TESIS DOCTORAL

2018

NUEVOS NANOMATERIALES APLICADOS COMO CATALIZADORES PARA ALGUNOS PROCESOS DE VALORIZACIÓN DE PRODUCTOS DERIVADOS DE LA BIOMASA

CAROLINA RAMÍREZ BARRIA

PROGRAMA DE DOCTORADO EN CIENCIAS

Director: Dr. ANTONIO GUERRERO RUIZ

Codirectora: Dra. INMACULADA RODRIGUEZ RAMOS

Programa de Doctorado en Ciencias

Madrid, Abril de 2018

NUEVOS NANOMATERIALES APLICADOS COMO CATALIZADORES PARA ALGUNOS PROCESOS DE VALORIZACIÓN DE PRODUCTOS DERIVADOS DE LA BIOMASA

CAROLINA RAMÍREZ BARRIA

Memoria para optar al grado de
Doctor en Ciencias

Dirigida por:

Dr. Antonio Guerrero Ruiz
Catedrático de Universidad
Dpto. Química Inorgánica
y Química Técnica
Facultad de Ciencias
UNED

Dra. Inmaculada Rodríguez Ramos
Profesora de Investigación
Instituto de Catálisis y
Petroleoquímica
CSIC

AGRADECIMIENTOS

Ahora que ha llegado el final de este viaje, es hora de agradecer a todas las personas e instituciones que me apoyaron y han colaborado de alguna manera en la realización de este trabajo:

En primer lugar, quiero agradecer enormemente a mis directores de Tesis: al Dr. Antonio Guerrero-Ruiz y a la Dra. Inmaculada Rodríguez-Ramos, por ofrecerme la posibilidad de llevar a cabo mi formación en el GDMCH. Agradeceros infinitamente de corazón que nos hagáis sentir siempre parte de esta familia y por aceptarnos tal como somos.

También quisiera expresar mi agradecimiento,

Al Ministerio de Educación, Cultura y Deporte por la financiación de este trabajo doctoral a través de la concesión de una Beca de formación de profesorado universitario (FPU).

A todo el personal del Instituto de Catálisis y Petroleoquímica, en especial a los miembros de la unidad de apoyo.

A todo el personal del departamento de Química Inorgánica y Química Técnica de la UNED.

I would like to thank to Karen Wilson, who helped and supervised me during my stay at the European Bioenergy Research Institute (EBRI), Aston University, UK.

A Cristina y Nadia. No podríamos ser un cluster más heterogéneo, ha sido una suerte trabajar con vosotras. Y no quiero dejar de mencionar a la cuarta chocolatina: Margarida, que nos alegro los días durante 6 meses en 2016.

A mis hermanas de la vida, Ivonne y Rosita, gracias por hacerme reír en la distancia como si el tiempo no hubiera pasado.

A Betty, por su amor puro e incondicional.

Finalmente doy las gracias a mi familia, especialmente a mi hermana Mariana, a Cristian y a Jaime. Gracias por estar siempre presentes y por cuidar de Betty durante las estancias. Sin vuestra ayuda esto no habría sido posible.

To Gavin,

For your endless love, encouragement and support,

I am thankful for having you in my life.

TABLA DE CONTENIDOS

Tabla de contenidos

LISTA DE CONTENIDOS

LISTA DE ABREVIATURAS

1,4-PeD : 1,4-pentanediol

1,2-PeD : 1,2-pentanediol

2-MF: 2-Metilfurano

2-MTHF: 2-Metiltetrahidrofurano

5-HMF: 5-Hidroximetilfurfural

AC: Carbon activado

BET: Ecuación de Brunauer-Emmett-Teller para determinar áreas superficiales, también se refiere al método de determinación volumétrica de isotermas de adsorción

DFF: 2,5-diformilfurano

DMF: Dimetilfurano

DRX: Difracción de Rayos X

EA: Análisis elemental

FAL: Furfural

FOL: Furfuril alcohol

FDCA: Acido 2,5-furandicarboxilico

FFCA: Acido 5-formil-2-furancardboxilico

G: Grafito

GO: Oxido de grafito

HFCA: Acido 5-hidroximetil-2- furancarboxilico

HSAG: Grafito de alta area superficial

ICP-EOS: Espectrometría de emisión óptica de plasma acoplado inductivamente

IEP: Punto isoeléctrico

NPs: Nanopartículas

N-rGO: Oxido de grafeno reducido dopado con nitrógeno

NrGO: Oxido de grafeno reducido dopado con nitrógeno

PEF: Polietilen furanoato

PET: Polietilen tereftalato

PZ: Potencial zeta

rGO: Oxido de grafeno reducido

S_{BET}: Area superficial determinada por el método BET

STY: Site time Yield

TEM: Microscopia electrónica de transmisión

THFA: Tetrahidrofurfuril alcohol

TGA: Análisis termogravimétrico

TPD: Desorción a temperatura programada

XRD: Difracción de rayos X

XPS: Espectroscopía fotoelectrónica de rayos

LISTA DE FIGURAS

LISTA DE TABLAS

RESUMEN-ABSTRACT

RESUMEN

El efecto producido por la presencia de heteroátomos sobre las propiedades superficiales de los materiales grafénicos merece especial consideración. Más precisamente, se ha demostrado que la incorporación de N en los materiales grafénicos modifica sus propiedades químicas y eléctricas. Esto es debido al hecho de que la presencia de N cambia la densidad electrónica del material de carbono incorporando un electrón más en la superficie volviéndolo más básico. Esta posibilidad de modificar las propiedades de la superficie y la elevada área superficial que poseen los materiales grafénicos, los convierte en materiales altamente prometedores para ser usados como catalizadores o soportes de catalizadores heterogéneos.

Por otro lado, la producción sostenible de productos químicos y combustibles ha recibido un renovado interés en los últimos años debido a las predicciones que sugieren el agotamiento de los recursos fósiles. Además, se espera un gran aumento en la demanda de combustibles no renovables debido al enorme crecimiento económico de potencias emergentes como India y China. No menos importante es la contribución al cambio climático a mediano y largo plazo que produce el uso masivo de recursos no renovables. La liberación de CO_2 de la combustión de recursos fósiles es una de las principales fuentes de gases de efecto invernadero. Por lo tanto, el crecimiento de la demanda, agravada por la disminución de las reservas, requerirá el desarrollo de nuevas rutas para la producción de productos químicos, combustibles y materiales a partir de materias primas renovables que tengan un menor impacto ambiental.

El uso de biomasa como materia prima renovable es una alternativa prometedora para la producción de productos químicos y combustibles. La biomasa lignocelulósica es un recurso ampliamente disponible. Además, desde el punto de vista ético, el uso de materiales lignocelulósicos evita la competencia con los alimentos.

En este contexto, el 5-hidroximetilfurfural, furfural y alcohol bencílico son moléculas plataforma derivadas de biomasa con un gran potencial para producir una gran cantidad de productos, que sean una alternativa a los derivados de recursos no renovables.

El objetivo de esta tesis se centra en el desarrollo de nuevos nanomateriales catalíticos basados en materiales grafénicos con propiedades optimizadas, dopados con nitrógeno o no, y nanopartículas (NPs) de Ru soportadas en ellos. Se trata de conocer el efecto de los grupos de N en las NPs Ru y cómo las propiedades del soporte pueden afectar el rendimiento catalítico de las mismas en la valorización de moléculas plataforma: Para ello se ha realizado un estudio detallado de tres reacciones:

- ✓ La oxidación en fase acuosa de 5-hidroximetilfurfural (5-HMF) a ácido 2,5-furandicarboxílico (FDCA) sin añadir bases como co-catalizadores.
- ✓ La hidrogenación en fase acuosa del furfural (FAL) a alcohol furfurílico (FOL).
- ✓ La oxidación selectiva de alcohol bencílico a benzaldehído utilizando oxígeno como agente oxidante en condiciones suaves sin utilizar bases.

En primer lugar, se prepararon materiales grafénicos dopados con nitrógeno y no dopados, por oxidación enérgica de grafitos naturales de diferentes tamaños de partículas (mesh 10, 100 y 325) y posterior tratamiento térmico en atmósfera conteniendo amoníaco o en atmósfera inerte, produciendo óxido de grafeno reducido dopado con nitrógeno (NrGO) y óxido de grafeno reducido (rGO), respectivamente. Se realizó una exhaustiva caracterización textural, estructural, superficial y morfológica de los materiales obtenidos.

Las muestras se caracterizaron por análisis elemental, fisisorción de nitrógeno (BET), análisis termogravimétrico (TGA), difracción de rayos X (XRD), microespectroscopía Raman (RAMAN), microscopía electrónica de transmisión (TEM), potencial zeta (PZ) y espectroscopía fotoelectrónica de rayos X (XPS). Estos resultados se discuten en el Capítulo 4, sección 1. Los datos de caracterización señalan que las propiedades físicas de los materiales, así como las especies de nitrógeno introducidas dependían del tamaño de partícula del grafito de partida, la atmósfera de reducción (NH_3 o inerte), de la temperatura final de tratamiento y de la rampa de calentamiento utilizadas durante el proceso de exfoliación. Estos hallazgos indicaron que es posible optimizar las propiedades del grafeno y el grafeno dopado con N, tales como el número de capas, el área superficial y el contenido de nitrógeno, mediante una estrategia simple basada en seleccionar el tamaño adecuado de grafito inicial y las condiciones experimentales convenientes durante el proceso de exfoliación térmica. Asimismo, se ha demostrado la reproducibilidad de este proceso de producción. En cuanto a la optimización de las propiedades superficiales, se lograron áreas de superficie máximas de 492 m^2g^{-1} para NrGO y 867 m^2g^{-1} para rGO.

El NrGO y rGO optimizados se han utilizado como soporte de nanopartículas de Ru. Con fines comparativos, también se evaluaron diferentes soportes comerciales (SiO_2, TiO_2, Al_2O_3, carbón activado y grafito de alta área superficial). También se han evaluado los efectos de los diferentes precursores metálicos utilizados ($RuCl_3$, $RuNO(NO_3)_3$ y $Ru_3(CO)_{12}$) en la preparación de las nanopartículas de Ru y el efecto de diferentes temperaturas de reducción. Además, se ha iniciado el estudio de otros metales (como Cu, Ag y Au) soportados también en los materiales grafénicos.

Los catalizadores de Ru se caracterizaron por análisis termogravimétrico (TGA), microscopía electrónica de transmisión (TEM), difracción de rayos X (XRD), desorción programada por temperatura (TPD) y espectroscopía fotoelectrónica de rayos X (XPS). Estos resultados se resumen en el Capítulo 4, sección 2 de este documento. Los análisis confirmaron que el Ru se encontraba disperso de manera uniforme en los materiales grafénicos sintetizados y también en los materiales comerciales.

En el Capítulo 4, sección 3, se han recogido los resultados catalíticos obtenidos con los catalizadores de Ru soportados sobre materiales grafénicos y sobre otros materiales comerciales, para cada una de las tres reacciones estudiadas. Además, en las reacciones de oxidación de 5-HMF e hidrogenación de FAL se llevó a cabo una comparación del comportamiento catalítico del Ru con los metales antes citados (Cu, Ag y Au)

Respecto a la reacción de oxidación de 5-HMF, los diferentes soportes modifican significativamente los rendimientos catalíticos, siendo las NPs de Ru soportadas sobre los materiales grafénicos aquellas que bajo nuestras condiciones de reacción experimentales producen la mayor selectividad hacia FDCA. En estos últimos soportes (rGO y NrGO) la conversión más alta de 5-HMF se logró usando $Ru_3(CO)_{12}$ como precursor de rutenio. Para el mejor catalizador, Ru soportado en NrGO, el rendimiento hacia FDCA se acerca al 80%. Este catalizador se ha reutilizado varias veces, sin pérdida de actividad ni modificaciones en los valores de selectividad. Los datos de caracterización señalan que los resultados catalíticos se pueden correlacionar con las propiedades básicas del soporte de NrGO, así como con las propiedades de superficie de las nanopartículas de Ru. Estos hallazgos indicaron que el precursor del metal y la existencia de átomos de nitrógeno en la superficie del soporte pueden modular las propiedades catalíticas, en particular modificando la selectividad hacia la producción de FDCA.

La hidrogenación en fase acuosa de FAL a FOL se ha estudiado en un reactor discontinuo en condiciones muy suaves de 20°C y 10 bares de hidrógeno. Los diferentes soportes modifican notablemente el comportamiento catalítico, siendo los catalizadores de Ru soportados sobre materiales grafénicos los que producen la más alta conversión de FAL y la máxima selectividad a FOL. En estos últimos soportes, la conversión de FAL más alta se logró utilizando $Ru_3(CO)_{12}$ como precursor de rutenio. El rutenio soportado en óxido de grafeno reducido (rGO) mostró una conversión del 93% con un 98% de selectividad hacia FOL. Se encontró que este catalizador exhibía excelente estabilidad y se reutilizó al menos 4 veces sin pérdida significativa de actividad ni disminución de la selectividad. Los datos de caracterización sugieren que las diferencias catalíticas pueden atribuirse al tamaño de las nanopartículas de Ru, así como a su interacción con la superficie de los materiales grafénicos, sin efecto aparente debido a la presencia de átomos de nitrógeno. Además, los resultados catalíticos están influenciados por el tipo de precursor de metal y la temperatura de reducción, lo que sugiere que la génesis de las nanopartículas de Ru también puede desempeñar un papel clave controlando las actividades catalíticas obtenidas con estos catalizadores en la hidrogenación del FAL en FOL.

Finalmente, para la oxidación del alcohol bencílico también se ha encontrado que los diferentes soportes modifican fuertemente el comportamiento catalítico, siendo los catalizadores de Ru soportados en NrGO los que, bajo nuestras condiciones de reacción experimentales, producen la conversión más alta del alcohol bencílico al producto deseado. Por lo tanto, el rendimiento catalítico se potencia significativamente por la presencia de N en la estructura grafénica en comparación con el soporte no dopado (rGO). El precursor del metal también juega un papel importante en la actividad de los catalizadores en la oxidación del alcohol bencílico. El catalizador de Ru preparado usando $Ru_3(CO)_{12}$ como precursor soportado en NrGO exhibe la más alta actividad catalítica para la oxidación a 90°C del

alcohol bencílico al aldehído correspondiente. Este catalizador mostró una actividad casi tres veces mayor en comparación con el catalizador de Ru soportado en carbón activado. Las diferencias en comportamiento catalítico se pueden atribuir a que se produce una interacción de tipo ácido-base entre el producto de la reacción con carácter ácido y la superficie básica del material grafénico dopado con N. Este hecho confiere una mejora de la actividad catalítica significativa en la oxidación selectiva del alcohol bencílico sobre Ru soportado sobre NrGO, en comparación con el soportado en rGO. Este catalizador se desactiva probablemente debido a la acumulación de agua que bloquea los sitios activos superficiales. Se encontró que la superficie del catalizador desactivado se puede regenerar fácilmente con un simple tratamiento de secado.

ABSTRACT

Special consideration must be paid to the effect induced by the presence of heteroatoms at the surfaces of graphenic materials over their properties. More precisely, it has been demonstrated that the incorporation of N into graphenic materials modifies their chemical and electrical properties. It is due to the fact that N presence improves electronic density of the carbon material incorporating by one more electron into the carbon surface becoming more basic. The possibility of tuning the chemical surface properties of graphenic materials and also their high specific surface areas, make them highly promising materials to be used as either catalysts or supports of heterogeneous catalysts.

On the other hand, the sustainable production of value-added chemicals and fuels has received a renewed interest in recent years due to predictions suggesting the depletion of fossil resources. In addition, a huge increase in the demand for fossil fuels is expected due to the enormous economic growth of emerging powers like India and China. No less important is the contribution to climate change in the medium and long term that produces the massive use of non-renewable resources. The release of CO_2 from the combustion of fossil resources is one of the main sources of greenhouse gases. Therefore, the expansion of the demand, aggravated by diminishing reserves, will require the development of new routes for the production of chemicals, fuels, and materials from renewable feedstocks that have a lower environmental impact.

The use biomass as renewable feedstock is a promising alternative for the production of chemicals and fuels. Lignocellulosic biomass is a widely available resource. Besides, from the ethical point of view, the use of lignocellulosic materials avoids competition with food.

In this context, 5-hdyroxymethylfurfural, furfural, and benzyl alcohol are promising biomass-derived platform molecules with a huge potential to produce a large number of valuable products as alternative to those derived from non-renewable resources.

The motivation of this Doctoral Thesis is focused on developing new catalytic nanomaterials based on N-doped and non-doped graphenic materials with tailored properties, and on Ru nanoparticles (NPs) supported on them. In order to comprehend the effect of N-groups on Ru NPs and how support properties can affect the catalytic performance of these catalysts; three valorisation reactions of relevant platform molecules derived from biomass have been extensively studied:

- ✓ The base free aqueous-phase oxidation of 5-hydroxymethylfurfural (5-HMF) to 2,5-Furandicarboxylic acid. (FDCA)
- ✓ The aqueous-phase hydrogenation of furfural (FAL) to furfuryl alcohol (FOL).
- ✓ The selective oxidation of benzyl alcohol to benzaldehyde using molecular oxygen as an oxidizing agent under base-free mild conditions.

Firstly, N-doped and non-doped graphenic materials were prepared by vigorous oxidation and further thermal treatment of natural graphites of different particle sizes (10, 100 and 325 mesh) under ammonia and inert atmospheres, leading to nitrogen doped reduced graphene oxide (NrGO) and reduced graphene oxide (rGO), respectively. An exhaustive textural, structural, superficial and morphological characterization has been made for the obtained materials.

Samples were characterized by elemental analysis, nitrogen physisorption (BET), thermogravimetric analysis (TGA), X-ray diffraction (XRD), Raman micro-spectroscopy (RAMAN), transmission electron microscopy (TEM), zeta potential (PZ), and X-ray photoelectron spectroscopy (XPS). These results are discussed in Chapter 4, section 1. Characterization data point out that the physical properties of the materials, as well as the nitrogen species introduced were dependent on the particle size of the starting graphitic material, the reduction atmosphere (NH_3 or inert) and the final temperature and heating ramp used during the exfoliation treatment. These findings indicated that is possible to tailor properties of graphene and N-doped graphene such as, number of layers, surface area and nitrogen content using a simple strategy based on selecting adequate starting graphite size and convenient experimental conditions during the thermal exfoliation process. The reproducibility of this production process has also been demonstrated. Regarding the optimization of surface properties, maximum surface areas of 492 m^2g^{-1} for NrGO and 867 m^2g^{-1} for rGO were achieved.

The optimized NrGO and rGO have been used as support of Ru nanoparticles. For comparative purposes different commercial supports (SiO_2, TiO_2, Al_2O_3, activated carbon and high surface area graphite) were also evaluated. The effects of different metal precursors used ($RuCl_3$, $RuNO(NO_3)_3$ and $Ru_3(CO)_{12}$ in the preparation of the Ru nanocrystallites and of different reduction temperatures have been assessed. Moreover, the effect of other metals (such as Cu, Ag, and Au) supported on graphenic materials was incipiently addressed.

Ru catalysts were characterized by thermogravimetric analysis (TGA), transmission electron microscopy (TEM), X-ray diffraction (XRD), temperature programmed desorption (TPD), and X-ray photoelectron spectroscopy (XPS). These results are summarized in Chapter 4, section 2 of this document. The analyses confirmed that Ru was evenly dispersed on the graphenic materials and also over commercial materials.

In Chapter 4, section 3 of the present memory, the catalytic results obtained with the Ru catalysts supported on the graphenic materials and over commercial materials are collected for each one of the 3 reactions studied. Additionally, for the oxidation of 5-HMF and the hydrogenation of FAL a comparison of the catalytic performance of Ru with other metals (such as Cu, Ag, and Au) was carried out.

Regarding the oxidation of 5-HMF, the different supports significantly modify the catalytic performances, the Ru NPs supported on graphenic materials being those, that under the experimental reaction conditions used, produce the highest selectivity to FDCA. On these later supports (rGO and NrGO) the highest HMF conversion was achieved by using $Ru_3(CO)_{12}$ as ruthenium precursor. For the improved catalyst, Ru supported on NrGO, yield towards FDCA becomes close to 80%. This catalyst has been reused several times with neither loss of activity nor modifications in selectivity values. Characterization data point out those catalytic results can be correlated to basic properties of NrGO support as well as to the surface properties of Ru nanoparticles. These findings indicated that metal precursor and the presence of nitrogen atoms exposed on the support can modulate the catalytic properties, in particular amending the selectivity towards FDCA production.

In addition, the aqueous-phase hydrogenation of FAL to furfuryl alcohol FOL has been studied in a batch reactor under very mild conditions of 20ºC and 10 bar hydrogen. The different supports notably modify the catalytic behaviour, the Ru based catalysts prepared using graphenic materials being found to produce the highest conversion of FAL and the maximum of selectivity to FOL. On these later supports the highest FAL conversion was achieved by using $Ru_3(CO)_{12}$ as ruthenium precursor. Ruthenium supported on reduced graphene oxide (rGO) shows 93% conversion with a 98% of selectivity towards FOL. This catalyst was found to exhibit excellent stability, and was reused at least 4 times without loss of activity or selectivity. Characterization data suggest that the catalytic differences can be attributed to the particle size of Ru nanocrystals as well as to their interaction with the surface of graphenic materials, without apparent effect of the nitrogen functional groups. Furthermore, the catalytic results are influenced by the type of metal precursor and the reduction temperature, these facts suggesting that the genesis of the Ru nanoparticles can also play a key role controlling the catalytic activities obtained with these catalysts in the hydrogenation of FAL into FOL.

Finally, for the oxidation of benzyl alcohol, the different supports strongly modify also the catalytic behaviour, the Ru NPs supported on NrGO materials being those that, under the experimental reaction conditions used, produce the highest conversion of benzyl alcohol to the desired product. Thus, the catalytic performance is significantly enhanced by presence of N in the graphenic structure as compared to non-doped counterpart (rGO). Metal precursor also plays an important role on the activity of the catalysts in oxidation of benzyl alcohol. Ru prepared by using $Ru_3(CO)_{12}$ as precursor supported on NrGO exhibits the best catalytic activity for the oxidation of benzyl alcohol to the corresponding aldehyde at 90ºC. This catalyst showed almost three times higher activity in comparison with an activated carbon supported Ru catalyst. The differences in catalytic performance can be attributed to an acid-

base interaction between the acidic product of the reaction and the basic surface of N doped graphenic materials. This fact confers significant rate enhancement in the selective oxidation of benzyl alcohol over Ru supported over NrGO compared to rGO. The catalyst deactivated probably due to water accumulation blocking the active sites. It was found that the surface of the spent catalyst can be easily regenerated with a simple drying treatment.

INTRODUCTION

1. INTRODUCTION

1.1. Background

The use of renewable resources for the production of fuels and chemicals is a field of growing interest due to the predictions that suggest the depletion of fossil fuels. Fossil resources such as crude oil, coal, and natural gas, are the three most utilized raw materials by industrial economies.[1] They provide more than three quarters of the world's energy[2] and most speciality chemicals are directly or indirectly produced from them**.** [1] Thus, worldwide dependence on fossil reserves is alarming. Several studies have been devoted to calculate when non-renewable resources will be diminished. In 2005, Topal et al. calculated fossil fuel reserve depletion times for crude oil, coal and gas of approximately 35, 107 and 37 years, respectively.[3] More recent studies suggest that the oil reserve will support our society for another 50 years at the current rate of consumption.[1] It is an undeniable fact that diminishing fossil-fuel reserves will cause a great rise of the oil prices and chemicals in the near future.

During the 20th century the global population has almost quadrupled and the global energy consumption increased more than 16 fold over that period. [1] In addition, a huge increase in the demand for fossil fuels is expected due to the enormous economic growth of emerging powers such as India and China.[4]

No less significant is the contribution to climate change in the medium and long term that produces the massive use of non-renewable resources. The release of CO_2 from the combustion of fossil resources is one of the main sources of greenhouse gases.[1] Over the past few decades, improved awareness of the links between climate change and anthropogenic greenhouse gas emissions has led to increased political will in most of the countries to tackle this issue.[5]

The future supply of conventional oil is already and will become a geopolitical issue correlated to the unequal location of fossil fuels reserves.[3] Therefore, the competition for the resources might lead to conflicts.

All these factors are causing increasing concern with regard to the stability of the global economy and the environment. In this context, numerous research studies have been devoted to the development of more sustainable routes for the production of chemicals, fuels, and materials from renewable feedstocks that have a lower environmental impact, such as biomass.

1.2. Biomass

As mentioned above, the use biomass as renewable feedstock for the production of chemicals and fuels has become the focus of considerable interest from both academia and industry.

The term biomass refers to any organic material that is available in a renewable way. Examples of this are crops (such as corn, wheat, barley, sugar crops, grasses, woody crops, vegetable oils), agricultural residues, aquatic plants, algae, trees, wood residues, logging residues, animal waste, urban wastes and other waste materials.[6]

It is widely believed that fuels and chemicals derived from biomass are CO_2 neutral regarding the release of CO_2 because the CO_2 released during the combustion or use of them, can be later utilized for biomass growth in the next cycle. In reality, they can be either CO_2 neutral, positive or negative, depending on how land use is affected by the biomass source. If the biomass is replanted, the carbon released from combustion is recaptured and the biomass energy cycle is generally CO_2 neutral. If forests are cleared to allow bioenergy plantations, then substantial initial emissions are produced and the balance would be positive. If, on the other hand, biomass energy plantations are established on lands with sparse vegetation, there might be an initial accumulation of carbon on the land, and the emission would become negative. For those reasons, it is assumed that biomass energy produced in a sustainable way, in the absence of carbon capture and storage, is CO_2 neutral. It should be noted that the CO_2 impact of biomass also depends on the contribution produced by fossil resources in the production, transport and conversion of the biomass.[7]

Other environmental benefit of biomass is the very low content of nitrogen and sulfur. This fact significantly reduces sulphur oxides and nitrogen oxide emissions released, compared to fossil fuels.[8]

Depending on the raw material used and the production process, biofuels are classified as first-generation biofuels, second generation and third generation. First generation biofuels are considered those produced from agricultural raw materials. Their processing involves food crops (e.g., sugar, starch and oils) and consists mainly in the production of alcohols (bioethanol) and oils (biodiesel).[9] Although these processes are considered efficient, from the ethic point of view, first generation biofuels are subject of controversy due to the competition generated as they are produced at the expenses of food crops and the land use.[10] Second generation biofuels are predominantly produced from lignocellulosic materials. For this reason, it is considered more viable from an ethical and renewable perspective as the feedstocks are generally not competitive with food stocks.[9] The third generation of biofuels involves algae crops as a sustainable source of feedstocks for bioethanol and biodiesel. However, these potential alternatives are still at an early stage of development.[9]

Feedstocks derived from biomass can be classified into three general groups: lignocellulosic feedstocks (e.g., bagasse, corn stover, grasses, wood, etc.), starchy feedstocks (e.g., starch, glucose, etc.), and triglycerides feedstoocks (e.g., vegetable oil). Among the feedstocks derived from biomass the cheapest, most abundant, and fastest growing form of biomass is lignocellulosic biomass.[11]

1.2.1. Composition of lignocellulosic biomass

Lignocellulosic biomass is composed mainly of cellulose, hemicellulose, and lignin (Figure 1.1) which comprise 40-50%, 25-35% and 15-20%, respectively.[12]

Cellulose is a polymer formed by a large number of molecules of glucose units linked via β-glycosidic bonds. It is a crystalline and hydrophobic material with an extended, flat, 2-fold helical conformation forming intra and inter chain hydrogen bonds between the monomers that help to maintain and reinforce the flat, linear conformation of the chain, making cellulose reluctant toward hydrolysis.[6,13]

In contrast to cellulose, hemicellulose is a polymer formed by 5 different sugars (glucose, galactose, mannose, xylose and arabinose) all of which are highly substituted with acetic acid, and it does not form crystalline regions making it more amenable to hydrolysis. Consequently, hemicellulose is easier to hydrolyse compared to cellulose.[6]

The lignin fraction of biomass is a highly complex, branched, amorphous polymer composed by phenolic and allylic alcohols, such as coniferyl alcohol, sinapyl alcohol, and coumaryl alcohol, which surrounds the hemicellulose and cellulose fractions and provide plants with structural rigidity.[6,9]

The enormous degree of chemical complexity of the lignocellulosic biomass and its high resistance towards either catalytic or enzymatic hydrolysis lead to high costs of processing compared to biomass derived from edible resources. For that reason, the development of new processes for the valorisation of lignocellulosic biomass is the main challenge in the production of second generation biochemical and biofuels. Its processing usually involves a series of pretreatments to liberate the cellulose from lignin and break down its rigid structure and thus, once isolated cellulose can be hydrolyzed into glucose monomers.[14]
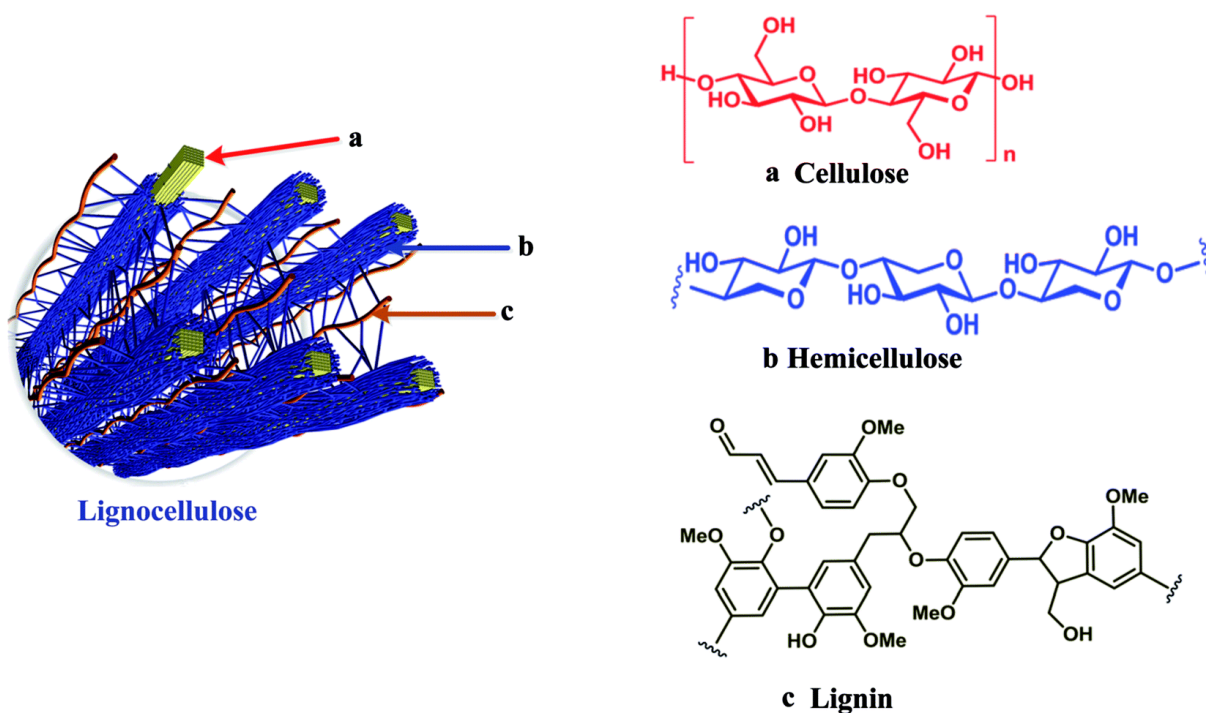
Figure 1.1 Composition of lignocellulosic biomass.[15]

1.2.2. Chemical routes for the conversion of the lignocellulosic biomass

It is clear that the challenge of manufacturing bulk chemical products from biomass or other renewable raw materials, instead of using products obtained from fossil fuels, is currently a field of great interest. Likewise, the development of sustainable processes and the revision of the synthesis methods already established, in order to reduce the environmental impact derived from the chemical production, are presented as valuable tools to lead to more efficient industrial processes.

Chemical compounds generate almost 50% of the profit in current refineries. This fact results remarkable, as only about 5-10% of the crude oil is converted into chemicals. It is not expected that this ratio change in a future, which indicates the huge economic potential in producing chemicals from biomass.[16] However, the cost of fuels and chemicals produced from biomass is still higher than that produced from fossil resources.

26 leading experts have written a report called "Roadmap for Biomass Technologies". It has been predicted that by 2030, 20% of transportation fuel and 25% of chemicals will be produced from biomass. US Department of Energy (US DOE) and the US Department of Agriculture (US DA) have estimated that to achieve these goals, the US should produce 1.3 billion dry tons of biomass per year. Based on current technology, the only biofuels produced and used on a large scale are corn-to-ethanol and oil-to-biodiesel and they have limited capacity to fulfill the agreed targets. Thus, the development of new technology for processing lignocellulosic biomass for fuels and chemicals will be crucial.[2]

Many processes to transform lignocellulosic biomass into liquid fuels and chemical compounds have been reported. However, renewable fuels and chemicals are obtained from biomass by three basic processes: gasification, pyrolysis and hydrolysis.[6] The main pathways for the conversion of lignocellulosic biomass feedstocks into renewable fuels are shown in figure 1.2.
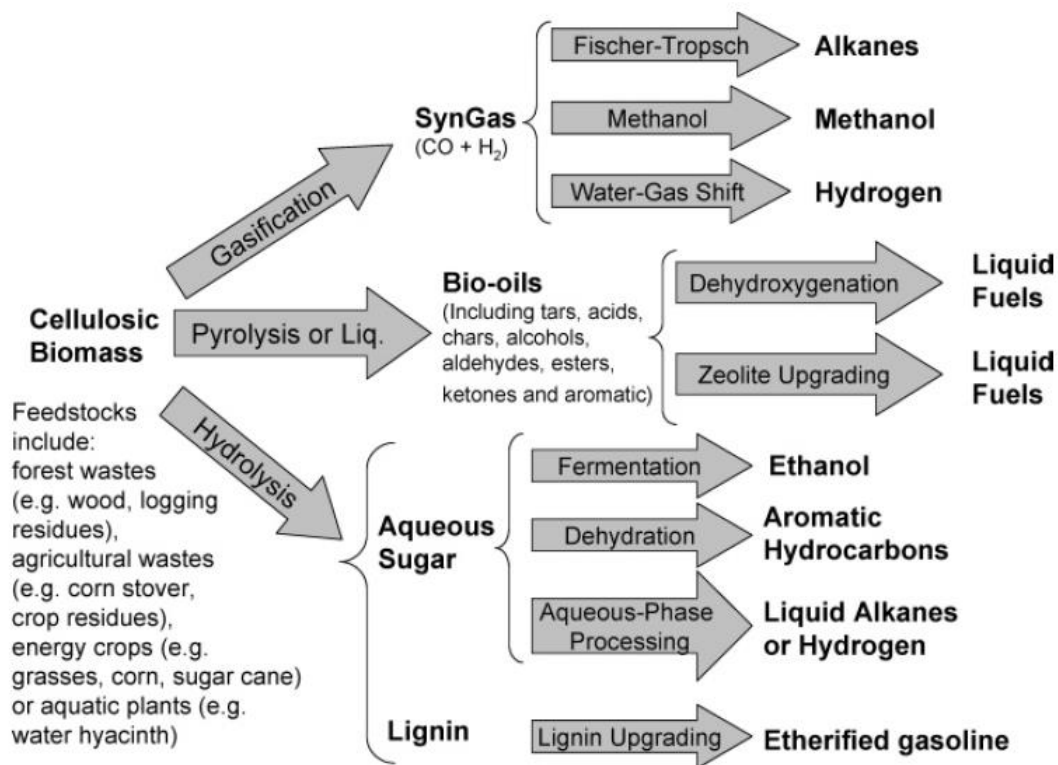
Figure 1.2 Strategies for the production of fuels and chemicals from lignocellulosic biomass. [11]

Gasification is a process carried out through partial combustion of biomass to produce a gas product called syngas that contains CO, H_2, CO_2, CH_4, and N_2 in various proportions. [6] There are two well-known processes for syngas conversion: methanol synthesis and Fischer–Tropsch synthesis, where the obtained syngas can be used as raw material to obtain hydrocarbons with properties similar to gasoline or diesel.[11]

Unlike gasification, pyrolysis is a thermal decomposition reaction of the solid biomass under conditions of absence of oxygen. This process can lead to products of very different nature that can be used for the production of energy in thermal power plants and as reagents to be transformed into numerous chemical products. The products of biomass pyrolysis primarily consist of biochar, bio-oil and gases including CH_4, H_2, CO and CO_2.[17]

Bio-oils are dark brown with a smoky odor and composed of polar organics (75–80 wt.%) and water (20–25 wt.%). [11] They are a mixture that can contain more than 400 different compounds, including acids, alcohols, aldehydes, esters, ketones, and aromatic compounds. Commercially, bio-oils are used as boiler fuel for stationary power and heat production, and for chemical production. Upgrading is required if bio-oils are going to be used as transportation fuels.[6]

Liquefaction is an alternative method for the production of bio-oils. Biomass is mixed with water and basic catalysts like sodium carbonate, and the process is carried out at lower temperatures than pyrolysis (250-450ºC) but higher pressures (50–200 atm) and longer residence times. These factors contribute to make liquefaction a more expensive process; however, the bio-oils produced through liquefaction have lower oxygen content than pyrolysis and typically requires less extensive processing.[9,11]

Through hydrolysis processes, monosaccharides are obtained at lower temperatures than gasification or pyrolysis. Hydrolysis uses acidic or enzymatic catalysts, to break the glycosidic bond between sugar units. Thus, sugar monomers are isolated, this being a complex and expensive step for lignocellulosic feedstocks. Monomers are processed by a variety of catalytic technologies and give access to the production of valuable platform molecules, such as furfural (FAL) and 5-hydroxymethylfurfural (5-HMF).[9]

1.2.3. Platform molecules

In 2004, the US Department of Energy (DOE) released a report named "Top Value Added Chemicals from Biomass". This publication described a group of 12 building block chemicals, the so-called platform molecules that could be produced from biorefinery carbohydrates. These molecules have multiple functional groups conferring them a huge potential to be transformed into new useful molecules. The twelve sugar-based building blocks were 1,4-diacids (succinic, fumaric and malic), 2,5-furandicarboxylic acid, 3-hydroxypropionic acid, aspartic acid, glucaric acid, glutamic acid, itaconic acid, levulinic acid, 3-hydroxybutyrolactone, glycerol, sorbitol, and xylitol/arabinitol.[18,19]

In 2009, Bozell et al.[18] presented an updated evaluation of potential platform molecules including ethanol, bio-hydrocarbons, polyols (sorbitol, xylitol, glycerol), furans (furfural, 5-hydroxymethylfurfural) and acids (succinic acid, levulinic acid, hidroxypropionic acid, and lactic acid).

1.3. Furanic derivatives as platform molecules

The chemistry of furans and their derivatives is very noteworthy due to the huge variety of chemicals that can be obtained from them. Furfural and 5-Hydroxymehilfurfural are the most important molecules that represent furan derivatives. They are promising biomass-derived platform molecules generally produced trough chemical dehydration of pentoses and hexoses respectively.

1.3.1. 5-Hydroxymethylfurfural

5-HMF has been extensively studied in several reviews.[4,20] It can be converted into highly attractive products for the chemical industry, being a significant starting material for the production of other chemicals with numerous important applications (Figure 1.3). It is included among the furan derivatives molecules mentioned by Bozzel et al.[18] in their update of the original DOE list.[19]

5-Hydroxymethylfurfural (5-HMF) is also known as 5-(hydroxy-methyl)-2-furancarboxaldehyde and 5-(hydroxymethyl)-2-furaldehyde. The reactivity of HMF molecule arises from the presence of hydroxyl and aldehyde groups as well as a furan ring. HMF is a yellow solid with a boiling point between 114 and 116ºC. It is soluble in many solvents, such as water, methanol, ethanol, benzene, acetone, chloroform, ethyl acetate and formaldehyde.[21]

The synthesis of 5-HMF was first reported in 1895 by Dull and Kiermeyer. Then, inulin (a β-2,1-fructan) was heated in acidic aqueous solution followed by solvent extraction. However, its structure was not definitively assigned until 1910.[13] Since then, thousands of papers have been published involving 5-HMF.

5-HMF is produced by removal of three molecules of water from hexoses in an acid-catalysed process. Despite the apparent simplicity of the conversion, in reality, several side-reactions may be produced, including the re-hydration of the 5-HMF to levulinic acid and formic acid, and cross-polymerisation to soluble polymers and insoluble humic compounds, that renders the HMF synthesis very complicated.[21]

Other problems associated to the synthesis of 5-HMF are the extraction and purification of the product from the aqueous medium, due to its high affinity with water and their close boiling points. For this reason the purification process has been studied using various organic solvents such as dichloromethane, ethyl acetate and tetrahydrofuran and extraction methods.[4]

5-HMF is a very important intermediate. It can be converted into biofuels, as dimethylfuran (DMF). It is also a relevant precursor for the synthesis of valuable molecules such as levulinic acid, 2,5-furandicarboxylic acid (FDCA), 2,5-diformylfuran (DFF), dihydroxymethylfuran and 5-hydroxy-4-keto-2-pentenoic acid.[22] Several pathways for conversion of 5-HMF are shown in Figure 1.3.

Among these routes, it is remarkable aldol-condensation as it allows to increase the molecule length through the formation of carbon–carbon bonds. Aldol-condensation is a base-catalysed reaction, through which diesel and jet fuel can be produced by the coupling between C3 aldehydes or ketones and 5-HMF. The condensed products, ranging from C9 to C15, can be hydrogenated reducing their oxygen content.[20]
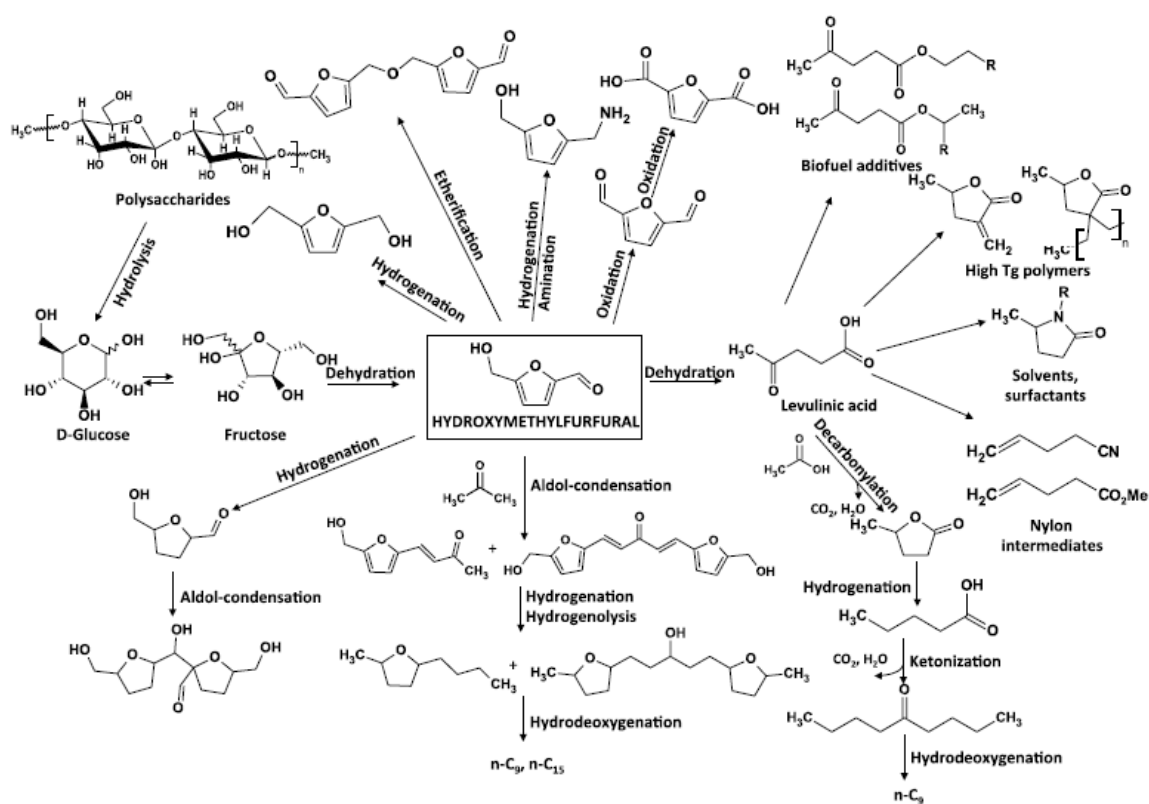
Figure 1.3 Pathways for conversion of 5-HMF.[20]

Etherification of 5-HMF is an alternative to produce chemicals for pharmaceutical industry. An example of this is the etherification of 5-HMF to synthesize 5,5-oxy(bis-meth-ylene)-2-furaldehyde, which can be used to produce imine-based polymers, as well as in the preparation of hepatitis antiviral precursors.[20]

The oxidation of HMF leads to the formation of FDCA, a bio-degradable candidate to replace terephthalic acid in the production of plastics. A complete revision of this reaction will be done later.

1.3.2. Furfural

Furfural is a promising biomass-derived platform molecule with a huge potential to produce a large number of valuable products (Figure 1.4). Furfural was isolated in 1821 by the German chemist Johann Wolfgang Döbereiner, who obtained it as a byproduct of the synthesis of formic acid.[23]

Furfural is generally produced by the hydrolysis and dehydration of xylan, which exists in large quantities in hemicellulose. The conversion of xylan into furfural was first industrialized in 1921 by the Quaker Oats Company. However, the current industrial production of furfural still uses the traditional method that is limited by a low yield of furfural, the use of corrosive homogeneous acid catalysts for the digestion of hemicellulosic wastes and high energy consumption.[12,24]

Furfural can be converted by diverse catalytic processes, such as oxidation, decarboxylation, aldol condensation, hydrogenation among other reactions into a wide range of molecules, which are valuable building blocks for the production of liquid fuels, fuel additives and chemicals.[12]

Furfural can be decarbonylated to furan under reductive conditions. Furan can be further hydrogenated to tetrahydrofuran which is commonly used as solvent and as starting material for polyurethane manufacture. [20] The selective oxidation of furfural can produce several C4 products, such as acid anhydride, dicarboxylic acids (succinic, malic, and fumaric acids) and furanones.[12]
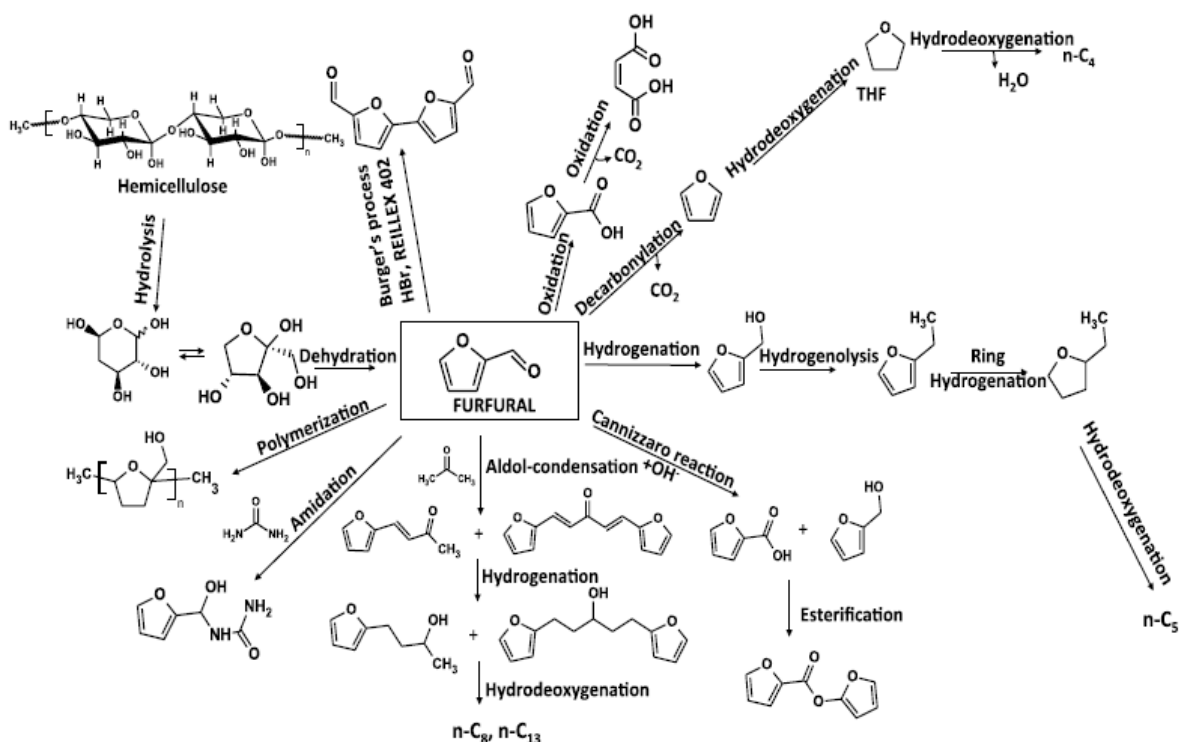
Figure 1.4 Pathways for conversion of furfural.[20]

Like 5-HMF, the aldol-condensation reaction of furfural with C3 aldehydes and ketones takes place in the presence of a basic catalyst. Coupling lead to condensation products, ranging from C8 to C13, that can be subsequently hydrogenated decreasing their oxygen content.[20]

Selective hydrogenation of furfural can lead to promising bio- fuel components as furfuryl alcohol (FOL), tetrahydrofurfuryl alcohol (THFA), 2-methylfuran (2-MF), 2-methyltetrahydrofuran (2-MTHF). A complete revision of this reaction will be done later.

1.4. Derived alcohols from lignocellulosic biomass

Currently, nearly 90% of ethanol is obtained from biomass. Ethanol can be produced from sugar, starch, or lignocellulosic feedstocks. In the United States, the primary route for converting biomass to bioethanol is the fermentation of corn. In Brazil, most ethanol is produced from fermentation of sugar cane using the Saccharomyces cerevisiae yeast. Many efforts have been done to replace edible sugars with lignocellulosic biomass as feedstock. In the biochemical conversion of lignocellulosic feedstocks, biomass is pre-treated to open up its structure. Then cellulose is hydrolysed to sugars which are then easily fermented to produce bioethanol. However the processes remain commercially unviable and present some difficulties. Current research plans suggest that production of bioethanol from lignocellulosic biomass will be competitive within a decade.[5,25]

At present commercial methanol is produced from biomass by gasification of renewable feedstocks to form a syngas. A gas-shift reaction is employed to adjust the gas mixture to the proper H_2 to CO ratio. The syngas is then catalytically converted to methanol.[25]

1-Butanol may be produced by alcohol homologation of methanol produced from syngas. Another option to obtain 1-butanol can be by microbial fermentation using organisms such as Clostridium acetobutylicum, which provides mixtures of acetone, 1-butanol, and ethanol. The hydrogenolysis of renewable triglycerides offers an alternative route to desirable C8+ alcohols. Ru, Os, and Pd catalysts have been reported as well to produce alcohols from fatty acids by oxidative cleavage using oxidants such as, O_3 or H_2O_2. The resulting aldehydes and acids can be later hydrogenated to form the desired alcohols.[5]

1.4.1. Benzyl alcohol

Benzyl alcohol deserves special attention, as it is an aromatic hydrocarbon alcohol with a broad range of commercial applications. It is a safe and effective strong polar solvent mainly due to its low volatility and toxicity. Benzyl alcohol is commonly employed as precursor and chemical intermediate in the pharmaceutical industry, synthesis of polymers and resins, and cosmetic production. Additionally, since benzyl alcohol provides a floral scent; it is commonly used as a precursor to synthesize numerous products for flavor and fragrance industries. It is also used as a topical agent and preservative in the pharmaceutical and healthcare industries as it has a bacteriostatic effect at even low concentrations. Benzyl alcohol is naturally synthesized by many plants, however, benzyl alcohol contents rarely surpass 30 mg/kg, and consequently these natural sources are unsuitable for supplying benzyl alcohol in a bulk scale. Benzyl alcohol is generally produced from petroleum-derived feedstocks. Most commonly, from benzyl chloride via alkaline hydrolysis under harsh reaction conditions.[26]

A sustainable approach is the biosynthesis of benzyl alcohol from renewable glucose by engineered E. coli, benzyl alcohol becoming a promising and representative biomass-derived platform molecule with a huge potential to produce a large number of valuable products.[26]

As mentioned above, valorisation of benzyl alcohol can generate several products. One of the most important reactions of benzyl alcohol is its oxidation into benzaldehyde and benzoic acid (Figure 1.5). Nevertheless, other by-products could be produced[27] depending on the reaction conditions as benzene (decarbonylation), toluene (hydrogenolysis) or benzyl benzoate (esterification).
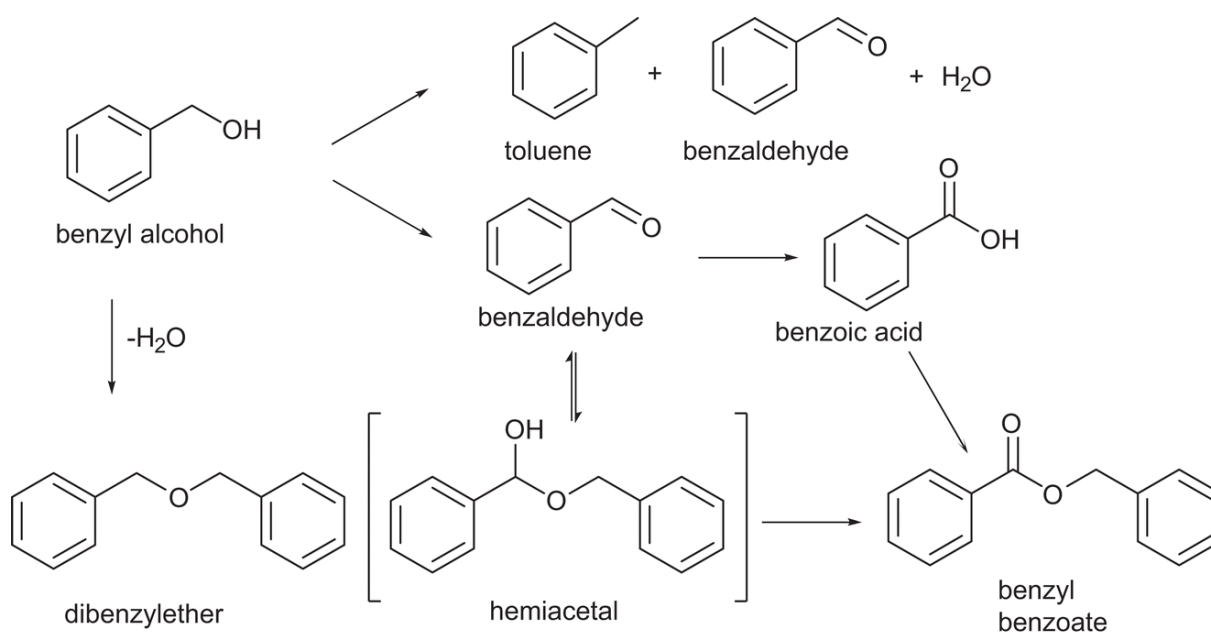
Figure 1.5 Pathways for conversion of benzyl alcohol.

1.5. Oxidation of 5-HMF

The oxidation of HMF can generate several kinds of products such as 2,5-diformylfuran (DFF), 5-hydroxymethyl-2-furancarboxylic acid (HFCA), 5-formyl-2- furancarboxylic acid (FFCA) and 2,5-furandicarboxylic acid (FDCA) (Figure 1.6). The oxidation of HMF can occur through the selective oxidation either on the aldehyde group or on the hydroxyl group to produce HMFCA or DFF respectively.
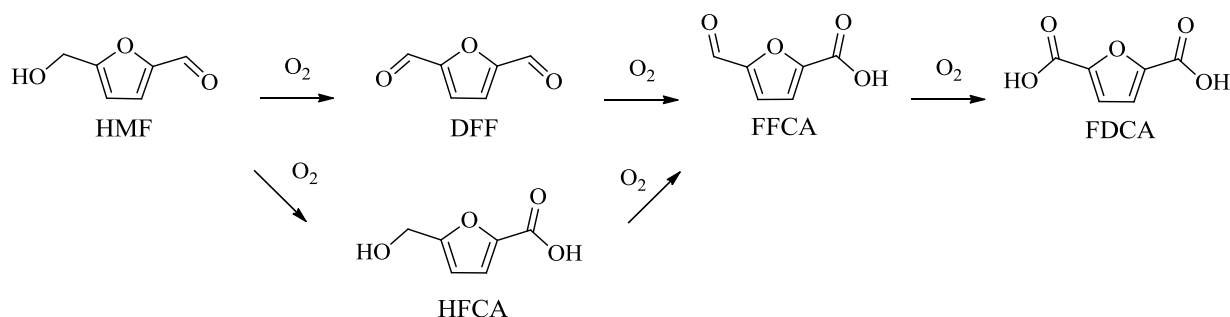
Figure 1.6 Reaction pathway from 5-HMF to FDCA

FDCA has been identified by the U.S. Department of Energy as one of the 12 top value added chemicals from biomass.[19] Terephthalic acid is the monomer employed in the production of polyethylene terephthalate (PET). FDCA can be used as alternative monomer to potentially replace terephthalic acid due to the structural similarity between them.[28] Polymerization of FDCA can produce polyethylene furandicarboxylate (PEF).

The Dutch company Avantium patented a process named YXY for the production of FDCA methyl ester using a catalyst based on Co/Mn/Br. Generic steps of the YXY process are shown in Figure 1.7. First, C6 sugars are converted to HMF ethers, by acid catalysed reaction of HMF with an alcohol such as methanol or ethanol, followed by oxidation to FDCA. To make the biobased polymer PEF, a third catalytic step brings together FDCA and Mono-Ethylene-Glycol (MEG).[28]

Avantium is currently producing PEF at pilot plant scale. In addition to the more favourable energy and GHG emissions balance, PEF bottles have superior properties compared to PET bottles. They have better thermal and barrier properties.[28]
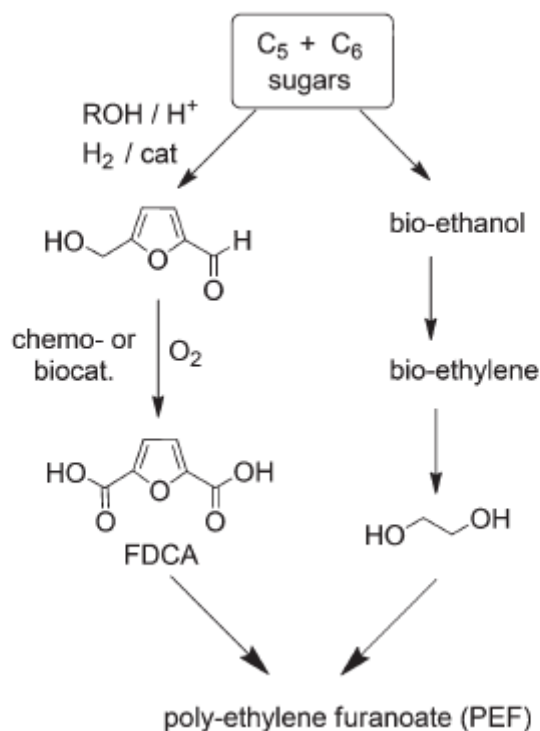
Figure 1.7 Avantium YXY® process for the production of PEF.[28]

Several stoichiometric oxidants, such as HNO_3, N_2O_4 and $KMnO_4$[29], as well as homogenous catalytic systems[30] have been used for the HMF oxidation into FDCA. However, harsh reaction conditions, corrosive properties of the media and production of large amounts of waste have a negative economic and environmental impact.

The oxidation of HMF to synthesize FDCA employing air or oxygen has been described along with different supported catalysts[31]. Among the studied heterogeneous catalysts are noteworthy those based on noble metals such as Pt[32,33], Au[34,35], and Ru[36]. However, it should be underlined that in most of the reported reaction procedures a base additive, essentially NaOH, KOH or Na_2CO_3, is required[22,37,38], so only very few works applying inorganic base-free catalysis have been reported.

Casanova et al.[39] claimed a useful strategy to avoid base added requirement, using methanol as solvent instead of water. Using an Au/CeO_2 catalyst under oxygen pressure, 2,5-dimethylfuroate is the main product. Despite its outstanding activity and selectivity, the oxidation of the solvent was unavoidable due to it follows a similar oxidation pathway than the substrate.

Highly basic solid supports have also been proposed as replacements of the inorganic bases during HMF oxidation in water. Gupta and coworkers [40] reported Au nanoparticles supported on hydrotalcite (HT) to catalyze the aqueous-phase oxidation of HMF to FDCA showing good performances. However, later studies[41] suggested that alkali contaminants from the synthesis of the HT supports or co-existing partially soluble brucite, favored the obtained results. Along the same lines, high yields of FDCA were also obtained by Gorvanev et al.[42] using $Ru(OH)_X$ supported on a HT and MgO. Nevertheless, extensive deactivation due to leaching of magnesium from both supports was described. In recent publications Au-Pd alloys[43] and Pt[44] supported on functionalized carbon nanotubes (CNT) were presented as base-free alternatives in the aerobic oxidation of HMF to FDCA under oxygen pressure. It is reported that the oxygen-containing functional groups, in particular carbonyl/quinone and/or phenol groups, on CNT surfaces play crucial roles in FDCA formation. These functional groups could enhance the adsorption of HMF as well as the reaction intermediates from water and might facilitate hydrogen transfer. Nonetheless, long reactions times of 12 and 14 h respectively were required besides the use of expensive metals as Au, Pt and Pd. Also, the facet effect and size-dependent effect of single-crystalline Pd nanocrystals on the aerobic oxidation of HMF has been systematically investigated by experimental and theoretical approaches[45]. It was found that the size-dependent effect of these Pd nanocrystals derived from the different surface Pd atom percentages. So, Pd atoms at (111) facets exhibited notably enhanced catalytic activity for the aerobic oxidation of HMF than Pd atoms at (100) facets. By controlling the amount of surface Pd atoms to be identical, Pd nanocrystals with the same shape but different particle sizes exhibited very similar catalytic performances for HMF

oxidation. Ruthenium catalysts supported on carbon materials were studied by Yi et al.[46], however very high Metal:HMF ratios are required to achieve significant catalytic yield to FDCA.

In order to understand the two steps in HMF oxidation into FDCA a brief introduction to the general mechanisms of oxidation of primary alcohols to aldehydes and aldehydes to acids is described below. As figure 1.8 outlines, the oxidation of a primary alcohol proceeds first to an aldehyde and subsequently to a carboxylic acid.

Davis et al. [47] proposed on a critical review that the oxidation of an alcohol to an aldehyde over a heterogeneous catalyst likely occurs in three steps: metal alkoxide formation, β-hydride elimination to produce a carbonyl compound and a metal hydride, and oxidation of the metal hydride and regeneration of the metal surface.

$$RCH_2OH \xrightarrow{[O]} RCHO \xrightarrow{[O]} RCOOH$$

Figure 1.8 General oxidation scheme for primary alcohols to acids.

Metal-alkoxide formation

The mechanism of primary alcohols oxidation to aldehydes likely begins with the formation of a metal alkoxide.[48–50] The nature of the metal or the nature of substrates adsorbed on the metal can influence its formation.[47]

The adsorbed metal alkoxide (RCH_2O^*) and a metal hydride (H^*) are produced when the alcohol adsorbs dissociatively on the metal surface and the O-H bond is broken.[51]

$RCH_2OH + * \leftrightarrow RCH_2OH*$

$RCH_2OH* + * \rightarrow RCH_2O* + H*$
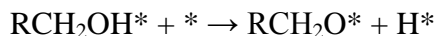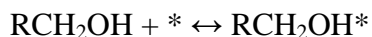
β-hydride elimination

There is a general agreement on a β-hydride elimination as the second step of alcohol oxidation over metallic catalysts. It produces a carbonyl species (RCHO*) and a metal hydride.[49–52] β-hydride elimination is assumed as the rate determinating step.[53]

$RCH_2O* + * \rightarrow RCHO* + H*$
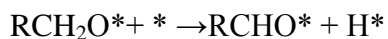
Oxidation of Metal Hydride and Regeneration of Catalyst Surface

The final step in the oxidation of an alcohol to aldehyde is the oxidation of the metal hydride species (H*) generated in the previous step to regenerate either the metal-hydroxide (OH*)[49] or metal surface(*)[48,50].

Regarding the oxidation of aldehyde to carboxylic acid is widely accepted that it proceeds through a geminal diol intermediate. The aldehyde in water experiments a reversible hydration to a geminal diol. The bases favour the conversion of the aldehyde into the corresponding geminal diol increasing the rate of hydration. Finally, the geminal diol is likely adsorbed to the metallic surface of the catalyst form a metal alkoxide, which will undergo β-hydride elimination to form a carboxylic acid.[47,54]

Zhou et al.[44] proposed that the gem-diol intermediate can be formed by the hydration of DFF and the β-hydride elimination of the gem-diol in the presence of Pt NPs lead to FFCA. Similarly, the hydration of the aldehyde group in FFCA might result in another gem-diol intermediate, which could be oxidized to FDCA in the subsequent step (Figure 1.9).
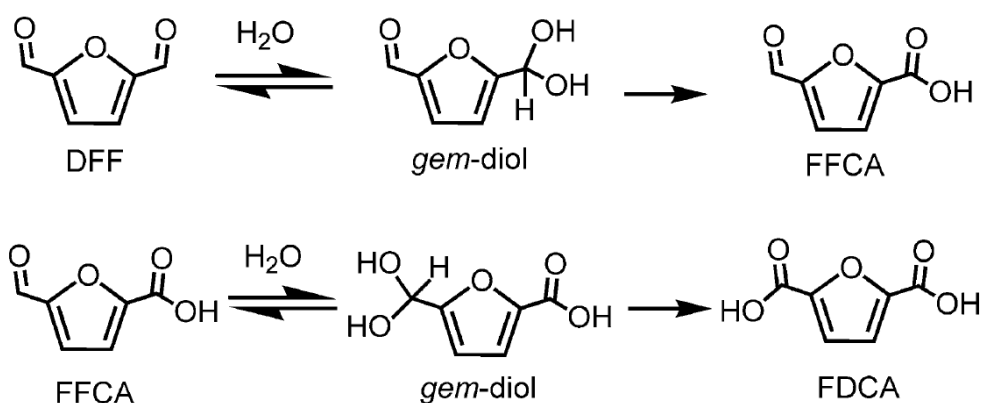
Figure 1.9 Possible reaction mechanisms for the conversions of DFF and FFCA.[44]

It is remarkable the role of oxygen in 5-HMF oxidation. Isotopic labelling studies carried out by Davis et al.[47] indicate that oxygen atoms from dioxygen are not directly incorporated in the acid molecules. However, oxygen is essential for the oxidation of HMF to FDCA. The role of oxygen in HMF oxidation is to scavenge electrons from the metal catalyst surface being reduced to peroxide and other species, closing the catalytic cycle in the process, removing electrons from the metal surface, oxidizing metal–hydride bonds, and regenerating hydroxide ions.

1.6. Hydrogenation of Furfural

The hydrogenation of FAL can generate several kinds of products such as furfuryl alcohol (FOL), tetrahydrofurfuryl alcohol (THFA), 2-methylfuran (2-MF), 2-methyltetrahydrofuran (2-MTHF), 1,4-pentanediol (1,4-PeD) , and 1,2-pentanediol (1,2-PeD) (Figure 1.10).

2-MF and 2-MTHF are promising biofuel components due to their high energy density, high research octane number and ideal boiling point. Nevertheless, FOL is the most important chemical derived from FAL, having a very broad spectrum of applications. 65% of the overall FAL produced is used in the production of FOL.[55]

FOL can be employed in diverse applications including the production of fine chemicals, resins, vitamin C, lysine, lubricants, fragrances, dispersing agents and plasticizers.[56,57]

Significant effort has been devoted to the preparation of FOL. The synthesis of FOL can be performed through the selective catalytic hydrogenation of furfural either in gas phase or in liquid phase, and has been carried out industrially for decades using based copper chromite catalysts.[58–60] However, harsh reaction conditions and production of large amounts of toxic waste has a negative economic and environmental impact on the process, thus the development of Cr-free catalysts is desirable.
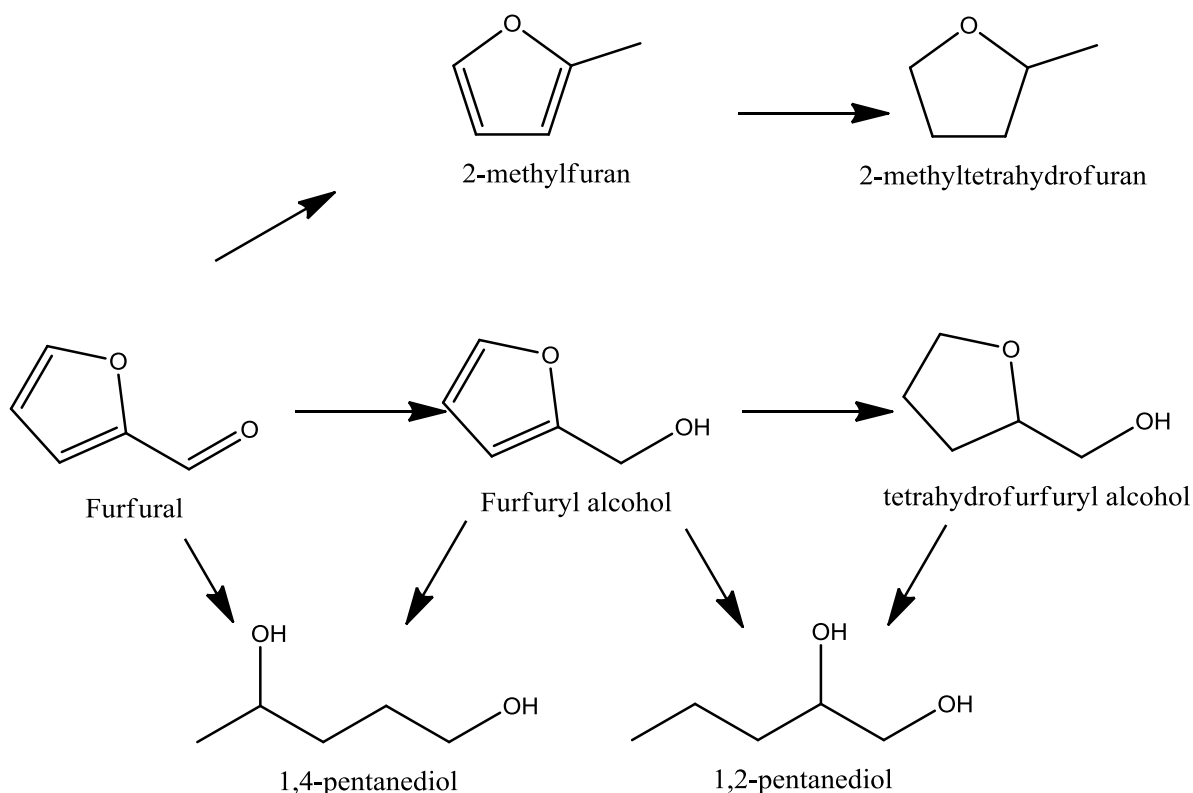
Figure 1.10 Reaction pathway for the hydrogenation of FAL.

The gas phase production of FOL has been reported by Kijenski et al.[61] using Pt based catalysts on oxide supports covered with transition metal oxide monolayers. 2% Pt/TiO$_2$ monolayer/SiO$_2$ system showed the higher selectivity (94%) and a 68.3% of conversion. Nagaraja et al.[62] studied the gas-phase FAL hydrogenation using Cu/MgO catalyst, and reported high conversion of furfural (98%) with high selectivity towards furfuryl alcohol (98%). However, such vapour phase hydrogenations are uneconomic owing to the high energy requirement for FAL vaporisation.

Liquid phase hydrogenation of FAL to FOL employing noble and non-noble metals has been explored, with the most promising heterogeneous catalysts reported to be based on Raney Ni[63], Mo doped Co-B amorphous alloys catalysts[64] and noble metals such as Pt[65], Ru[66,67], and Pd[68]. However, in most of the reported processes an organic solvent such as ethanol, methanol, propanol, butanol or octane, is employed, with few studies utilizing water as a solvent. Nakagawa and coworkers[69] reported silica supported Pd-Ir alloy catalysts for the aqueous-phase hydrogenation of FAL which while showing >99% conversion after 4 hours these exhibit low selectivity toward FOL, favouring THFA. High conversions of FAL were also obtained by Lesiak et al.[70] using alumina supported Pd-Cu nanoparticles, but also exhibited poor selectivity towards FOL even though relatively mild conditions of 90°C, 20 bar of H_2 were employed. A series of Pd-Cu/MgO catalysts for the selective hydrogenation of FAL in water were studied by Fulajtarova et al,[71] these were reported to exhibit complete conversion of FAL and >98% to FOL after 80 min of reaction, however elevated temperatures of 110°C and 6 bar of H_2 were employed

Recently Mironenko et al.[72] studied Pd and Ru catalysts supported on carbon nanotubes (CNT) and carbon black in the hydrogenation of FAL under mild conditions (50°C, 5 bar of H_2 and using water as solvent). Pd/CNT samples were the most active, attaining 97% of selectivity at a 40% of conversion. However, the Ru samples showed very low activity irrespective of the support nature and reaction conditions. This fact was attributed to water adsorbed on the ruthenium surface. H_2O–Ru interaction is much stronger than the H_2O–Pd one leading to lower activities.

Chen et al.[57] reported that graphitic carbon nitride nanosheet supported Pt exhibits high FAL conversion and high selectivity to FOL during hydrogenation in water at 100°C. The authors claimed that the large surface area of the support (142 $m^2 g^{-1}$) allows a uniform dispersion of the nanoparticles and hence, FAL adsorption ability on the nanosheets contributes to improved catalytic behaviour.

Full conversion of FAL and 100% selectivity to FOL was reported by Yang et al.[73] employing Ru nanoparticles supported on Al based metal-organic frameworks with benzene-dicarboxylic acid as linkers. FAL hydrogenation was performed in water at room temperature (20°C) at a pressure of H_2 of 5 bars. They suggested that in-situ reduction of Ru species occurs over the support surface accounting for the high activity observed. However, no recyclability test for the catalyst was reported and the metal: FAL ratio used was quite high.

In a recent publication[74] Ru-Sn alloys supported on activated carbon (AC) were presented as a promising catalyst for the aqueous-phase hydrogenation of FAL to FOL. While 90% conversion and 95% selectivity to FOL observed after 5 hours of reaction at 90°C very high metal:FAL ratios were required to achieve this high yield to FOL.

The high cost of Pt and Pd[75] and lack of more economically attractive and stable heterogeneous catalyst systems, had led to significant efforts being devoted to the development of more economically viable Ru based catalysts. Furthermore, for the development of a sustainable process, that could be translated into an industrial setting, these catalysts should be able to work effectively using water as solvent.[76] To stabilize highly dispersed Ru attention should also be paid to the effect of the support materials on catalytic performance.

Although the exact mechanism for the hydrogenation of FAL to FOL is not fully understood, Sharma et al.[77] proposed a mechanism for the hydrogenation of the C=O bond of FAL.

They suggested that the reaction takes place in several consecutives steps (Figure 1.11). In the first stage hydrogen molecule is adsorbed and decomposed into hydrogen atoms (proton and hydride) on the catalyst surface presenting hydrogen atoms available for bonding. Meanwhile, the lone pair present on the aldehydic oxygen is attracted and adsorbed on the catalyst surface. Subsequently, the C=O bond is hydrogenated selectively by the nucleophile hydride to form a hydroxyl alkyl intermediate which gives furfuryl alcohol after the addition of an activated hydrogen atom.
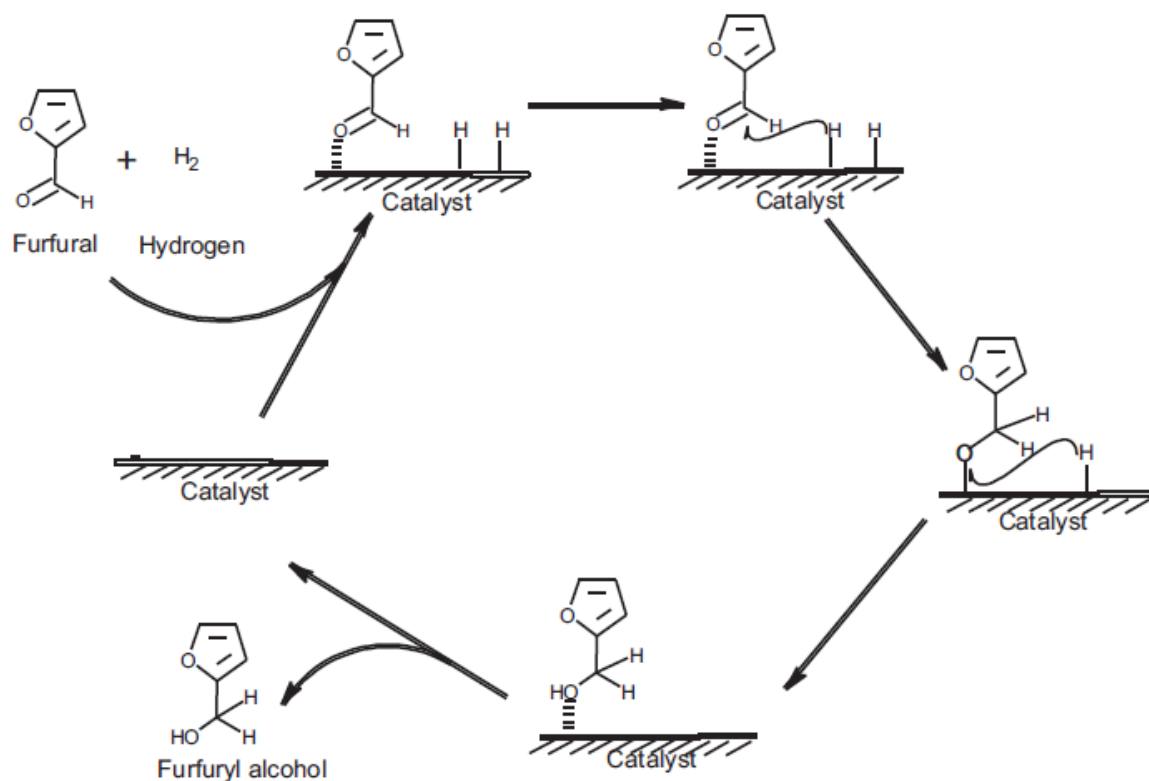
Figure 1.11 Reaction mechanism for the hydrogenation of FAL to FOL.[77]

1.7. Oxidation of Benzyl alcohol

Oxidation of alcohol to carbonyl compounds is one of the most important reactions for fine chemical industry. The oxidation of benzyl alcohol can generate benzaldehyde and benzoic acid (Figure 1.12).
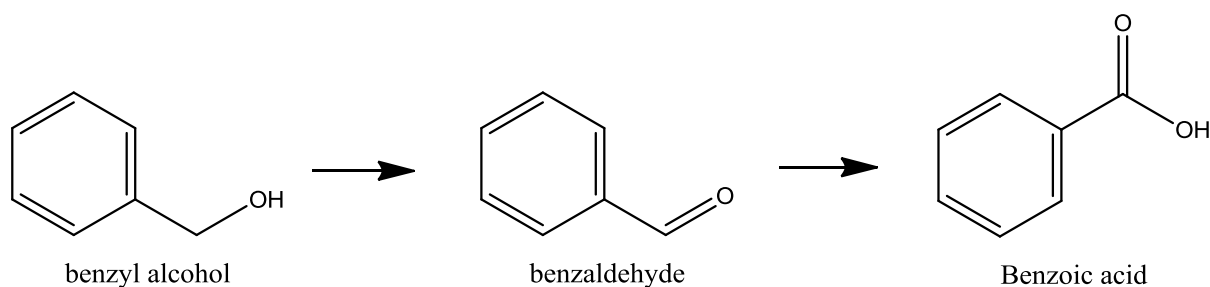
Figure 1.12 Reaction pathway for the oxidation of benzyl alcohol.

Benzaldehyde is the most industrially applied member of aromatic aldehydes. Benzaldehyde is a synthetic flavoring substance recognized as safe for foods by the United States Food and Drug Administration. It is also recognized as safe for use as bee repellant in the harvesting of honey. [78] It can be extensively employed as precursor and intermediate in the agrochemical, pharmaceutical and perfumery industries. Benzaldehyde is considered the second most important aromatic molecule used, after vanillin.[79]

Selective oxidation of benzyl alcohol to benzaldehyde is one of the most relevant transformations in chemical synthesis. Benzaldehyde is industrially produced via benzyl chloride hydrolysis derived from toluene chlorination or through toluene oxidation.[79] An extensive number of works have been devoted to the preparation of benzaldehyde from benzyl alcohol using greener oxidation routes to produce chlorine-free benzaldehyde required for perfumery and pharmaceutical industries. The traditional methods of oxidation of benzyl alcohol, reported the use of strong stoichiometric reagents like $KMnO_4$[80], chromites[81] or HNO_3[82]. It is well known, that these reagents are considered hazardous and generate a large amount of toxic waste, having a negative economic and environmental impact. Extensive

research regarding photocatalytic properties of different materials in the oxidation of benzyl alcohol has been reported[79,83,84] as a more relative efficient alternative to stoichiometric oxidants. Other oxidants, like peroxides [85–87] were proposed, however due to the handling risks associated with them[88], the use of molecular oxygen as oxidant is preferable. The use of heterogeneous metallic catalysts has been extensively studied. Nevertheless, most of the reported reaction procedures require the use of additives as NaOH[89], TEMPO[90,91], NaHCO$_3$[92], Na$_2$CO$_3$[93] or K$_2$CO$_3$[94,95].

The additive-free synthesis of benzaldehyde can be performed through the selective oxidation of benzyl alcohol either in gas phase[96,97] or in liquid phase using different types of metal catalysed processes. The solvent-free production of benzaldehyde has been reported by Choudary et al.[98] using non-noble transition metal based catalysts supported on hydrotalcite. Cu-Cr/HT system showed the higher conversion (51%) and 70% of selectivity toward benzaldehyde. Nevertheless, the main drawbacks of solvent-free oxidation are the high temperature needed to carry out the reaction (210ºC) and the undeniable deactivation of the catalysts in the recycling tests. In base to these previous results, Uphade et al.[99] proposed the use of Au nanoparticles supported on different materials to selectively produce benzaldehyde using a solvent-free strategy and molecular oxygen. The nano-size gold catalysts supported on U$_3$O$_8$ and MgO showed good conversions (53% and 51% respectively). However, a reduction in the selectivities can be immediately seen due to the formation of benzyl benzoate.

The liquid phase oxidation of benzyl alcohol to synthesize benzaldehyde employing Pd has been described along using different supports. Keresszegi and co-workers [53] reported Pd/Al_2O_3 catalysts showing yields >30% after 1.5 hours at 50ºC using cyclohexane as solvent. The catalytic processes occurred at the material surface were monitored in situ by ATR-IR spectroscopy. The in situ study of the solid-liquid interface revealed a complex reaction network and a remarkable catalyst deactivation due to a strongly adsorbed CO formed by decarbonylation of benzaldehyde and the formation of surface water due to side reactions leading to a blocking of the active sites.

Luque et al.[100] developed Pd nanoparticles supported on iron doped SBA15. Conversions of benzyl alcohol higher than 80% and high selectivity towards benzaldehyde were observed in the solvent free oxidation of benzyl alcohol at 85°C after 9h. A series of Pd and Pd-Au nanoparticles supported on nitrogen functionalized carbon nanotubes (CNT) catalysts for the selective oxidation of benzyl alcohol were studied by Villa et al.[101] They found that nitrogen functionalities incorporated by oxidation and further amination lead to an improvement in the TOF compared to pristine CNT. This enhancement was attributed to the increase of metal dispersion produced by nitrogen surface groups. Nevertheless, the solvent free samples presented poor selectivity toward benzaldehyde. When water was used as solvent the activities decreased. Nonetheless, the selectivities toward benzaldehyde were higher than the solvent-free tests. Along the same lines, 54% of conversion of benzyl alcohol and 90% of selectivity were also obtained by Wang et al.[102] using 8.6% Pd nanoparticles supported on N-doped CNT at 120ºC after 3h reaction. Hutchings and coworkers[103] demonstrated that the incorporation of Pd into Au nanoparticles create synergistic effects improving the catalytic

performance in the solvent-free oxidation of benzyl alcohol under mild conditions (100°C and 10 bar of O_2). 1%(Au-Pd)/TiO_2 samples prepared by sol immobilisation method were the more active, attaining 92% of selectivity at a 29% of conversion after 4 hours. Liu et al.[104] developed Pt nanoparticles supported on graphitic TiO_2. Complete selectivity towards benzaldehyde and 77% of conversion was observed in the oxidation of benzyl alcohol in water at 26°C after 10 hours. They claimed that the difference in the anatase content contributed to improve the catalytic behaviour. Despite its outstanding activity and selectivity, very low substrate: metal ratios were required to achieve this high yield to benzaldehyde. Provably due to Pt, Au and Pd high-cost[75] and the lack of more economically attractive and stable heterogeneous catalyst systems, some efforts have been devoted to the study of Ru as an alternative with lower cost and maintaining high catalytic efficiency. Full conversion of benzyl alcohol and 100% selectivity to benzaldehyde was achieved by Yamaguchi et al.[49] supporting Ru nanoparticles on Al_2O_3. Benzyl alcohol oxidation was performed in trifluorotoluene at 83°C and atmospheric pressure of O_2 during 1h. However, the benzyl alcohol:metal ratio used was very low and the uncompleted elimination of the NaOH used during the washing between recycling tests cannot be ruled out as a factor that could lead to effect masking effect of deactivation of the materials. The deactivation and regeneration of RuO_2 based catalysts supported on CNT has been described by Yu et al.[105] Although 75% of conversion with excellent benzaldehyde selectivity (>99%) was obtained after 1 hour, the samples showed significant deactivation in recycling tests. Besides, specially low benzyl alcohol:metal ratios were used. They determined that it was possible to regenerate the catalysts using a simple method based on treating the materials with hot water and drying

them overnight between runs, in order to eliminate the unfavourable adsorption of water in the active sites of the catalysts by surface reconstruction. In a recent publication[106] RuO_2 supported on NaY zeolites were presented as an alternative catalyst in the aerobic oxidation of benzyl alcohol to benzaldehyde. Nevertheless, the samples presented in the best case, 12% of conversion, the reaction being conducted during 3 hours at a temperature of 70°C in toluene and atmospheric pressure of O_2 using considerable small substrate:metal ratios.

The general mechanism for the oxidation of primary alcohols to aldehydes was described in section 1.5. It was suggested that the oxidation of an alcohol to an aldehyde over a heterogeneous catalyst likely occurs in three steps: metal alkoxide formation, β-hydride elimination to produce a carbonyl compound and a metal hydride, and oxidation of the metal hydride and regeneration of the metal surface.[47]

1.8. Carbon materials

Carbon materials such as activated carbons, carbon blacks, graphite, and graphitic materials play an important role in catalysis, either as active phases or supports[107,108] They have unique physical and chemical properties such as high surface area and well defined porosity, surface inertness, hydrophobicity and the possibility of tailoring their surface chemistry for specific applications through different chemical treatments.[108]

1.8.1. Structure and properties

The four valence electrons of the carbon atom endow it with an exceptional bond versatility, which allows it to form various organic and inorganic compounds. The electronic configuration of the carbon atom is ($1s_2 2s_2 2p_x 2p_y$). The outer electrons within the valence shell are involved in all chemical bonding features; they organize themselves to hybridize, forming linear (sp), planar (sp^2), or tetrahedral bonds (sp^3) with the electrons of neighbouring atoms. With these three hybrid orbitals, sp^3, sp^2, and sp, carbon atoms give rise to the formation of simple, double and triple bonds respectively.[107]

Due to this ability of carbon atoms to bond with each other in various ways, they can produce materials with a large range of properties.[108] Carbon forms different allotropes in solid state. These allotropes are composed entirely of carbon but have different physical structures.[107]

There are several allotropic forms of carbon materials (Figure 1.13): (1) flat sp^2 hybridization of carbon atoms in graphite. Graphite is comprised of sp^2 carbon atoms trigonally bonded to three neighboring carbon atoms in planar hexagonal rings (2) curved sp^2 hybridization in a fullerene or nanotubes, and (3) sp^3 hybridization in diamond, which is composed of sp^3 carbon atoms tetrahedrally bonded to four neighboring atoms. There are a few exotic allotropes, like lonsdaleite, which can be categorized as derivative of sp^3 carbon materials.[108]
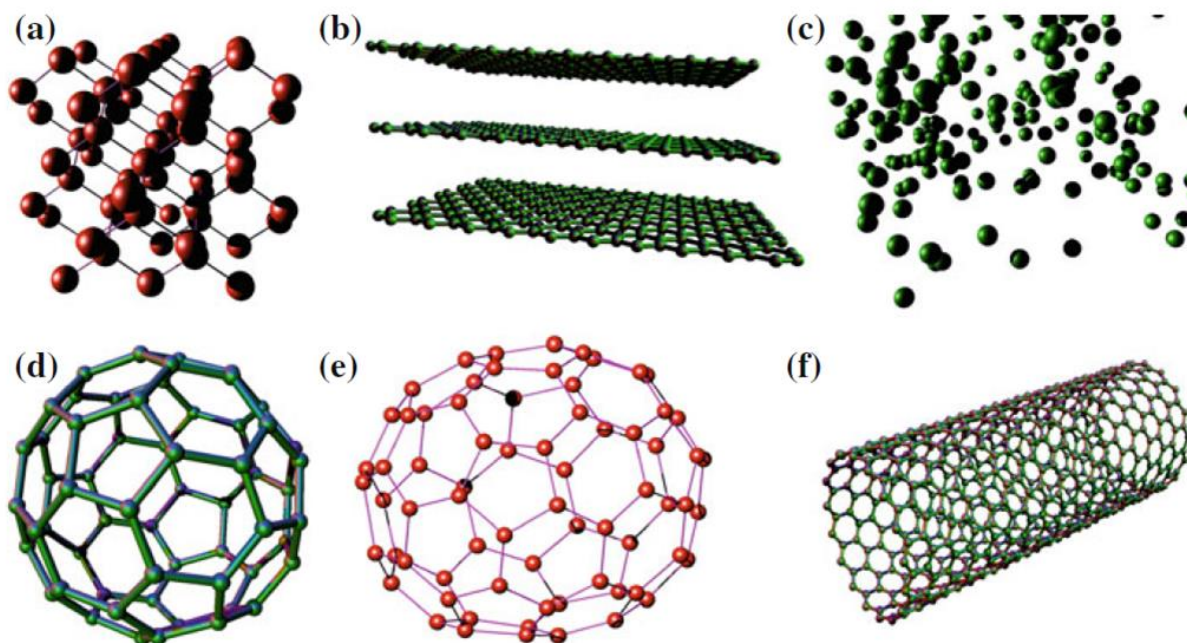
Figure 1.13 Carbon allotropes: a)Diamond, b)graphite, c) amorphous carbon, d) fullerene C60, e) fullerene C70, and f) Carbon nanotube.[109]

Surface properties of carbon materials are dependent on their structure. On these properties lie in carbon materials potential for catalytic applications.[108]

High surface area and a well-developed porosity are crucial properties of carbon materials. They exhibit surface areas significantly higher than other conventional oxide catalyst supports which allow them to attain high dispersions of metallic catalysts. However, must be highlighted, that in some carbon materials, especially AC, a great proportion of this surface area is mainly due to microporosity, being inaccessible to precursors or reactants.[107]

As seen above, surface area and porosity are very important factors in the preparation and properties of catalysts. However, the role of carbon surface chemistry is also extremely relevant.[110]Despite the presence of heteroatoms on the carbon surface could generate some type of active phase-support interaction, carbon material surface are less reactive compared to conventional oxide supports such as silica, alumina, titania, or ceria.[107] Thus, the carbon-active phase interaction is weak and the performance of the catalyst will be dependent of the chemical nature of the active phase. This fact allows studying the effect of adding other metals or promoters without undesirable effects with the support.[110] In the synthesis of bimetallic catalysts, the relative inertness of the carbon surface is very valuable, since the low interaction between the carbon surface and the two metals or metal precursors facilitates their mutual interaction.[108]

The interaction with other molecules and the chemical reactivity of basal and edge carbon atoms are considered different from one another. Due to the presence of surface functional groups at graphene edges, surface chemistry of carbon materials present a noteworthy flexibility. This is because of their unique proton-electron-, and oxygen-transfer characteristic. The reactivity of carbon materials is also linked to the presence of imperfections and defects along the edges of graphene layers which are the most active sites, owing to the high densities of unpaired electrons. Basal plane is not as chemically inert as is often believed due to the presence of delocalized unpaired electrons in the graphene sheet.[108]

Figure 1.14 shows the oxygen containing functionalities present on the surface of carbon materials (a) carboxyl groups, (b) lactone, (c) hydroxyl, (d) carbonyl, (e) quinone, (f) ether, (g) pyrone, (h) carboxylic anhydride, (i) chromene, (j) lactol, and (k) π electron density on carbon basal planes.
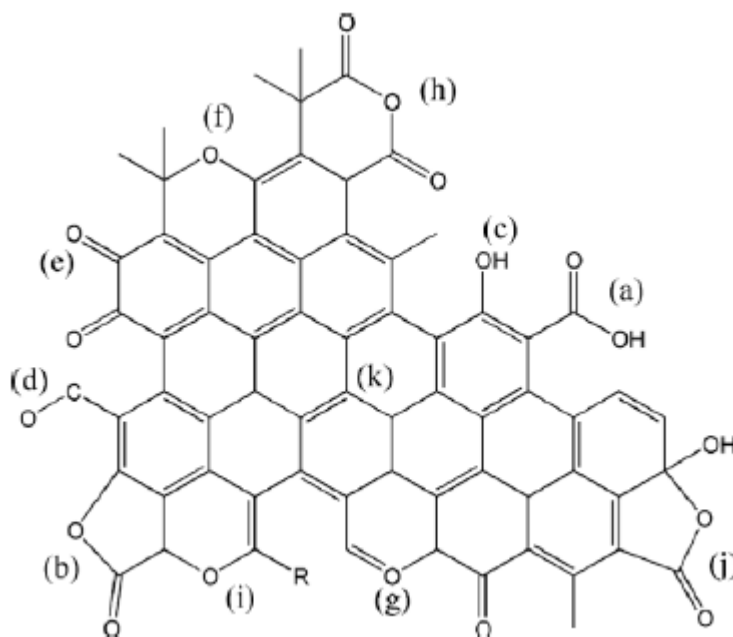
Figure 1.14 Oxigen containing funcionalities of carbon surface.[108]

Nitrogen-containing functionalities are not formed spontaneously on carbon surfaces by contact with air as with functionalities containing oxygen. Nitrogen can be introduced to the carbon matrix as component of the carbon precursors, such as carbazole or melamine. Another way of obtaining nitrogen doped carbon materials is by treatment of them with nitrogen containing reagents like ammonia or urea. The presence of nitrogen has been shown to be the key parameter for the behaviour of carbon materials as adsorbents, catalyst supports, or metal- free catalysts.[108]

Figure 1.15 shows the types of nitrogen-containing functionalities that can be found on the carbon materials: (a) pyrrole- like group; (b) nitrile; (c) secondary amine; (d) nitro group; (e) nitroso group; (f) terciary (g) amine; (h) pyridine-like group; (i) imine; (j) amide; (k) lactam; (l) pyridone; (m) quaternary amine.
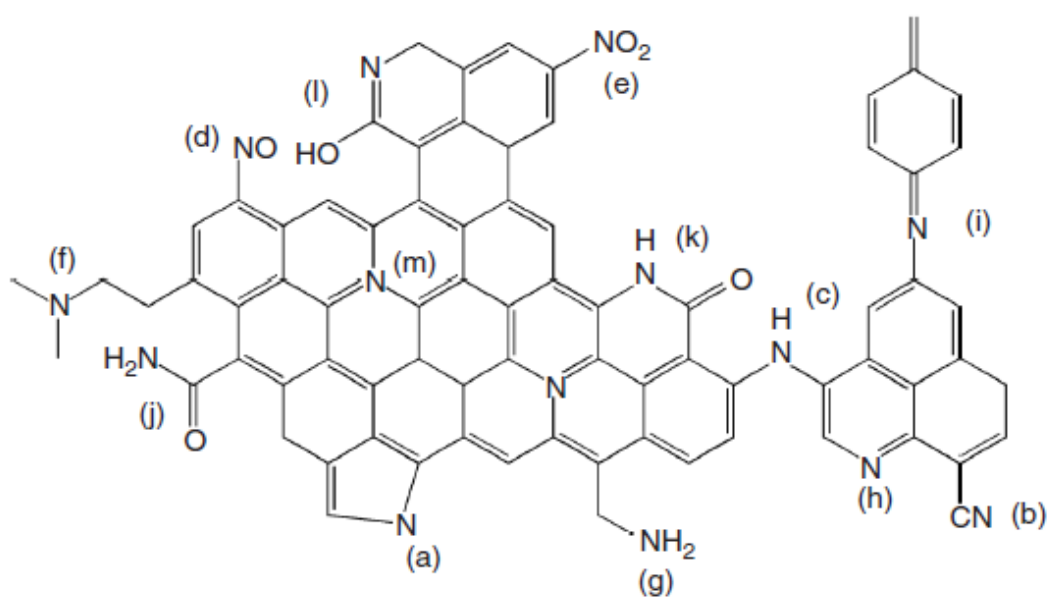
Figure 1.15 Nitrogen containing funcionalities of carbon surface.[108]

Carbon materials are usually hydrophobic, showing a low affinity towards polar solvents. However, the surface chemistry of carbon materials can easily be modified, for example by oxidation, to reduce their hydrophobicity and favour ionic exchange.[107]

Apart from an easily tailorable porous structure and surface chemistry, carbon materials present other advantages:

(i) metals on the support can be easily reduced;

(ii) the carbon structure is resistant to acidic or basic media;

(iii) the structure is stable at high temperatures (even above 750ºC under inert atmosphere); and

(iv) the cost of carbon supports is usually lower than conventional supports such as alumina and silica.[107,110]

1.8.2. High surface area graphite (HSAG)

High surface-area graphites (HSAG) are obtained by thermal treatment of the spherical carbon black particles at 2500-3000ºC and mechanical grinding. HSAG consists of small grains of crystallized structures. It possess well-ordered domains, and the mesopores, interparticle spaces, are the principal contribution to its porosity.[111] After a grinding process resulting surface areas are in the range of 100-500 m^2g^{-1}. These materials also exhibit high reactivity, specifically because of the unsaturated valences at the edges of the graphitic layers. They have been commonly used as supports for catalysts for diverse reactions, as oxygen reduction reaction in fuel cells, NO reduction, wet air oxidation, hydrogenations, hydrodechlorination and decomposition of NH_3.[107]
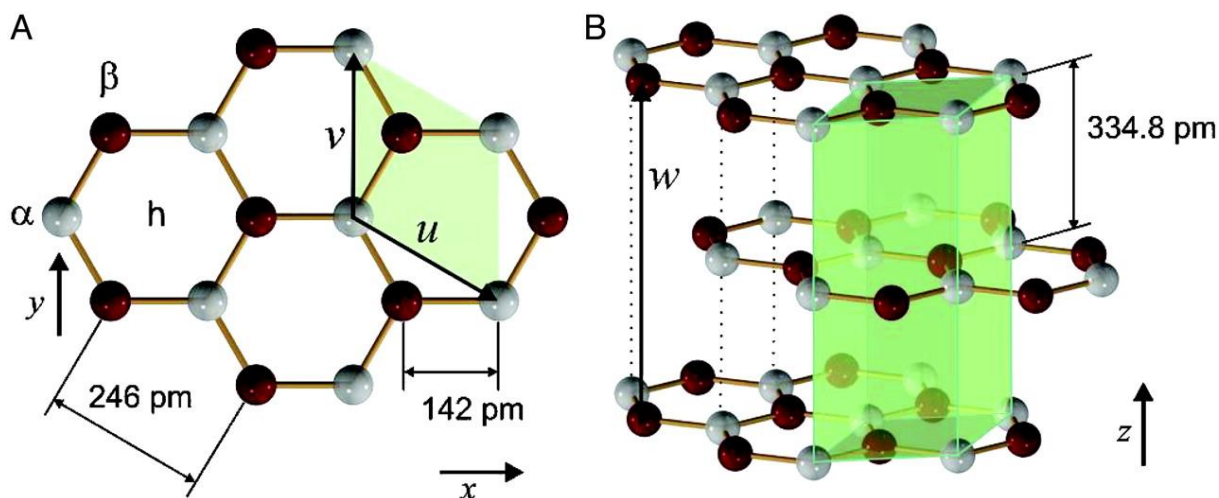
Figure 1.16 Schematic representation of the crystal structure of graphite. A) Top view on the surface layer. B) Perspective view, showing the layered structure.[112]

The hexagonal surface lattice is defined by two unit vectors (Figure 1.16), *u* and *v*, in the *xy* plane with a length of 246 pm and an angle of 120° forming a honeycomb structure of hexagonal rings. The α atoms (white) are directly above an α atom in the layer directly underneath at a distance of 334.8 pm; the β atoms (red) are over a hollow sites (h). The unit vector *w* is parallel to the *z*-axis with a length of 669.6 pm.[112]

1.8.3. Activated Carbon (AC)

Activated carbon (AC) is a term that defines a group of materials with highly developed internal surface area and porosity.[107] Activated carbons possess BET surface areas ranging from 400 to 2500 m^2g^{-1} and micropore volumes up to 1.2 cm^3g^{-1}, which makes them particularly attractive as adsorbents to be used in gas and liquid phase.[108] Consequently, activated carbons are the most common materials used as adsorbents.

The large surface area and high porosity of activated carbon catalysts make them also especially interesting to be used in catalysis, as they allow a good dispersion of the active phase over the support increasing its resistance to sintering at high metal loadings.[107]

The porosity of AC is a function of the precursor used in its preparation and the activation method followed and the degree of activation. Thus, the surface area and pore volume can vary widely from one type of AC to another. [113]

Another important feature of activated carbons is the variety of chemical properties of their surfaces which play an important role admitting the accommodation of molecules to be adsorbed or to undergo a targeted chemical reaction.[108] It is due to each carbon atom within a plane is linked to four adjacent carbon atoms. However, the atoms at the edges of the planes present a high availability and reactivity, allowing that the adsorption takes place.

AC is produced by pyrolysis of different carbonaceous materials such as coal, polymers, vegetables, etc.[111] The turbostratic structure of AC, which is based on the graphite lattice, corresponds to a non-graphitizable carbon. It is generally accepted that the average structure of AC can be represented as in Figure 1.17, consisting of irregular aromatic sheets, often bent, with variable spaces of molecular dimensions between them. Being these spaces the ones that contribute to develop the porosity. [113] This random ordering avoid that the structure give rise to graphite, even under thermal treatments of up to 3000°C, and in general are classified as non graphitizable carbon materials.

Figure 1.17 Schematic representation of activated carbon turbostratic microstructure.[113]

1.8.4. Reduced graphene oxide (rGO)

In the last few years there has been a growing interest in graphene due to its many outstanding electronic, thermal, chemical, and mechanical properties.[114] These properties give to graphene an enormous versatility. It can be extensively used in diverse applications including energy storage[115], electronics[116] and sensing device applications[117]. Graphenic materials have been widely employed as solid catalytic materials as well, either as active phases or as supports.[118] These catalytic applications strongly depend on its surface chemical properties.

Graphene is a 2-D material consisting of a one atom thick layer of graphite and it is based in sp^2 hybridized carbon atoms[107]. According to the number of sheets of graphene can be classified as single layer graphene or few layer graphene.

An extensive number of works have been devoted to the preparation of graphene. The synthesis of graphene can be performed using different methods, among them, micromechanical cleavage method[119], chemical vapour deposition (CVD)[120] and epitaxial growth on silicon carbide surfaces[121]. However, they show low productivity and lack of properties selectivity. One of the common approaches used for a large scale graphene production is based on the oxidation of graphite (G) flakes to produce graphite oxide (GO) [122,123], using strong oxidant agents (Figure 1.18). GO can be later exfoliated and converted to reduced graphene oxide (rGO) through a reduction procedure. The most used routes for the reduction of GO are chemical[124,125], electrochemical[126,127], solvothermal[128,129] and thermal treatments[130]. The use of thermal reduction is preferred over the rest of the methods due to its simplicity and industrial scalability.[131]

Even though the use of a single layer graphene as a catalytic support has not yet been reported, many promising results have already been obtained with few layer graphene [107] The properties of a defect-free single layer graphene are different to a few layer graphene, it is due to reduced graphene oxide presents considerable amount of defects, which disrupt the electronic and mechanical properties. Besides the dependency regarding the number of defects, most of the properties of this material are also dependent on the number of graphene layers present on the sample.[118] Thus, for example, the theoretical surface area of graphene is 2600 m^2g^{-1}, however for a sample of few layer graphene this value is reduced according at the number of layer presents on the sample.[132]

From a practical point of view, this thesis refers to few layer graphene as reduced graphene oxide (rGO) which is an infinite three-dimensional material made up of stacked layers of graphene.
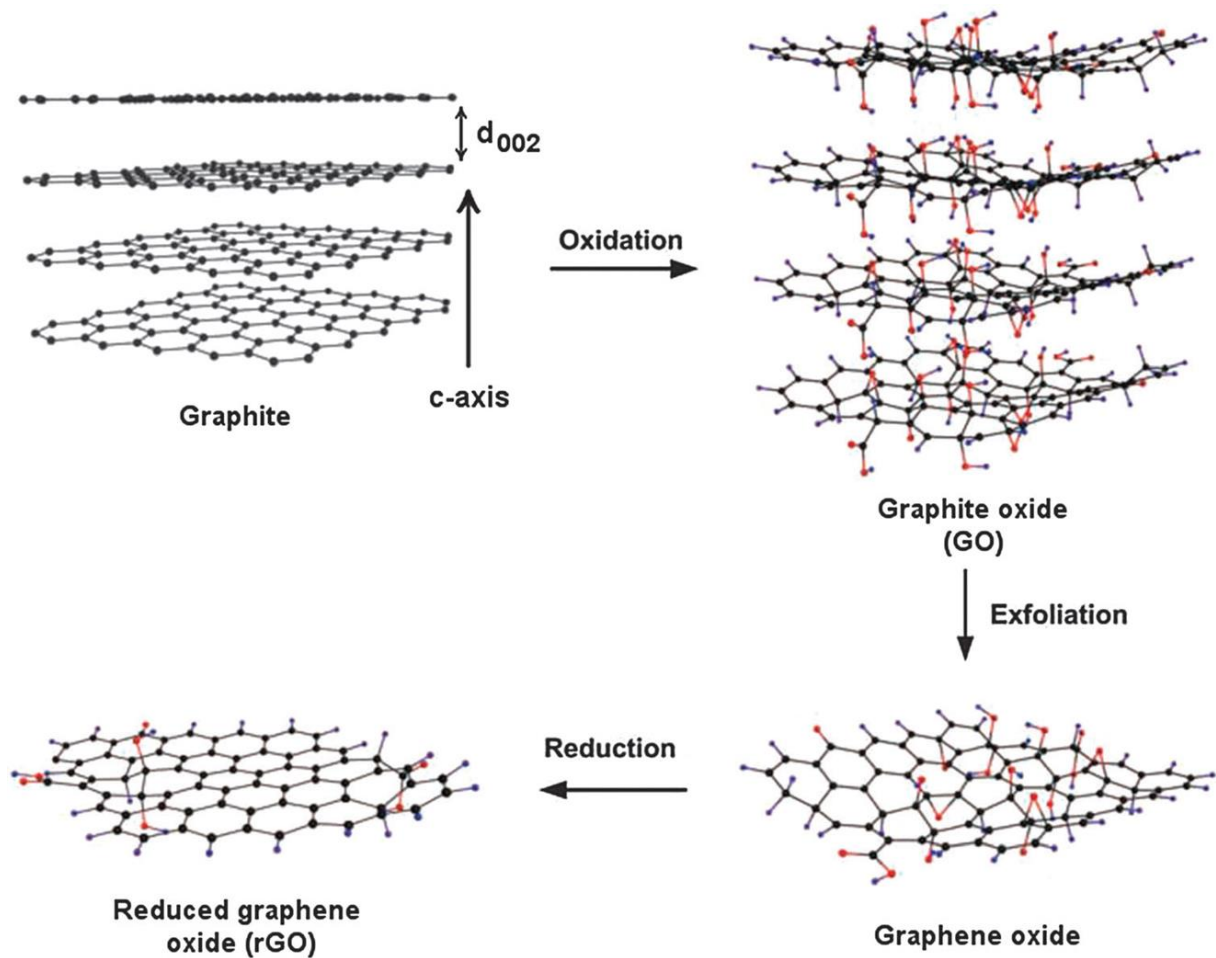
Figure 1.18 Preparation of reduced graphene oxide. [118]

1.8.5. Nitrogen doped reduced graphene oxide (NrGO)

It is well known that the surface chemical properties of graphenic materials can be tuned by covalent added adatoms.[108] Thus, the presence of nitrogen or boron atoms in the basal planes of graphene layers produce changes of many of their chemical properties. It was demonstrated that the doping of nitrogen into a graphenic structure modify their chemical and electrical properties, introducing basic properties to the carbon materials surfaces.[133] N presence improves electronic density of the graphenic layer producing a higher positive charge on a carbon atom adjacent to the nitrogen atom, this is due to presence of five electrons of valence in the nitrogen versus four valence electrons in carbon atoms. This fact incorporate one more electron into the graphenic layer and becoming more basic.[134,135] The possibility of acting on the surface chemical properties and the high specific surface area of graphenic materials, make them highly promising materials in this field.

Nitrogen can be introduced in different ways into the carbon matrix, giving rise to different functionalities, which in turn provide different properties to the material (Figure 1.15). It is possible to find in the graphitic matrix of NrGO at least three types of nitrogen [136]: pyrrolic-N (Figure 1.15 a), pyridinic-N (Figure 1.15 h), and quaternary-N (Figure 1.15 m).

The relative abundance and chemical environment of N-containing functionalities is expected to determine the NrGO acid/base properties. The basic character of NrGO can be attributed likely to the presence of pyridinic-N.[137] To explain this fact, attention can be focused on quaternary-N and the pyrrolic-N: sp^2 hybridized quaternary-N replaces a C atom in the graphitic matrix and it contributes with one additional electron to the aromaticity of the conjugated π system, producing a delocalization of the electrons of the N atom. Therefore, the donation of an electron by the N when accepting a H^+ would be energetically unfavourable because it would destabilize the system by decreasing aromaticity. Therefore, quaternary nitrogen groups would not contribute to basicity.[107]

The sp^3 hybridized pyrrolic nitrogen atom is also part of an aromatic matrix. The protonation of the nitrogen atom, in the same way that quaternary-N requires donation of one electron to the H^+ ion, and it would produce a loss of the aromaticity of the ring, which is energetically unfavorable for the stability of the structure.[107]

Based on the foregoing, the pyridinic-N with its free electron pair can act as Lewis base and Bronsted base, being the only type of N of the aforementioned able to interact favourably with a H^+.[107] N-O species, which are an oxidized form of pyridinic-N, may also appear. These present acid character, with reported pKa values below 3.[107]

Incorporation of nitrogen in graphenic materials to produce N doped reduced graphene oxide (NrGO) has been described using several methods as well. For example CVD using NH_3[138], acetonitrile[139] or pyridine[140] as N source, arc discharge of graphite[141] in presence of pyridine or NH_3, nitrogen plasma treatment of graphene[142], and thermal treatment of GO with melamine[143,144], urea[145] or NH_3[135,146].

1.8.6. Tailoring of properties of rGO and NrGO

The improvement of some of the properties of rGO and NrGO has been undertaken using different synthetic strategies.

Wu et al.[147] studied a chemical exfoliation of GO to produce graphene with a selective number of layers based on different starting materials as pyrolytic graphite, natural flake graphite, kish graphite, flake graphite powder and artificial graphite. They reported the effect of the lateral size and crystallinity of these starting graphite materials on the number of graphene layers presented in the obtained graphenic material. They found that graphite samples with a small lateral size and low crystallinity produce a higher proportion of single layer graphene.

Li et al.[146] obtained NrGO through thermal annealing of GO in NH_3 screening temperatures between 300 and 1100 °C. Annealing at 500 °C afforded the highest N-doping level of ~5% showing the strong influence of the temperature on the nitrogen content of the obtained materials. They claim that N- doping degree depends on the amounts of oxygen functional groups of graphene as they are responsible for the formation of C−N bonds. The higher the annealing temperature is, the lower the content of oxygen, leading to a lower reactivity between graphene layer and NH_3.

The production of NrGO based on annealing of GO in the presence of melamine at high temperature (700−1000 °C) has been reported by Sheng et al.[148] They noted that nitrogen content depends on mass ratio between GO and melamine as well as on the temperature, reaching values of 10.1% using a 1:5 ratio of GO to melamine at 700ºC. A similar approach was used by Canty et al.[145] working with urea and GO as precursor materials of NrGO, they used the ratio of GO to urea as a way to control the amount of nitrogen inserted and the surface area values obtained. Nonetheless, neither Li nor Canty reported a systematic study of the synthesis conditions to optimize NrGO properties.

Menendez's group[131] analysed the effect of the experimental conditions of the thermal transformation of GO onto rGO, finding that the treatment temperatures strongly affect the type and amount of functional groups obtained. Following this line of research they proposed that the temperature of the initial flash thermal treatment allows the control of the surface area obtained.[149] However, the surface area values achieved were lower than 500 m^2g^1.

Zhang et al.[150] proposed a vacuum promoted thermal exfoliation method for different samples of GO, obtained from natural flake graphites with particle sizes arranging from 100 to 5000 mesh. Nevertheless, neither the morphology nor the structures of different graphene samples were affected by parent graphite particle size. Surface areas observed were around 490 m^2g^{-1} and the C/O ratio determined by XPS analysis revealed that all the samples had almost the same oxygen content. Whereby, the vacuum-promoted exfoliation method minimizes the differences originated from the raw graphite particle size.

The effect of raw graphite size on rGO properties has been also described by Dao et al.[151]. They prepared rGO by rapid heating of dry GO using three graphite particle sizes obtained grinding a large size graphite sample. An increase in the surface area was observed as the particle size of the samples reduced, reaching a value of 739 m^2g^{-1} in their best sample. This improvement was explained as due to a better oxidation degree achieved with the decrease of the graphite particle size that favours a better exfoliation of the GO. On the other hand a previous study of Asedegbega et al. [133] reported the synthesis of NrGO from GO obtained from three different graphite particle sizes. Also they found that the quantity of nitrogen and the surface properties obtained were dependent on the particle size of the graphite used. However, the surface areas obtained were not enough optimized.

OBJECTIVES

2. OBJECTIVES

As previously stated, special consideration must be paid to the effect induced by the surface functional groups exposed at the surfaces of graphenic materials over their properties. More precisely, it has been demonstrated that the incorporation of N into graphenic materials change their chemical and electrical properties. It is due to the fact that N presence improves electronic density of the carbon material incorporating by one more electron into the carbon surface becoming more basic. [134] Thus N-doped materials have been gaining increasing interest in catalysis.

Guerrero et al. were the first ones that studied the differences induced by the introduction of nitrogen functional groups in the carbon surface. They found that these groups could affect the metal crystallite size, morphology or reductivity. Nitrogen groups could also involve a change in the electronic properties of the metal particles, as a consequence of a metal-support interaction, induced by the difference in the electron density of the carbon produced. [152]

In a recent work, Fujita et al.[153] reviewed N-doped carbon materials since the preparation of N-doped AC reported by Störh et al. in 1991 from a commercial AC by thermal treatments with ammonia and hydrogen cyanide. They go over the different applications of N-doped materials as catalysts or catalysts supports, remarking their superior activities in a wide range of reactions as Knoevenagel condensation of benzaldehyde and ethyl cyanoacetate, transesterification of ethyl acetate and methanol hydrogenations and oxidations.

To date, N-doped carbon materials, as of N-graphenes[154,155] and N-carbon nanotubes[156,157], have also been studied. However, the emphasis of most of the works was largely placed on the applications for energy conversion and storage, with less focus on for catalytic reactions, particularly catalytic hydrogenations and oxidations.[158] Therefore, it is required to further investigate the tailoring of the properties of N-doped carbon materials to prepare more effective catalysts.

There is a need of simultaneous and systematic reports regarding the combined effect of raw graphite size and the conditions of the thermal treatment (heating rate and temperature) in the properties of graphene and N-doped graphene, particularly, surface area and content of nitrogen. The optimization of these parameters in the graphenic materials is crucial due to the impact of these properties in the potential utilization of graphenic materials in multiple applications[159], but particularly as free metal heterogeneous catalysts or catalytic supports. Deserves significant attention the effect produced by the supports over the catalytic behaviour of supported metallic catalyst as well.

As mentioned above, there are many routes of conversion of platform molecules into valuable chemicals and fuels. Valorisation of biomass-derived compounds, including 5-hdyroxymethylfurfural, furfural, and benzyl alcohol, into value-added chemicals requires economically attractive, efficient and stable heterogeneous catalyst systems. Ru based catalysts, can be a viable alternative as Ru is cheaper than Au, Pd and Pt.[160]

The main objective of this Doctoral Thesis is the development of new nanomaterials; consisting of N-doped and non-doped graphenic materials with tailored properties and Ru nanoparticles (NPs), and comprehend the effect of N-doped surface groups of graphenic materials on Ru NPs and how support properties can affect the catalytic performance of these catalysts in a series of representative reactions of conversion of biomass.

As specific objectives for the preparation of materials are postulated:

- The synthesis of graphene materials (rGO) and nitrogen doped graphene materials (NrGO) using three different particle sizes of starting graphite and applying various thermal treatments.
- Carry out a deep characterization of the graphenic materials in order to study the influence of the combined effect of raw graphite size and the conditions of the thermal treatment in their properties and to optimize these properties, particularly, surface area and content of nitrogen.
- Application of the optimized graphenic materials (rGO and NrGO) as support of Ru, Cu, Ag and Cu nanoparticles.
- Comparatively investigate the preparation and characterization of Ru based catalysts supported on commercial materials as activated carbon, high surface area graphite, Al_2O_3, SiO_2 and TiO_2.

- Perform a deep characterization of the metallic catalyst to comprehend how parameters such as nature of the support, metallic precursor, and reduction temperature affect their properties.

As specific objectives for the catalytic application of the materials are postulated:

- Study of the catalytic performance of the Ru-based catalysts for the conversion of a series of biomass-derived compounds, including:
  - ✓ The base free aqueous-phase oxidation of 5-hydroxymethylfurfural to 2,5-Furandicarboxylic acid.
  - ✓ The aqueous-phase hydrogenation of furfural to furfuryl alcohol.
  - ✓ The selective oxidation of benzyl alcohol to benzaldehyde using molecular oxygen as an oxidizing agent under base-free mild conditions.
- Systematic comparisons of the impact of support properties and Ru NPs characterization, to correlate the catalytic results obtained with the effect exerted by the support on Ru NPs.
- Comparatively investigate the catalytic behaviour of Ru based catalysts with other metals such as Cu, Au and Ag
- Study of the catalytic stability and recyclability of the Ru-based catalysts for the aforementioned reactions to assess the suitability for a tentative industrial application

EXPERIMENTAL

3. EXPERIMENTAL

This chapter describes the preparation of the studied supports and catalysts, as well as the characterization techniques used to know their most relevant structural and surface properties. It also includes the description of the experimental systems and the measurement methods used in the reactions studied.

3.1. Preparation of supports

3.1.1. rGO and NrGO

Graphenic materials were obtained via thermal treatment of graphite oxide (GO). GO was synthesized from natural graphite powders (10 mesh, 100 mesh and 325 mesh) supplied by Alfa Aesar (purity 99.8%) following a modification of the Brodie's method.[123] This procedure is as follows: 10 g of graphite (G) were added to 200 mL of fuming HNO_3 kept at 0 °C in the reaction flask. 80 g of $KClO_3$ were slowly added during 2 hours. Thereafter, the mixture was stirred for 21 h maintaining the temperature. The resulting GO was filtered and washed thoroughly with deionized water until neutral pH and dried under vacuum to constant weight in a desiccator over P_2O_5 at room temperature. The resultant samples were labelled GO_m, where m indicates the mesh size used.

Exfoliation of the synthesized GO was carried out in a vertical quartz reactor. Two exfoliation atmospheres have been applied. One where GO was heated under nitrogen gas (87 mL/min) (yielding rGO) while the second consists in passing a mixture of NH_3, H_2 and N_2 with flow rates of 10, 3 and 87 mL/min (giving NrGO).

In order to study the effect of temperature and heating rate on the properties of rGO and NrGO, for each atmosphere described, five different exfoliation ramps have been applied over GO_{325}.

In a first ramp, 0.3 g of GO was introduced in the furnace and heated at 5 ℃ min^{-1} to 250 ℃, the samples being then kept at this temperature for 30 minutes. The temperature was increased up from 250 to 500ºC with a heating rate of 5ºC/min and then kept at this temperature for 30 minutes.

In a second and third ramp, GO was heated at 5 ℃ min^{-1} and 10ºC/min respectively to 250 ºC, the samples being then kept at this temperature for 30 minutes. The temperature was increased up from 250 to 700ºC using the same heating rates, and then kept at this temperature for 30 minutes.

In a fourth ramp, GO was heated at 5 ℃ min^{-1} to 100 ℃, the samples being then kept at this temperature for 1 hour. The temperature was increased up from 100 to 700ºC with a heating rate of 10ºC/min and then kept at this temperature for 5 minutes.

Finally the fifth ramp involves: GO was heated at 20ºC min^{-1} to 250 ℃, the samples being then kept at this temperature for 30 minutes. The temperature was increased up from 250 to 500ºC with a heating rate of 20ºC/min and then kept at this temperature for 30 minutes.

For the exfoliation of the samples GO_{10} and GO_{100}, the temperature and heating rate used were selected using the ramp that gave the higher values of surface area for the exfoliated samples of GO_{325}. The samples obtained were labelled rGO_m-r and $NrGO_m$-r respectively, where m indicates the mesh size used and r the ramp used.

3.1.2. Commercial materials

Apart from the lab prepared graphenic materials five commercial supports were also employed as support of Ru metallic nanoparticles. These are: SiO_2, TiO_2, Al_2O_3, activated carbon, and high surface area graphite. The activated carbon (denoted as AC, $S_{BET} = 1190$ m^2g^{-1}, 313 m^2g^{-1} external surface area by t-plot method) was provided by Oleicola el Tejar, Córdoba Spain, while SiO_2 ($S_{BET} = 465$ m^2g^{-1}) was obtained from Fluka, P25 TiO_2 ($S_{BET} = 50$ m^2g^{-1}) and Al_2O_3 ($S_{BET} = 187$ m^2g^{-1}) from Degussa. Finally the high surface area graphite material ($HSAG_{400}$, $S_{BET} = 396$ m^2g^{-1}) was supplied by TIMCAL. Prior to catalyst preparation, the as received activated-carbon was treated with hydrochloric acid solution 10% (v/v) at 373 K for 24 h to remove residual inorganic materials and then it was successively washed with deionized water at reflux temperature and dried at 393 K.

3.2. Preparation of catalyst

All supported Ru catalyst were prepared in order to obtain samples with ruthenium loading of 4 wt.%. Three different precursors were used in the catalyst preparation. $Ru_3(CO)_{12}$ (catalyst series denoted with "CO") was incorporated in the supports by wetness impregnation, once dissolved the exact amount in acetone. The solvent was removed under reduced pressure on a rotary evaporator at about 50ºC during at least 30 minutes. Two other series of Ru catalyst were prepared, using $RuCl_3$ as precursor (series denoted as "Cl") or using $Ru(NO)(NO_3)_3$ (series labeled with "NN"). For these two series the graphenic materials were impregnated by incipient wetness impregnation method. The metal precursors were dissolved, in both cases, into a water:ethanol (1:1) solution. After evaporation of solvent by keeping the solids overnight in an open recipient at room temperature, the samples were dried at 100ºC for 24 h. Finally, before characterization and catalytic tests the catalysts were activated by reduction under hydrogen flow (60 mL min^{-1}) at 350ºC or 300ºC for 2 h., in order to decompose the precursor and assure their initial metallic state. Once the reduced samples are at room temperature a helium flow (50 mL min^{-1}) is passed for 5 h in order to passivate the metallic surfaces. The reduced/passivated catalysts were exposed and stored under air up to their evaluation in reaction or the characterization studies.

4 wt.% Ag and 2 wt.% Cu catalysts supported on rGO and NrGO were prepared, using

$AgNO_3$ and $CuNO_3$ as precursors, respectively. The graphenic materials were impregnated by

incipient wetness impregnation method. The metal precursors were dissolved, in both cases,

into a water:ethanol (1:1) solution. After evaporation of solvent by keeping the solids

overnight in an open recipient at room temperature, the samples were dried at 100ºC for 24 h.

Finally, before characterization and catalytic tests the catalysts were activated by reduction

and treated as in the case of Ru catalysts, described above.

Au/rGO and Au/NrGO catalysts were prepared by the method reported by Dobrzanski et al[161]

in order to obtain samples with gold loading of 1 wt.%. Firstly 0.5 mL of 0.01M

$HAuCl_4.3H_2O$ and 0.5 mL of 0.01M sodium citrate monobasic solution were mixed with 18.4

mL of deionized water. Then 0.6 mL of 0.1 M $NaBH_4$ solution was added under intensive

stirring. The measured amount of support was immersed into the gold suspension and mixed

with ethanol (5 mL of ethanol each 10 ml gold suspension). After ultrasonic dispersion

followed by stirring for 15 h, the black solid was separated and washed with water (600 mL)

and dried overnight at 78℃.

3.3. Material characterizations

This section briefly describes the foundations of the characterization methods employed over

the development of this work.

3.3.1. Nitrogen adsorption-desorption isotherms

Any solid can adsorb molecules or atoms on its surface. Considering how strong a species can be adsorbed on the surface, two cases can be distinguished: physical adsorption or physisorption, characterized by a weak interaction with the surface, which can take place at any point on the surface; and chemical adsorption or chemisorption, in which a chemical bond is created between the substrate and the adsorbate, having specificity the adsorption on some reactive superficial sites of the material under study.

The physical adsorption of gases is the most usual technique for the determination of the total area and distribution of pore sizes in solids. Brunauer, Emmet and Teller developed and published in 1938[162]a method (BET method), that is based on nitrogen adsorption at liquid nitrogen temperature (-196ºC). The obtained isotherms (representation of the volume of nitrogen physisorbed in the solid as a function of the relative equilibrium pressure of nitrogen) correspond to the process of adsorption and desorption of the gas in the solid. IUPAC classifies the isotherms in six types (Figure 3.1), which correspond to limiting cases for nonporous or macroporous solids (Type II), nonporous or macroporous solids with low interactions surface-adsorbate (Type III), mesoporous solids (Type IV), mesoporous solids with low interactions surface-adsorbate (Type V), and an infrequent isotherm characteristic of extremely well ordered nonporous systems such as graphite systems where adsorption occurs layer by layer (Type VI). Microporous solids usually give rise to Type I isotherms characterized by an increase in amount adsorbed at low pressure, corresponding to filling of the micropores, followed by a distinctive plateau. The hysteresis loops observed for the Type

IV and Type V isotherms correspond to a capillary condensation phenomena associated with the mesporosity.[163]
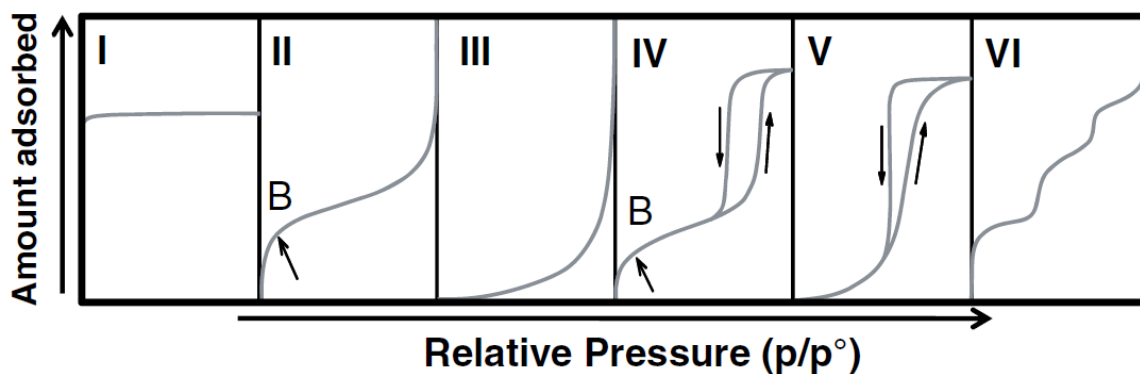
Figure 3.1 Classification of the isotherms according to IUPAC.[163]

For the determination of surface area values (m^2g^{-1}), the BET equation is widely used, since it allows estimating the total surface area of a sample from the amount of gas adsorbed when a monolayer is forming, knowing the area occupied by each one of the adsorbed molecules.[164] This method therefore implies the application of the BET equation:

$$\frac{p}{V(p_0 - p)} = \frac{1}{V_m C} + \frac{(C-1)}{V_m C} \times \frac{p}{p_0}$$

Where V is the specific volume of gas adsorbed to the relative equilibrium pressure p/p_0, V_m is the monolayer saturation adsorption quantity, p_0 is the saturated vapour pressure of adsorbate at adsorption temperature and C is a constant.

73

Representing p/V(p$_0$-p)n as a function of p/p$_0$ a straight line is obtained. From the slope

m=(C-1)/(V$_m$C) and intercept b=1/V$_m$C, the values of the V$_m$, from which the specific surface

is calculated, and the constant C can be obtained.

$$V_m = \frac{1}{m + b}$$

The surface area (S) of the sample (BET area) is determined from the expression:

$$S = A_m V_m \frac{N_A}{22414}$$

Where A$_m$ is the section area occupied by each molecule of adsorbate, being according to

IUPAC[165], 0,162 nm^2 for nitrogen; N$_A$ is the Avogadro's constant

For non-porous and mesoporous materials the BET equation is valid for a linear region in the

BET plot between p/p$_0$ =0.05 and 0.35 approximately. In the case of microporous solids, this

linear region will be found at a much lower region of p/p$_0$ often below 0.05.[163]

All the supports were analyzed using a Micromeritics ASAP 2020 system. Samples were

previously degassed at 150ºC for 16 h in a vacuum system for removing all physisorbed

species retained in the pores and external surface

3.3.2. X-ray diffraction (XRD)

X-ray diffraction is one of the oldest and most frequently applied techniques in catalyst characterization. It is based on the use of a monochromatic X rays and allows to obtain many useful structural information from the catalyst or the support. Thanks to XRD is possible to identify crystalline phases inside catalysts by means of lattice structural parameters, and to obtain an indication of particle size according to the diffraction of the direction in space, intensity and width.[164]

When X-rays are applied on a solid sample, its layers of periodically spaced atoms in the crystalline structure act like a diffraction grating. X-rays scattered by atoms interfere constructively in directions given by Bragg's law (Figure 3.2), giving rise to a diffraction line pattern where each line of the diffractogram is associated to concrete planes and specific to the material. In order to generate interference patterns, only the scattered monochromatic X-rays that are in phase give constructive interference are detected.
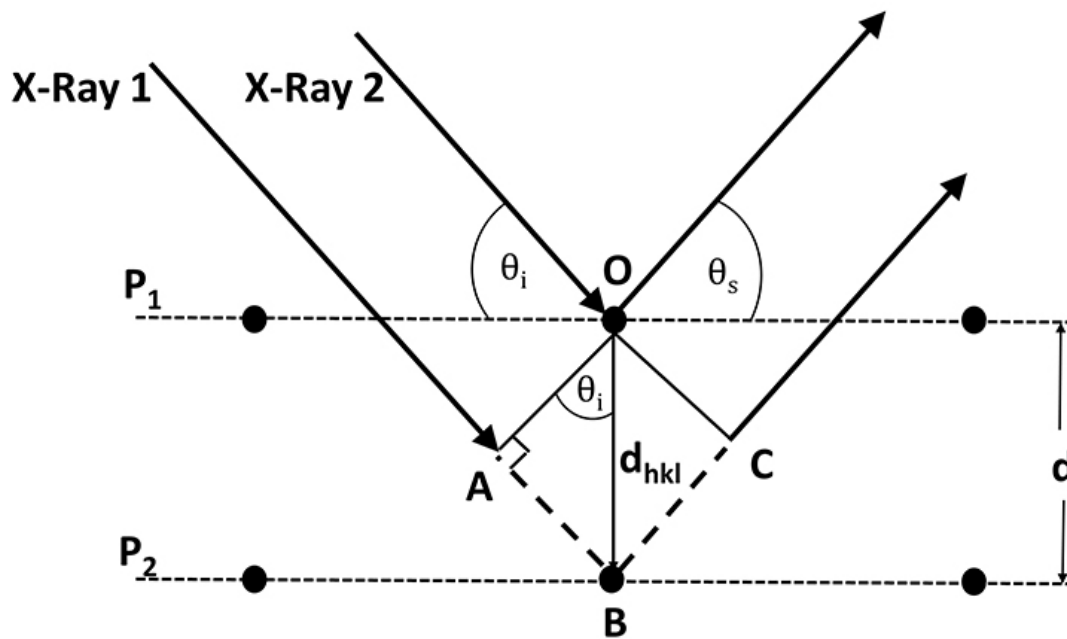
Figure 3.2 Schematic representation of x-ray diffraction.[166]

Constructive interference must satisfy the relation: $AB + BC = n\,\lambda$. Being $AB = d_{hkl}\sin(\theta_i)$ and $BC = d_{hkl}\sin(\theta_s)$, it leads to Bragg's law:

$$n\lambda = 2d\sin\theta; \quad n = 1, 2, \ldots$$

where λ is the wavelength of the X-rays, d is the distance between two lattice planes, θ is the angle between the incoming X-rays and the normal to the reflecting lattice plane, n is an integer called the order of the reflection.

Using the Bragg's law the angles, 2θ, of maximum intensity enable to calculate the spacing between the lattice planes[163,167]

The Scherrer formula relates crystal size to line width:

$$< L >= \frac{K\lambda}{\beta\cos\theta}$$

in which <L> is a measure of the dimension of the particle in the direction perpendicular to the reflecting plane, λ is the X-ray wavelength, β is the line broadening after subtracting the instrumental line broadening , θ is the angle between the beam and the normal to the reflecting plane, and K is a dimensionless constant.[167]

X-Ray diffraction has an important limitation: diffraction peaks are only observed when the sample possesses sufficient long-range order. Therefore, XRD cannot detect particles that are either too small or amorphous.[167]

The samples were analyzed using a Polycristal X'Pert Pro PANalytical diffractometer with Ni-filtered Cu/K radiation (λ = 1.54 Å) operating at 45 kV and 40 mA. For each sample, Bragg's angles between 4º and 90º were scanned at a rate of $0.04º s^{-1}$.

3.3.3. Elemental analysis (EA)

The determination of the carbon, hydrogen, nitrogen and sulfur of carbon samples is based on their combustion at high temperatures (900-1200ºC) under a stream of oxygen. The products of combustion are converted to gas molecules (CO_2, SO_2 and H_2O) and carried by an inert gas to be detected directly by selective sensors.

Nitrogen present in the sample is reduced to N_2 in an oven containing copper and it is quantified later by differential thermoconductivity after elimination of the remaining combustion gases, the signal of the output line is compared with a reference cell containing a flow of inert gas, the potential difference between the two cells is correlated to the amount of N_2 in the sample.[108,168]

The analyses were carried out using a Leco CHNS-932 system (Servicio Interdepartamental de investigación, Universidad Autónoma de Madrid). To analyze the samples, they are previously dried to eliminate errors due to the presence of solvents or water.

3.3.4. X-ray photoelectron spectroscopy (XPS)

XPS spectroscopy is based on the photoelectric effect. This technique consists in exciting a material with X-ray photons, extracting electrons from the internal levels of the atoms of the material studied. The incident photons have a higher binding energy than the electrons in the sample, since this energy must be overcome in order to pull them out. The measurement of the kinetic energy (Ek) of the electrons removed allows to calculate the bond energy of the electrons (Eb) since the incident energy (hv) of the photons is known. The excited electrons follow the equation of the photoelectric effect:

$$E_k = h\nu - E_b - \Phi$$

Being Φ the working function of the spectrometer, a correction factor which represents the minimum energy required to impulse one electron towards the highest level occupied in the vacuum.

The process of photoemission is shown schematically in Figure 3.3, where an electron from the K shell is ejected from the atom (a 1s photoelectron). An XPS spectrum is the representation of the number of electrons recorded by the detector as a function of the kinetic energy of the photoelectron emitted or their binding energy. The measurement of the binding energy of the electrons and the intensities of the peaks allow to determine the oxidation state of the atoms, their chemical environment and the atomic composition of the surface of the sample, since the binding energy is characteristic for each particular element. XPS allows the identification of all the elements present (except H, He) in concentrations higher than 0.1% and it is a semiquantitative technique. The maximum depth of the solid samples, normal to the surface, from which useful information is obtained, is in the order of 3-10 atomic layers of the analyzed material. The depth of analysis in XPS varies with the kinetic energy of the electrons under consideration. It is determined by a quantity known as the attenuation length of the electrons, which is related to free path of the electrons before suffer an inelastic collision, after which they could not leave the sample. The finite mean free path of electrons is of the order of a few nanometers.[168,169]

Ejected *K* electron
(1s electron)

Vacuum

Fermi
valence band

$L_{2,3}$

L_1

Incident
X-ray
($h\nu$)

K
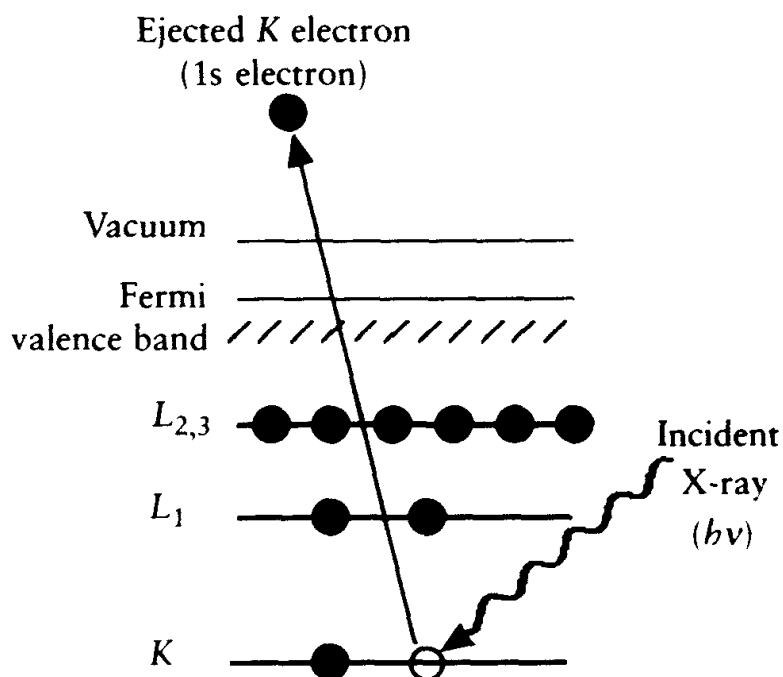
Figure 3.3 Schematic representation of the XPS process. [169]

All the materials were analyzed using an SPECS GmbH with UHV system, energy analyzer PHOIBOS 150 9MCD using a monochromatic X-ray source of Al Kα (1486.74 eV). Each sample was pressed into a small pellet of 10 mm diameter, placed in the sample holder and degassed in the chamber for 24 h to achieve a dynamic vacuum below 10^{-10} mbar before analysis. The spectral data for each sample were analyzed using CASA XPS software. The C1s peak at 284.6 eV was used as an internal standard.

3.3.5. Zeta potential

The determination of the zeta potential and the isoelectric point can be used as a measure of the basicity or acidity of the carbon materials in aqueous solution. Due to the amphoteric nature of carbon, the pH of aqueous suspension of carbons represents the average chemistry of the carbon surface. Bronsted acidic groups of the carbon surface donate their protons to water molecules, and thus the surface becomes negatively charged. Lewis bases adsorb protons from solution, becoming positively charged.[108]

Zeta potential is a measure of the charge on a particle surface in a specific liquid medium. The ionic environment of a particle can be described using the Stern layer model. It is represented by a double layer of ions attached adjacent to the particle surface, and the diffuse layer further away from the particle surface, but enough attracted to the particle to move with the solid grain. Beyond the double layer the ions are in equilibrium with the solution. The boundary between the electric double layer and the ions in equilibrium in the solution is called the slipping plane, as shown in Figure 3.4. Zeta potential is defined as the potential measured in mV at the slipping plane distance from the particle surface.[170]
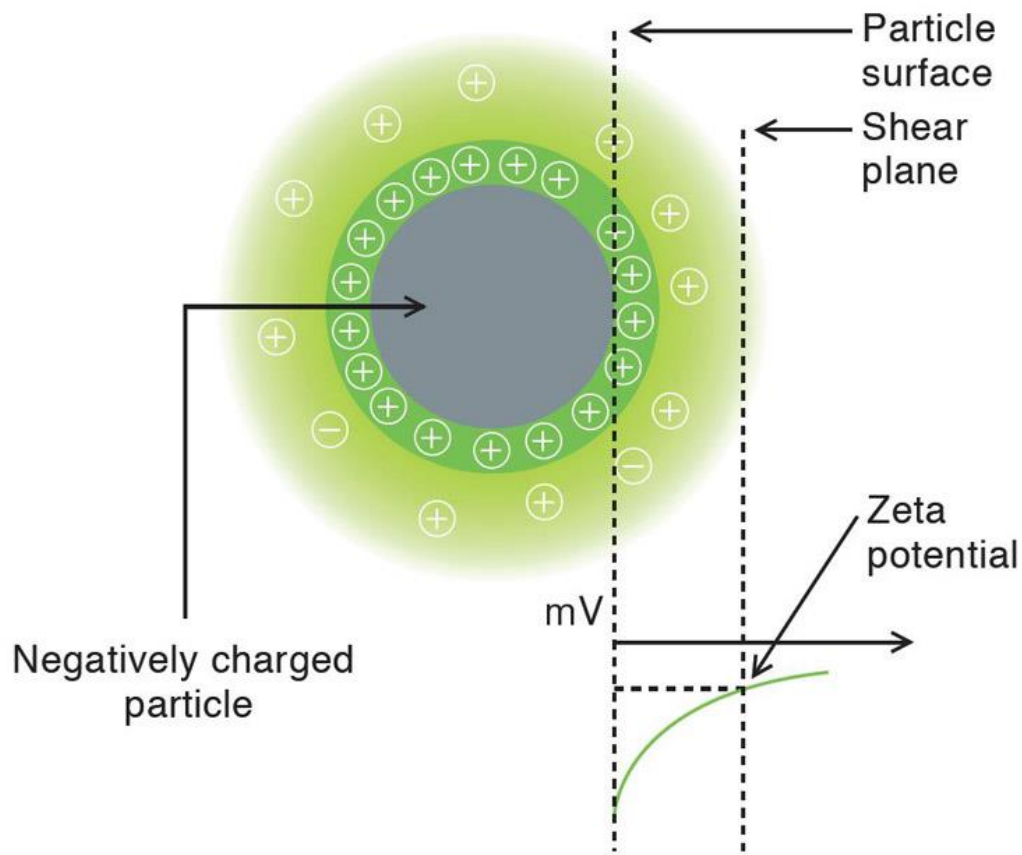
Figure 3.4 Zeta Potential scheme.[170]

The isoelectric point (IEP) is defined as the pH value where the charge at the slipping-plane pH of the Stern layer is zero. It is obtained by means of electrokinetic measurements applying an electric field across the slurry.[171] The particles move toward either the anode or cathode depending on whether the surfaces are positively or negatively charged. The speed of the particle motion (mobility) will be directly proportional to the zeta potential. [170]

To obtain the IEP of graphenic materials, the electrophoretic mobility (μ) of the samples was measured in a Zeta Meter 3.0+ at 25ºC. Each graphene sample (10 mg) was dispersed in 25 mL of water. The pH of the suspension was then adjusted to several pH values between 3 and 11 by adding 0.1M HCl or NaOH solution. Ten zeta potential readings were taken at every pH value, and the average zeta potential at a certain pH value was plotted against the pH value. The pH value where the zeta potential was zero is taken as the IEP.

3.3.6. Transmission electron microscopy (TEM)

The electronic microscopy techniques allow the determination of the size and spatial distribution of the metallic nanoparticles (NPs) and to obtain information about the shape and structure of a wide variety of solids. [163]

TEM uses a high-energy electron beam (100-400 keV) to create an image of the studied material. Electrons that form the electron beam are generated in a gun and accelerated under a differential electric potential to acquire kinetic energy. These electrons are collimated through a series of lenses and condensers to be projected in parallel onto the sample in a high vacuum chamber, interacting with the material through different processes (Figure 3.5). The signal obtained by TEM corresponds to transmitted and undispersed electrons that penetrate the thickness of the sample without interact with it. Subsequently, a series of magnetic lenses deliver the signal to a detector, generating a two-dimensional image of the sample.[167]
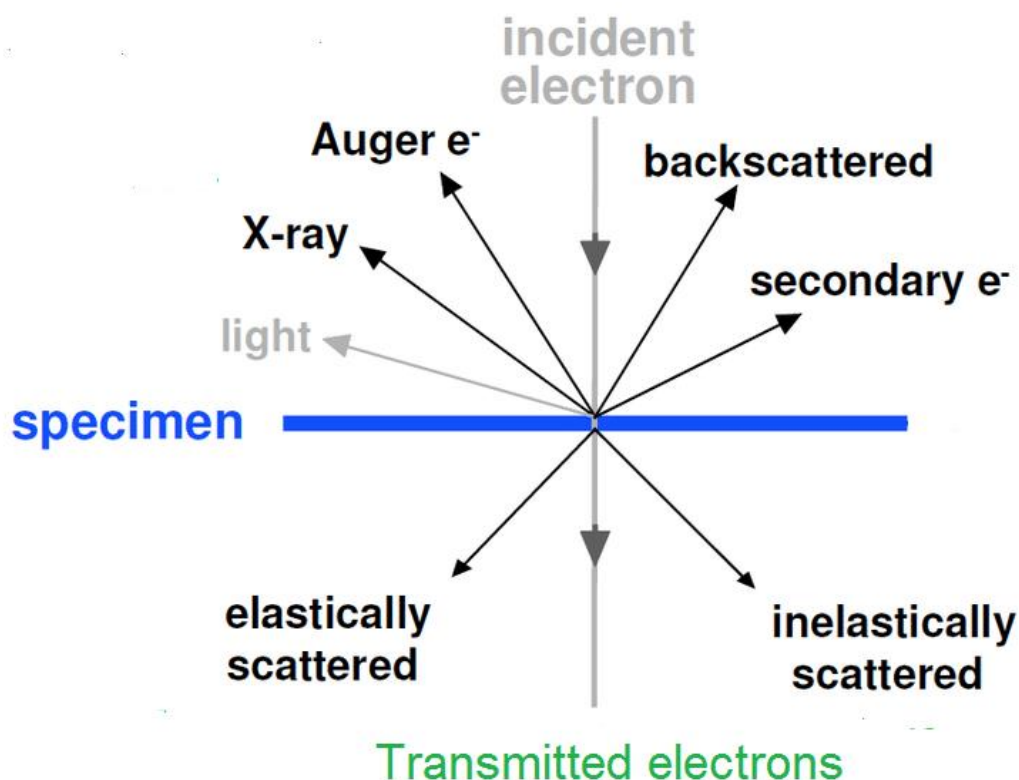
Figure 3.5 Type of signals generated in electron beam-sample interactions.[163]

One of the properties of metallic NPs is their high number of surface atoms that increases with decreasing particle size. These superficial atoms can act as active sites during the catalytic process. In addition, the atoms located in edges and corners are more active than those located in the planes and their number also increases when decreasing the particle size. Therefore, knowing the size of these NPs is essential to understand their activity.[172]

Transmission Electron Microscopy (TEM) micrographs of the supports and of the catalysts were obtained on a JEOL JEM-2100F microscope at 200 kV. The samples were ultrasonically suspended in ethanol before deposition over a carbon-coated copper grid of 200 mesh. The average metal particle sizes in the catalysts were calculated using the following formula [173]:

$$d = \frac{\sum n_i d_i^3}{\sum n_i d_i^2}$$

where n_i is the number of particles with diameter d_i

3.3.7. Raman spectroscopy

In the Raman technique, light is scattered from a sample after being irradiated by a laser. Most of the radiation results from elastic scattering and remains unchanged with respect to the frequency of the incident beam. This is called Rayleigh scattering. An extremely small fraction of the scattered radiation results from inelastic scattering, where the energy from the source is modified by vibrational transitions that occur during the energy transfers of the scattering process. The changes, known as the Raman effect, are observed as shifts to both lower and higher frequencies, a phenomenon demonstrated by C.V. Raman in 1928. The Raman effect is the result of the molecule suffer temporary vibrational transitions, usually from the ground state (v = 0), to the first vibrational energy level (v = 1).[174]

Raman spectrometer is coupled to a confocal microscope allowing to eliminate the reflected or fluorescent light coming from the planes out of focus. Fluorescence can hinder Raman effect because it can easily be six orders of magnitude higher than that of the Raman interaction. The confocal detection setup limits the collection of fluorescence to photons emitted from the focal plane. Besides, as Raman scattering is a very weak effect, the number of Raman photons in a given measurement geometry is limited. Thus, confocal Raman microscope allows to obtain results in reasonable amounts of time.[175]

Figure 3.6 shows a diagram of a typical Raman microscope system consisting of an excitation laser, a microscope, and a spectrometer with CCD detector.
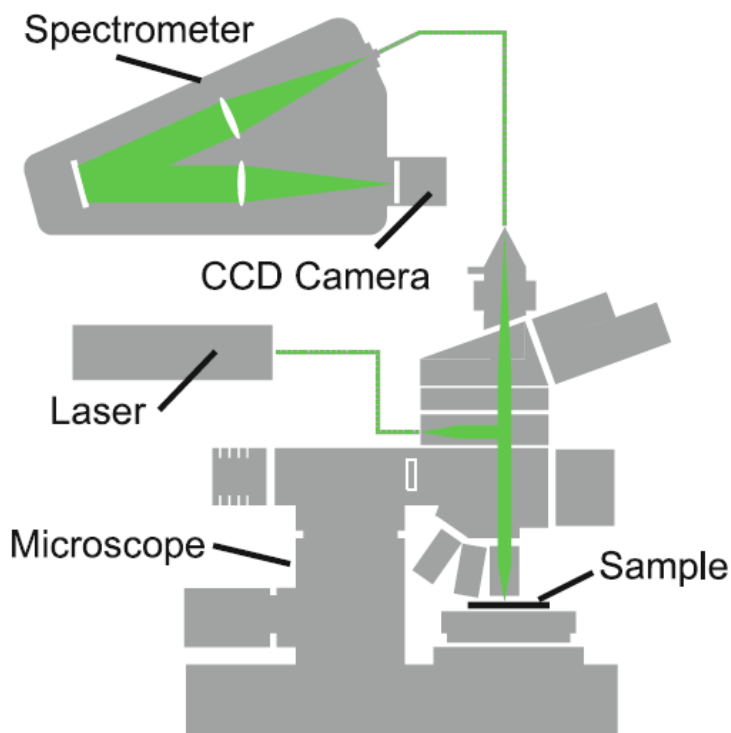
Figure 3.6 Layout of confocal Raman microsope.[175]

For carbon materials, Raman spectroscopy is one of the most used techniques of characterization. It provides information about the structure and the presence of defects, including type and distance between them.

Microscopic confocal Raman spectrometer (Renishaw inVia, 532 nm laser) was employed for the characterization of graphene materials. Over each material there were acquired 25 spectra in different samples points. Average and components fitting was obtained using Wire 4.2 software.

3.3.8. Thermogravimetric analysis (TGA)

Thermoanalytical techniques such as differential thermal analysis (DTA), thermogravimetric analysis (TG) and differential scanning calorimetry (DSC) are widely used for the study of solid materials.[176]

In a thermogravimetric analysis, the mass of a sample placed in a controlled atmosphere as a function of time is continuously recorded as the temperature increases. The representation of mass or percentage of mass as a function of time or temperature is called a thermogram.[168]

Most of the curves show weight loss, caused in general by chemical reactions of degradation or combustion, drying, loss of water of crystallization, physical transitions of evaporation, sublimation or desorption. Rarely a weight gain may be observed.[163] For carbon materials, the oxidation temperature of a sample can be considered a measure of the thermal stability of the structure. A higher oxidation temperature is generally associated with a higher structural purity.[108]

The amount of remaining metal catalyst can be determined from the residual mass of the product, after the complete oxidation of the support; this is a way to obtain the content of metal in carbon supported catalysts.

The equipment used to carry out the TG analysis was composed by a C.I. Electronics Ltd. MK2-MC5 balance, an oven controlled by a temperature controller Eurotherm 2408, and a flow controller Brooks 5850TR. For the analysis, each sample was treated under a heating ramp of 5ºC min^{-1} up to 850ºC under an air flow rate of 60 mL min^{-1}.

The measurement system work using the "zero method". When weight loss occurs, one of the arms is deviated, stopping the pass of the light between the lamp and a photodiode. The mobile part is kept stable by exerting a compensation force from an electromagnetic device.[163] The amplified current of the photodiode is recorded and transformed into information about the loss of mass of the sample thanks to a previous calibration of the system.[168]

3.3.9. Inductively coupled plasma optical emission spectrometry (ICP-OES)

Inductively coupled plasma optical emission spectrometry is a multielemental analysis technique able to determine and quantify the majority of the elements of the table periodic, except for C, N, O, H and noble gases. ICP instrument consists of a solution sample introduction system (a nebulizer and spray chamber), an argon ICP source, a differentially pumped interface, and ion optics for ion beam transmission to the analyser (see Figure 3.7).[163]

The solution sample is introduced into the source as an aerosol, which is completely desolvated. The thermal source in OES is hot enough to induce not only atomization of the sample exposed, but also a significant amount of excitation and ionization of their atoms. Once the atoms or ions are in their excited states, eventually they have to decay back to lower energy states through radiative energy transitions by emitting light. The specific wavelengths at which the optical emissions are measured are used to determine the identities of the elements, and the intensities of the photons emitted are used to determine the concentrations of the elements present in the sample.[174]
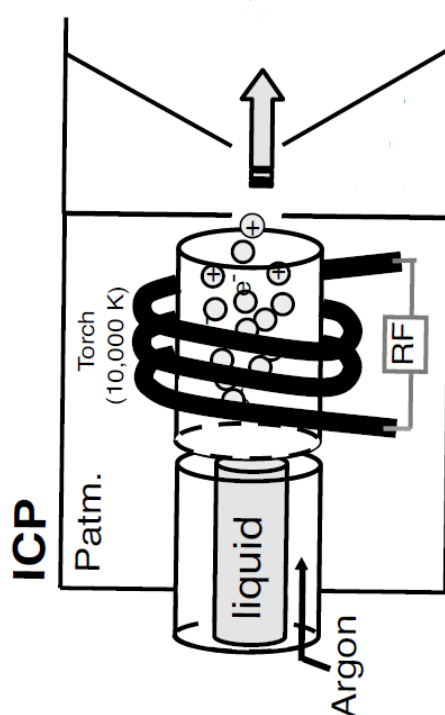
Figure 3.7 Operation process for ICP. [163]

ICP-EOS was used to measure the amount of probable metal leached during the reactions. The experiments were carried out using a Perkin Elmer spectrometer ICP-OES Optima 3300DV.

3.3.10. Temperature-programmed desorption (TPD)

TPD involves subjecting a sample to a temperature program under vacuum while the desorbed gaseous products are analysed by a mass spectrometer. It allows to follow and identify the species desorbed from the surface of a sample.[108]

Temperature programmed desorption experiments with MS analysis of the gases evolved can be used to exclude possible irreversible chemisorption of products on the surface of the catalysts since it allows to discern between chemisorbed and physisorbed products in base to the strength of the adsorption and its thermal stability.
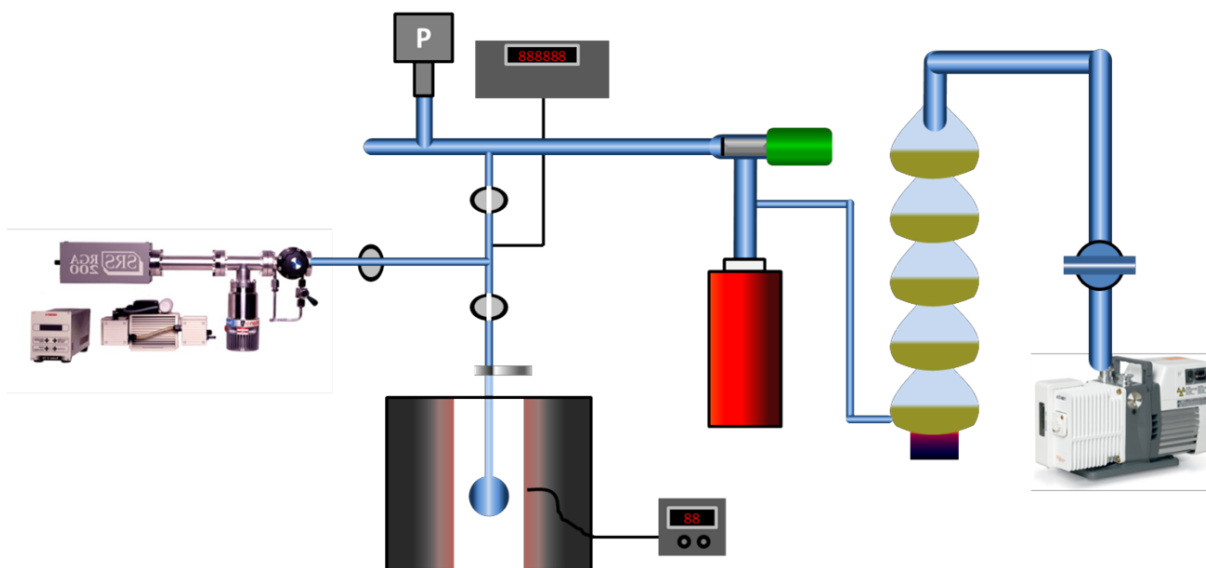
Figure 3.8 Temperature-programmed desorption equipment.

These experiments were carried out under vacuum in a conventional volumetric apparatus connected to a RGA-200 SRS mass spectrometer (Figure 3.8). The samples were placed in a quartz bulb and were evacuated at room temperature to remove physisorbed water. After 30 min, they were heated to 500ºC at a 5ºC min^{-1} rate analysing the evolved gas by the quadrupole mass spectrometer.

3.4. Catalytic tests

This section describes the experimental systems and the analytical methods followed for the reactivity measurement of the catalytic reactions studied: the base free aqueous-phase oxidation of 5-hydroxymethylfurfural to 2,5-Furandicarboxylic acid, the aqueous-phase hydrogenation of furfural to furfuryl alcohol and the selective oxidation of benzyl alcohol to benzaldehyde under base-free conditions.

3.4.1. Oxidation of 5-HMF

3.4.1.1. Experimental system

The oxidation of 5-HMF was carried out using an autoclave (Autoclave Engineers) reactor with 150 mL capacity, equipped with a mechanical stirrer (500 rpm) and furnace system. The autoclave reactor used is shown in Figure 3.9.

Figure 3.9 Autoclave reactor used for 5-HMF oxidation.

By some preliminary studies using the same catalyst it was determined that under this stirring velocity there is not intern mass transfer limitations. After reduction treatment, the catalysts (50 mg of Ru catalysts; 52, 60, and 370 mg of Ag/NrGO, Cu/NrGO and Au/NrGO catalysts respectively) were suspended in 100 mL of water. Then the autoclave was purged three times with synthetic air and the temperature was increased to 100 ºC. Once the reaction conditions were reached, 1 ml of HMF 0.2M in H_2O was dosed into the autoclave and pressure was raised up to 10 bars with air. .

3.4.1.2. Reactivity measurements

Aliquots of the reactor liquids were collected periodically, filtered and the reaction product mixture was analyzed by HPLC (Agilent Technologies 1200 series equipped with a refractive index detector, Hi-Plex H column, flow 0.7 mL/min, mobile phase 5 mM H_2SO_4, temperature 65 ºC). Carbon mass balances in the reaction studies are higher than 94% in all the catalytic determinations. Some of these experiments were repeated twice in order to check reproducibility of these measurements.

The conversion of HMF was calculated as:

$$C(\%) = \frac{HMF_i - HMF_f}{HMF_i} \cdot 100$$

where HMF_i represents the initial HMF concentration and HMF_f the final HMF concentration

The selectivity of each product was calculated as:

$$S_i(\%) = \frac{mol_i}{mol_t} \cdot 100$$

where mol_i represents the mole of the product whose selectivity is being calculated and mol_t represents the total moles of all the products.

Site time yields (STY), mols of FDCA produced per mol of catalyst surface per second, were also calculated. For determine the active surface area exposed by the Ru nanocrystallites we have assumed perfectly spherical metallic shapes. Thus with the direct measured of the diameters of such as metallic particles by TEM it is possible to determine the numbers of exposed active sites.

3.4.2. Hydrogenation of Furfural

3.4.2.1. Experimental system

The hydrogenation of FAL was carried out in a 75 mL Teflon-lined steel autoclave reactor (Parr 4560), equipped with a mechanical stirrer (500 rpm). The autoclave reactor used is shown in Figure 3.10.

Figure 3.10 Autoclave reactor used for Furfural hydrogenation.

By some preliminary studies, using the same catalyst, it was determined that under this stirring velocity there is not intern mass transfer limitations. The reactor was charged with 50 mL of an aqueous solution containing 150 mg of FAL and a determined amount of the reduced catalyst in suspension (25 mg of Ru catalysts; 26, 30, and 185 mg of Ag, Cu, and Au catalysts respectively). The system was flushed three times with high purity He. Subsequently the reactor was pressurised up to 10 bars with H_2. The reaction vessel was kept at 20ºC with a water bath.

3.4.2.2. Reactivity measurements

Aliquots of the reactor liquids were collected periodically, filtered and the reaction product mixture was analysed by gas chromatography, Varian 3350 equipment, provided with a FID detector and a Supelco SPB-5 column (30m length × 0.53mm internal diameter × 0.5μm film thickness). The samples for analysis were prepared by dilution of 350 μL of the reaction products with 650 μL of a 0.02M ethanolic solution of decane as internal standard.

Carbon mass balances in the reaction studies are higher than 95% in all the catalytic determinations. Calibration curves for the observed products were determined by injecting known concentrations of reference commercial products and decane as internal standard. Some of these experiments were repeated twice in order to check reproducibility of these measurements.

The conversion of FAL was calculated as:

$$C(\%) = \frac{FAL_i - FAL_f}{FAL_i} \cdot 100$$

where FAL_i represents the initial FAL concentration and FAL_f the final FAL concentration. At this point it should be indicated that as we have used the same Ru loading in all the catalysts and in the exactly the same amount of sample (25 mg) in the reaction tests, the values of catalytic conversions will be operated as description of catalytic activities.

The selectivity of each product was calculated as:

$$S_i\,(\%) = \frac{mol_i}{mol_t} \cdot 100$$

where mol_i represents the mole of the product whose selectivity is being calculated and mol_t represents the total moles of all the products.

3.4.3. Oxidation of benzyl alcohol

3.4.3.1. Experimental system

The oxidation of Benzyl alcohol was carried out using a Radleys Starfish carousel batch reactor on a 10 ml scale at 90ºC with oxygen bubbled through the reaction solution (5 ml min^{-1} at 1 bar) via 0.5 mm i.d. PTFE tubing while magnetic stirring was maintained at 700 rpm. The batch reactor used is shown in Figure 3.11.
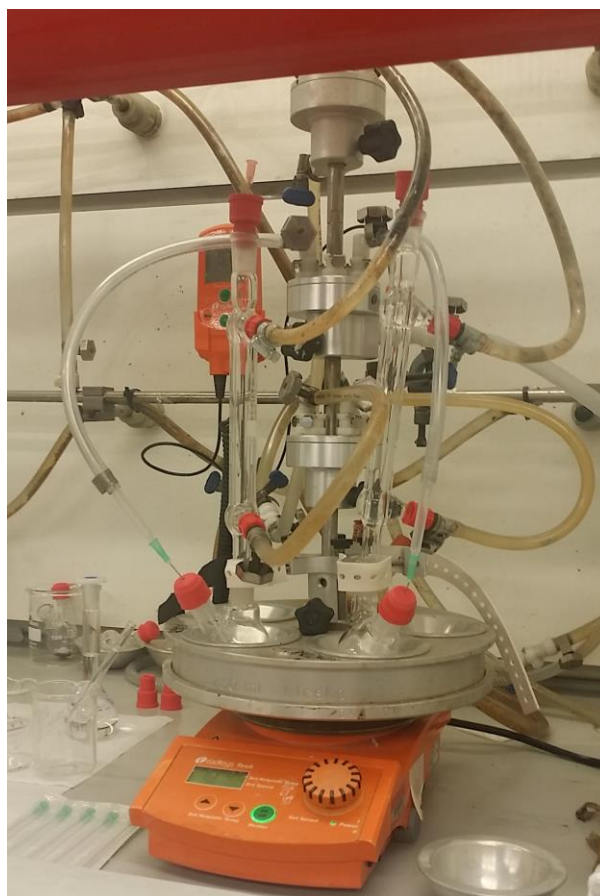
Figure 3.11 Reactor used for benzyl alcohol oxidation.

By some preliminary studies, using the same catalyst, it was determined that under this stirring velocity there is not intern mass transfer limitations. 25 mg of catalyst was added to a reaction mixture of 8.4 mmol benzyl alcohol, 0.1 mL mesitylene as an internal standard, and 10 ml HPLC grade toluene solvent.

3.4.3.2. Reactivity measurement

Aliquots of 0.25 ml of the reactor liquids were collected periodically, filtered and diluted with 1.75 ml of toluene. The reaction product mixture was analysed by gas

chromatography for triplicate on a Varian 3900GC with CP-8400 autosampler (CP-Sil5 CB column, 15 m length× 0.25 mm internal diameter × 0.25 μm film thickness). Carbon mass balances in the reaction studies are higher than 95% in all the catalytic determinations.

The conversion of Benzyl alcohol was calculated as:

$$C(\%) = \frac{BAL_i - BAL_f}{BAL_i} \cdot 100$$

where BAL_i represents the initial benzyl alcohol concentration and BAL_f the final benzyl alcohol concentration. At this point it should be indicated that as we have used the same Ru loading in all the catalysts and in the exactly the same amount of sample (25 mg) in the reaction tests, the values of catalytic conversions will be operated as description of catalytic activities.

The selectivity of each product was calculated as:

$$S_i(\%) = \frac{mol_i}{mol_t} \cdot 100$$

where mol_i represents the mole of the product whose selectivity is being calculated and mol_t represents the total moles of all the products.

3.4.4. Stability of the catalysts

Due to chemical and physical reasons, the activity and selectivity of catalyst will gradually decrease either with the running time or the number of cycles, until it is lower than a certain value which will be considered to be inactive.[164]

Based on the catalytic results, the stability of the best catalyst for each reaction is examined, in particular, their reusability. At least three successive rounds are conducted with the solid recovered by filtration and washed thoroughly with the reaction solvent.

RESULTS AND DISCUSSION

4. RESULTS AND DISCUSSION

In this chapter, the experimental results obtained are explained in detail. The characterization results of supports and metallic catalysts are presented in sections 4.1 and 4.2 respectively. Section 4.3 shows the experimental results for the reactions studied, including reusability tests. In order to comprehend the effect of N-doped surface groups of graphenic materials on Ru NPs and how support properties can affect the catalytic performance of the catalysts, the characterization and experimental results are deeply discussed.

4.1. Characteristics of the supports

4.1.1. Graphenic materials

As it was mentioned in the Experimental chapter, section 3.1.1, the approach used in this thesis for the synthesis of graphenic materials is based on the oxidation of graphite (G) flakes to produce graphite oxide (GO) following a modification of the Brodie's method.[123]. Graphenic materials were obtained subsequently via thermal treatment of GO.

XRD is a powerful tool to evaluate the interlayer changes of graphene based materials. Figure 4.1 shows the XRD patterns of G_{10}, G_{100}, G_{325}, GO_{10}, GO_{100} and GO_{325}. G samples presented the characteristic diffraction peak corresponding to pristine graphite (002) reflection at $2\theta \sim 26°$.[133]

A downshift for (002) reflection peak to 2θ~15° after the oxidation treatment was observed for all the samples of GO. It indicates that a successful oxidization of all Gs was achieved.[118] The distance between layers ($d_{(002)}$) increased from 0.33 nm for G to 0.57 nm for GO samples, it is due to the presence of interlayered species incorporated during the oxidation of graphite.[131]
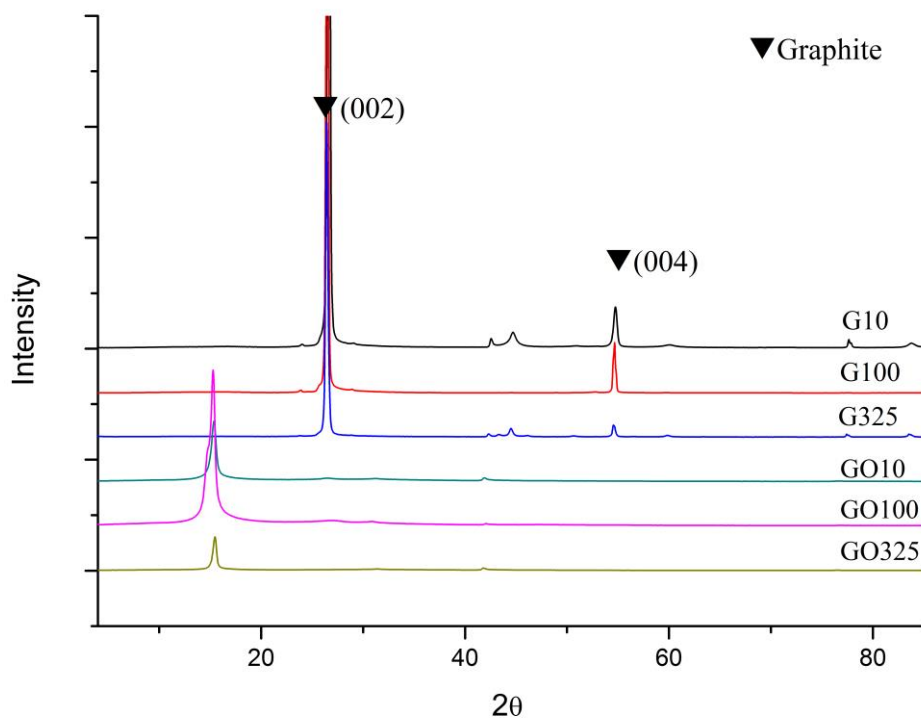

Figure 4.1 XRD patterns of G_m and GO_m

Small heating rates were selected to be evaluated during the exfoliation process of GOs. It is because fast heating rates produce more wrinkled sheets.[131] Thus, small heating rates are fast enough to produce an effective expansion allowing the exfoliation and minimizing the distortion of the graphene sheets. Temperatures below 700ºC were used in the thermal treatments. It is known that oxygen groups decompose at high temperatures reducing the number of reactive sites for N doping[146] and that high annealing temperatures (>700ºC) could break C-N bonds in NrGO leading to a low doping level.[155]

At this point, it should be remarked that the preparation of the supports was carried out several times, in order to obtain a quantity of mass of support enough to prepare the different catalysts. For the obtained solids in each individual synthesis, chemical analysis, determination of the XRD pattern and the study of adsorption isotherms were performed. From these results, the reproducibility of the sample preparation was evidenced, since small deviations in the obtained characterization results were observed for the graphenic aliquots prepared several times under the same experimental conditions.

Application of BET method to N_2 adsorption isotherms (type IV isotherms displayed in the Figure 4.2) gave surface area (S_{BET}) values ranging from 667 to 867 m^2g^{-1} for rGO_{325} samples and from 427 to 492 m^2g^{-1} for $NrGO_{325}$ samples.
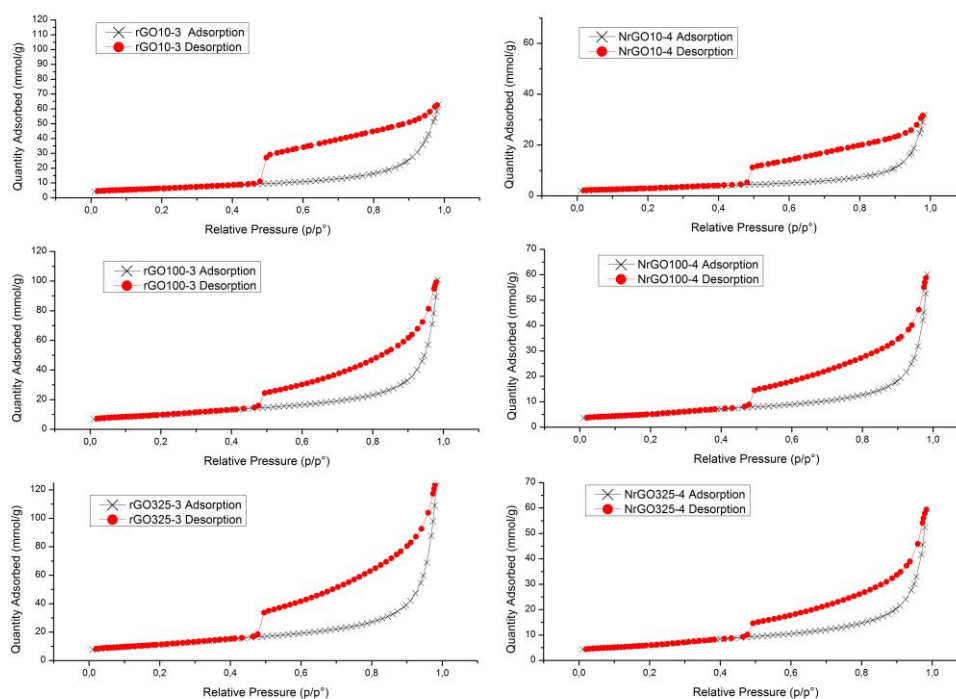
Figure 4.2 N$_2$ adsorption–desorption isotherm for samples rGO$_{325}$-3, NrGO$_{325}$-4, rGO$_{100}$-3, NrGO$_{100}$-4, rGO$_{10}$-3 and NrGO$_{10}$-4

These obtained S$_{BET}$ values are significantly lower than the theoretical value calculated for a single layer of graphene (2630 m^{2}g^{-1}),[118] which indicate some restacking of graphene layers and the formation of a few-layer graphene structures, both for rGO and for NrGO. However, these values are much higher than the values previously reported using thermal exfoliation to produce rGO[149,151] and NrGO[133].

106

Table 4.1 Interlayer distance $d_{(002)}$, estimated number of layers (N_L), S_{BET} and N content (%) for N doped and non doped reduced graphene oxide samples

| GO_m	Ramp	Atmosphere	Sample	$d_{(002)}$ (nm)	N_L*	S_{BET} (m^2g^{-1})	N (%)
GO_{325}	1	Inert	rGO_{325}-1	0.35	13	767	-
	2		rGO_{325}-2	0.35	10	804	-
	3		rGO_{325}-3	0.34	12	867	-
	4		rGO_{325}-4	0.35	17	667	-
	5		rGO_{325}-5	0.36	26	856	-
GO_{100}	3	Inert	rGO_{100}-3	0.35	10	778	-
GO_{10}	3	Inert	rGO_{10}-3	0.34	18	505	-
GO_{325}	1	Ammonia	$NrGO_{325}$-1	0.34	14	428	4.8
	2		$NrGO_{325}$-2	0.35	9	427	4.4
	3		$NrGO_{325}$-3	0.34	14	460	5.0
	4		$NrGO_{325}$-4	0.34	14	492	5.0
	5		$NrGO_{325}$-5	0.34	13	476	4.1
GO_{100}	4	Ammonia	$NrGO_{100}$-4	0.35	10	420	3.8
GO_{10}	4	Ammonia	$NrGO_{10}$-4	0.34	40	236	1.8

* $NL= (L_{002}+d_{002})/d_{002}$

From the results showed in the Table 4.1 it can be seen that the ramp 3 for non-doped graphene (rGO$_{325}$) and the ramp 4 for N-doped graphene (NrGO$_{325}$) lead to reduced materials having an enhanced S$_{BET}$. The ramps used for the exfoliation of GO$_{10}$ and GO$_{100}$ were selected on the basis of these results. Thus, the ramp used for the preparation of rGO$_{10}$ and rGO$_{100}$ was the ramp 3, and for NrGO$_{10}$ and NrGO$_{100}$ was ramp 4. A significant and gradual decrease of the surface area values as the size of starting graphite increases was observed for rGO and NrGO sample series. These findings are coherent with a tendency anteriorly reported for non-doped graphenic materials by Dao et al.[151]: the lower the starting G size, the higher the oxidation degree of the obtained GO, which could lead to a better exfoliation of rGO.

The completion of the exfoliation process for the prepared graphenic materials was investigated by XRD. Figure 4.3 shows the XRD patterns of NrGO$_m$-r and rGO$_m$-r. After thermal treatment, the characteristic diffraction peak at 2θ~15° of GO disappeared and a new main peak appeared at 2θ~26° corresponding to the graphite (002) reflection.[133] It suggests a successful exfoliation of NrGO and rGO. The small and broad peaks at 2θ~26° may indicate that the sample contains some restacking of graphene layers and the formation of a few-layer graphene structures. This behaviour is favoured under ammonia reactive conditions. The intensity of this peak increases when the particle size of the starting material increases, showing a higher number of restacked layers. This tendency is coherent with the values of S$_{BET}$. The average stacking number of graphene layers (N$_L$) in the exfoliated samples was calculated by using the layer-to-layer distance (d$_{(002)}$) and size of the crystallite, which was calculated from the width of the diffraction peak of the (002) reflection, using the Scherrer equation.[135] The N$_L$ calculated show higher values than the ones expected according to S$_{BET}$

obtained, this may be due to the fact that XRD signal is strongly influenced by the thicker particles, although these are minor in the total of the sample, since they are the ones with the highest diffraction signal. X-ray crystalline parameters are shown in Table 4.1.
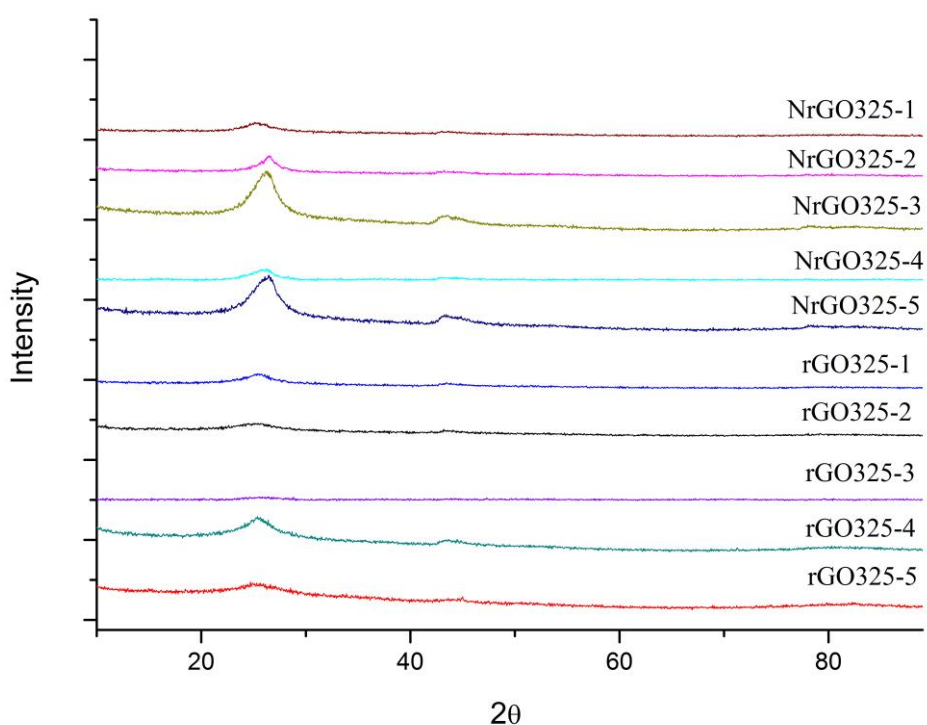
Figure 4.3 XRD patterns of graphenic materials: NrGO$_{325}$-1 NrGO$_{325}$-2, NrGO$_{325}$-3, NrGO$_{325}$-4, NrGO$_{325}$-5, rGO$_{325}$-1, rGO$_{325}$-2, rGO$_{325}$-3, rGO$_{325}$-4,and rGO$_{325}$-5.

The concentration of nitrogen adatoms in the graphenic materials was determined by elemental analysis. As is expected, none content of nitrogen is detected in rGO. As shown in Table 4.1, the N content for NrGO$_{325}$-4 sample was 5.0 wt.%. A gradual decrease of the N content values as the size of starting graphite increases was observed. There are two

explanations for this phenomenon. First, this tendency can be explained in terms of the higher degree of oxidation obtained in GO samples for smaller graphite particle sizes.[151] It is know that certain oxygen functional groups in the GO favour reactions with NH_3 to form C-N bonds, allowing incorporation of N in the structure.[146] Thus, smaller graphite particle size could lead to higher N contents. Besides, the higher degree of exfoliation of small crystals also facilitates the contact of the ammonia with the groups in the sheets leading to a better incorporation of N atoms.

XPS is a powerful technique to identify the chemical states of the surface species. It was used to analyse the different graphenic materials from the characteristic XPS peaks corresponding to C, N and O (Figure 4.4 shows general XPS spectra). These results obtained from the analysis of the C1s, O1s and N1s individual high resolution spectra are shown in Table 4.2.

The assignment of the components of the N1s, O1s and C1s region is not straightforward. The value of binding energy observed for the different functional groups of these elements varies in the literature. It may be due to the specific environments of the atoms and to the redistribution of electrons after ionization of the sample.[107,142,177,178]
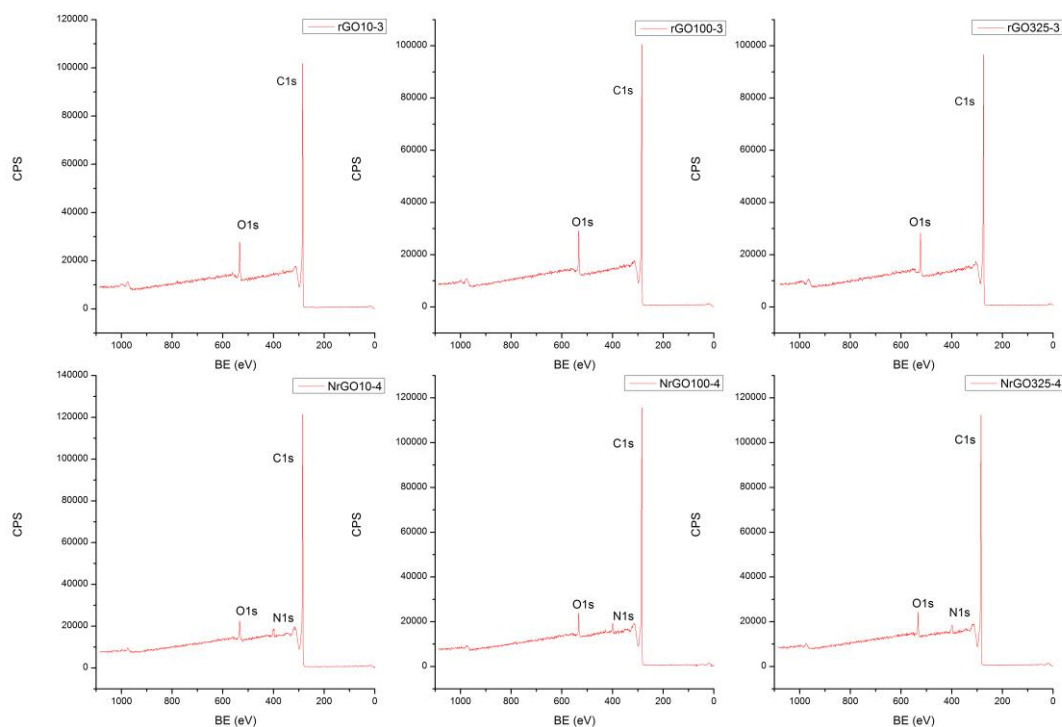
Figure 4.4 Survey XPS spectra for rGO$_{325}$-3, NrGO$_{325}$-4, rGO$_{100}$-3, NrGO$_{100}$-4, rGO$_{10}$-3 and NrGO$_{10}$-4

Nitrogen peak deconvolution for NrGO$_m$-4 samples (Figure 4.5) indicated the presence of four elementary peaks: pyridinic nitrogen (399.5–398.5 eV), pyrrolic nitrogen (400.8–399.8 eV), quaternary nitrogen (403.0–401.0 eV), and NOx groups (404.9–405.6 eV).[133,179–183] XPS analysis indicated that about 3.2-3.7 at.% N was found in the surface of the graphene sheets after ammonia treatment. This difference compared to the bulk N% content obtained by elemental analysis could be attributed to inhomogeneous nitrogen doping, being it lower at the surface analysed by XPS. No nitrogen peak was detected for rGO samples. % of pyridinic N species was slightly higher for samples obtained from smaller sizes and quaternary nitrogen

111

was higher for bigger ones. Of all N species, the pyridinic nitrogen is believed to have the stronger basic character. Accordingly, it is generally assumed that the basicity of carbon catalysts is linked to the amount of pyridinic groups.[137,184]
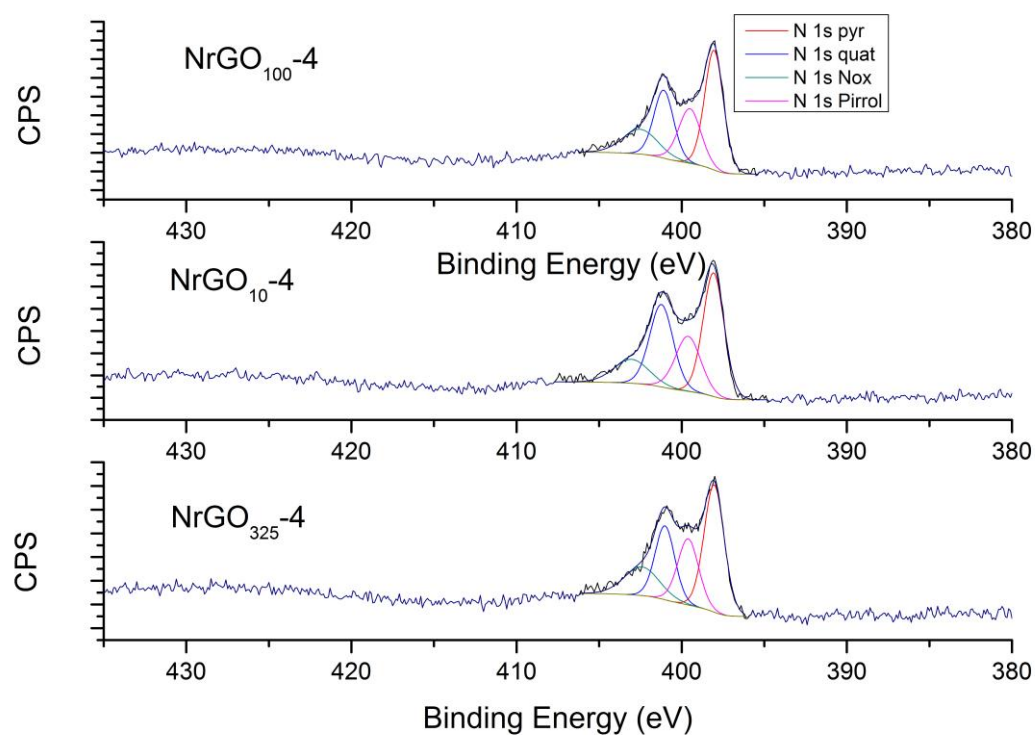
Figure 4.5 XPS spectra of the N 1s region for NrGO$_{100}$-4, NrGO$_{10}$-4, and NrGO$_{325}$-4 samples.

The C1s spectra was solved considering five components which can be assigned to graphitic sp^2 carbon atoms (284.6-285.1 eV), C-O bonds present in alcohol or ether groups (286.3-287.0 eV), C=O functional groups (287.5-288.1 eV), carboxyl or ester groups (289.3-290 eV), and a fifth wide shake-up satellite peak representing π- π* transitions of aromatic rings (291.2-292.1 eV).[181,185]

Concerning O1s (Figures 4.6 and 4.7), the curve was fitted considering four contributions corresponding to: carbonyl groups (531.1-531.8 eV), epoxide and hydroxyl groups (532.3-533.3 eV), carboxylic groups (534.0-534.4 eV) and chemisorbed H_2O or oxygen (535.5-536.1 eV).[178,181,185–187]

The analysis revealed that surface oxygen content varies from 3.6-4.1 at% for N doped samples to 6.8-7.0 at% for non doped samples. The relatively small amount of oxygen in respect to carbon may be attributed to the temperature of the process. It is known that higher temperatures during the thermal treatment produce a decrease of the amount of oxygen functional groups.[131] The oxygen/carbon atomic ratios also confirm this, as can be seen in Table 4.2. The differences in these ratios can be ascribed to an enhancement in oxidation degree from the original GO. For samples from raw graphite with smaller particles sizes the oxidation degree of GO is higher. After the thermal treatment the final content of oxygen is slightly higher for samples from graphite with smaller particle size.
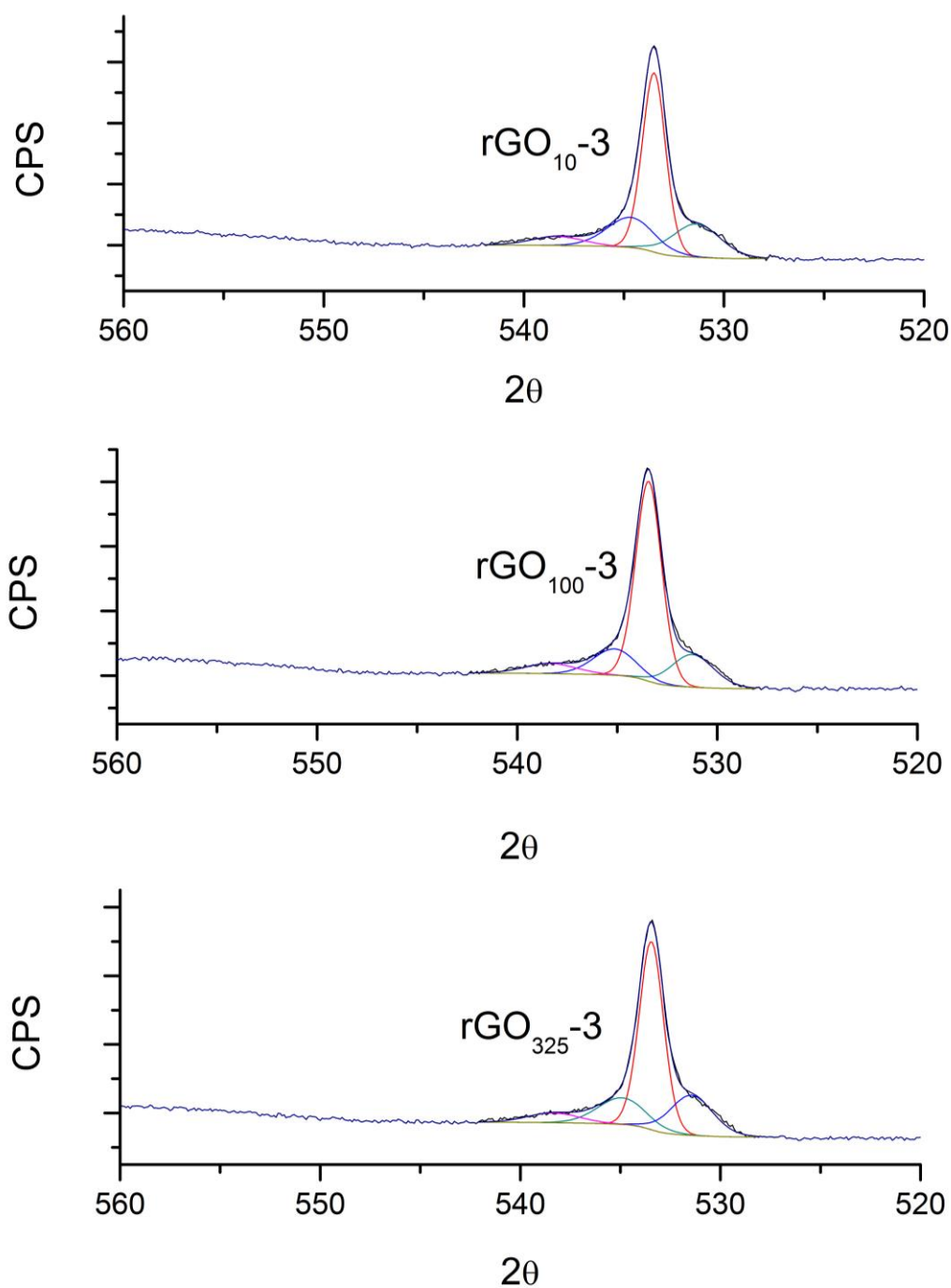
Figure 4.6 XPS spectra of the O 1s region for rGO$_{10}$-3, rGO$_{100}$-3 and rGO$_{325}$-3 samples, being ____C-O, ____C=O, ____COOH, and ____H$_2$O.
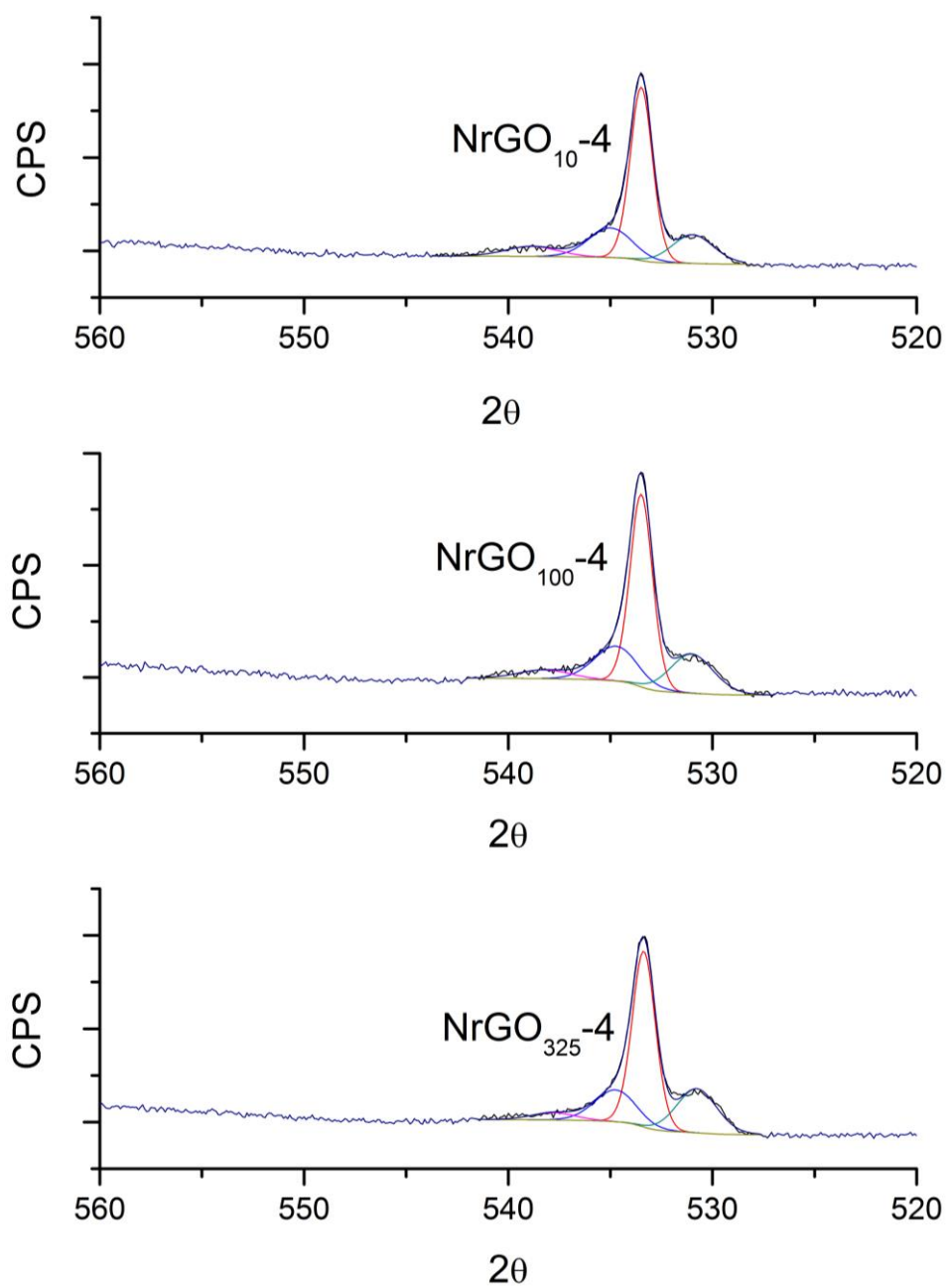
Figure 4.7 XPS spectra of the O 1s region for NrGO$_{10}$-4, NrGO$_{100}$-4 and NrGO$_{325}$-4 samples, being ____C-O, ____C=O, ____COOH, and ____H$_2$O.

Table 4.2 XPS deconvolution results and RAMAN Id/Ig ratio for rGO$_m$-3 and NrGO$_m$-4 samples

Sample	O (at%)	N(at%)	O 1s				N1s				I_D/I_G
			C-O	C=O	COOH	H_2O	Pyr	Pyrr	Quat	Nox	
rGO$_{325}$-3	7.0	-	57.0	21.1	15.7	6.2	-	-	-	-	0.63
rGO$_{100}$-3	7.0	-	63.1	17.0	13.7	6.3	-	-	-	-	0.39
rGO$_{10}$-3	6.8	-	54.6	20.7	18.7	6.0	-	-	-	-	0.53
NrGO$_{325}$-4	4.1	3.4	54.7	23.5	17.6	4.2	38.5	20.5	28.5	12.5	0.75
NrGO$_{100}$-4	3.6	3.7	54.2	21.2	18.9	5.7	39.5	21.7	23.6	15.3	0.63
NrGO$_{10}$-4	3.6	3.2	56.2	17.4	18.7	7.6	40.0	21.7	22.7	15.7	0.58

As the surface charge of carbonaceous materials is governed by the nature of the surface groups and the pH; PZ can be used to estimate the graphenic materials surface chemistry.[108] An increase in the IEP values was found for NrGO samples (Figure 4.8) showing An¡N IEP of 8.5-8.7 against 7.2-7.4 of rGO samples. These results indicate that NrGO surfaces present a higher basic character than rGO. Nitrogen atoms incorporate an additional electron into the graphenic structure in comparison with carbon atoms; this fact favours delocalization of p electrons in N doped samples, leading to changes in the acid-base character of the surface. Thus, this excess of electrons produces an increase in the electronic density, which could explain the higher IEP values obtained for NrGO samples. Due to the fact that electron-donor properties are related to basicity, the stronger the electron donating of the surface, the higher the basic strenght.[182]
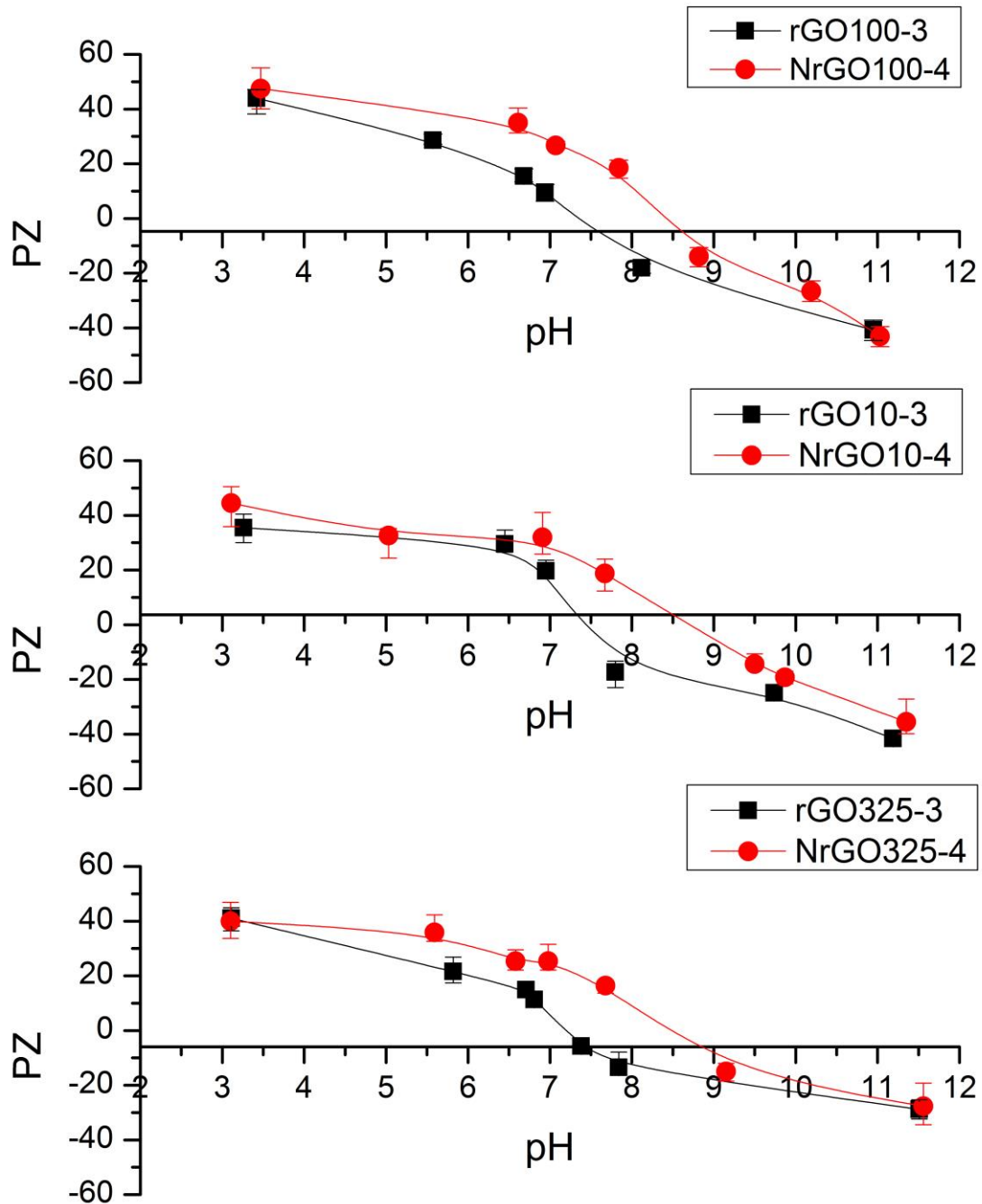
Figure 4.8 IEP for rGO$_m$-3 and NrGO$_m$-4 samples

Raman spectroscopy is a very useful tool to evaluate the degree of disorder in the structure of graphene.[118] Figure 4.9 shows Raman spectra of rGOm-3 and NrGOm-4 samples. As Raman spectra at discrete spots cannot provide an overall picture in case of non uniform defects distributions in the sample, spectral mapping were used to acquire 25 points over a 50×50 μm^2 area. Two main peaks corresponding to vibrations with E2g symmetry in the graphitic lattice (G band) at 1580 cm^{-1} and to graphite edges or structural defects (D bands) at 1345 cm^{-1} were observed. Another two featured peaks have been reported in previous studies. A band D′ peak appears at 1625 cm^{-1} as a shoulder of the G band. It arises from alterations in the tension of sp^2 carbon atoms in the lattice caused by the arrangement of the electronic cloud.[185] A second peak assigned as 2D (historically called G') is always present at 2700 cm^{-1} in the spectra of graphenic materials.[155]

The intensity ratio of the D and G bands (I_D/I_G) can be used as a quantitative indicator of the amount of disorder or edges within the structure of the samples. I_D/I_G ratios were calculated (Table 4.2). As can be seen, the ratio increases with N content; it is due to a disruption of the symmetry of the lattice produced by the incorporation of heteroatoms into the graphitic structure. This effect has been described previously by Chen et al.[188] They claimed that the introduction of N into the carbon lattice could produce distortions, transforming the graphitic region into sp^3 domain. From the Raman spectra can be observed that an increment in the N content leads to a shift of the D band to lower frequencies.

For a bulk graphite sample, the 2D band consists in two contributions. For single layer graphene, the 2D band appears as a single sharp peak at the lower frequency (around 2690 cm^{-1}). As number of layers increase, the 2D band changes its shape, width and position, and the G peak position shifts to lower frequencies.[118] A systematic study on in–plane crystallite size was carried out in 1970 by Tuinstra and Koenig.[189] They found that the ratio of the D and G band intensities (I_D/I_G) is inversely proportional to the in-plane crystallite sizes L_a. The crystallite sizes (L_a) can be calculated from $L_a(nm)= (2.4 \times 10^{-10}) \lambda^4 (I_D/I_G)^{-1}$ (being λ the Raman excitation wavelength).[190] L_a were 25.6-33.1 nm for NrGO samples and 30.5-49.3 nm for rGO samples. It can be concluded that the crystallite size decreases with the presence of defects and therefore the doping level. It is consistent with the bibliography[155] which point out that, L_a being the average interdefect distance, the introduction of nitrogen atoms accompanied by defects implies a smaller L_a.

Some morphological evidences of differences between rGO and NrGO were determined by TEM (Figure 4.10). TEM images of the samples of rGO exhibited the presence of winkled structure of graphene. The introduction of nitrogen in the graphitic structure did not produce noticeable difference on the morphology of the graphene sheets. HRTEM characterization further showed that rGO325-3 and NrGO325-4 samples consist of 5–12 graphene layers.
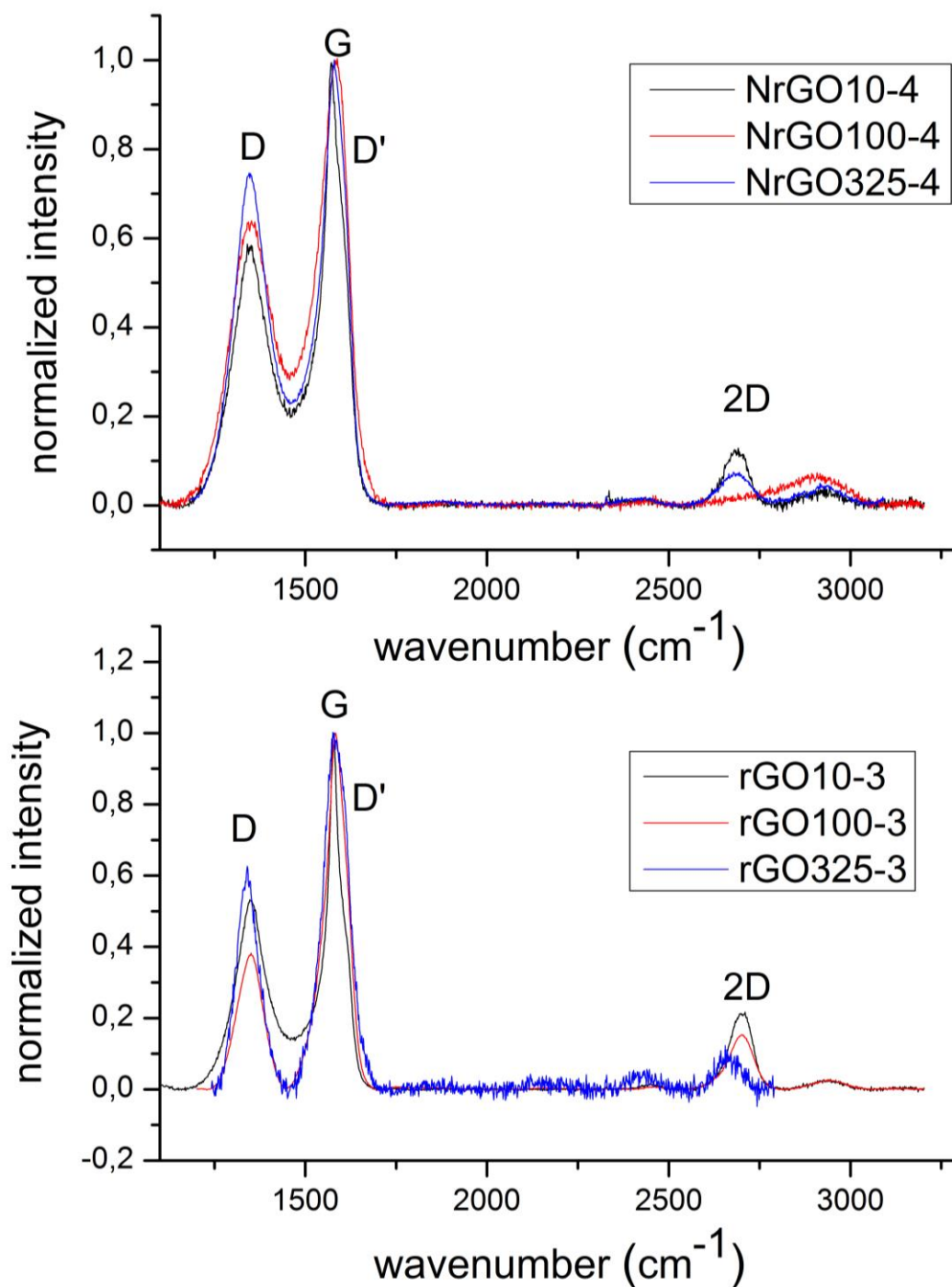
Figure 4.9 RAMAN spectra for rGO$_m$-3 and NrGO$_m$-4 samples.
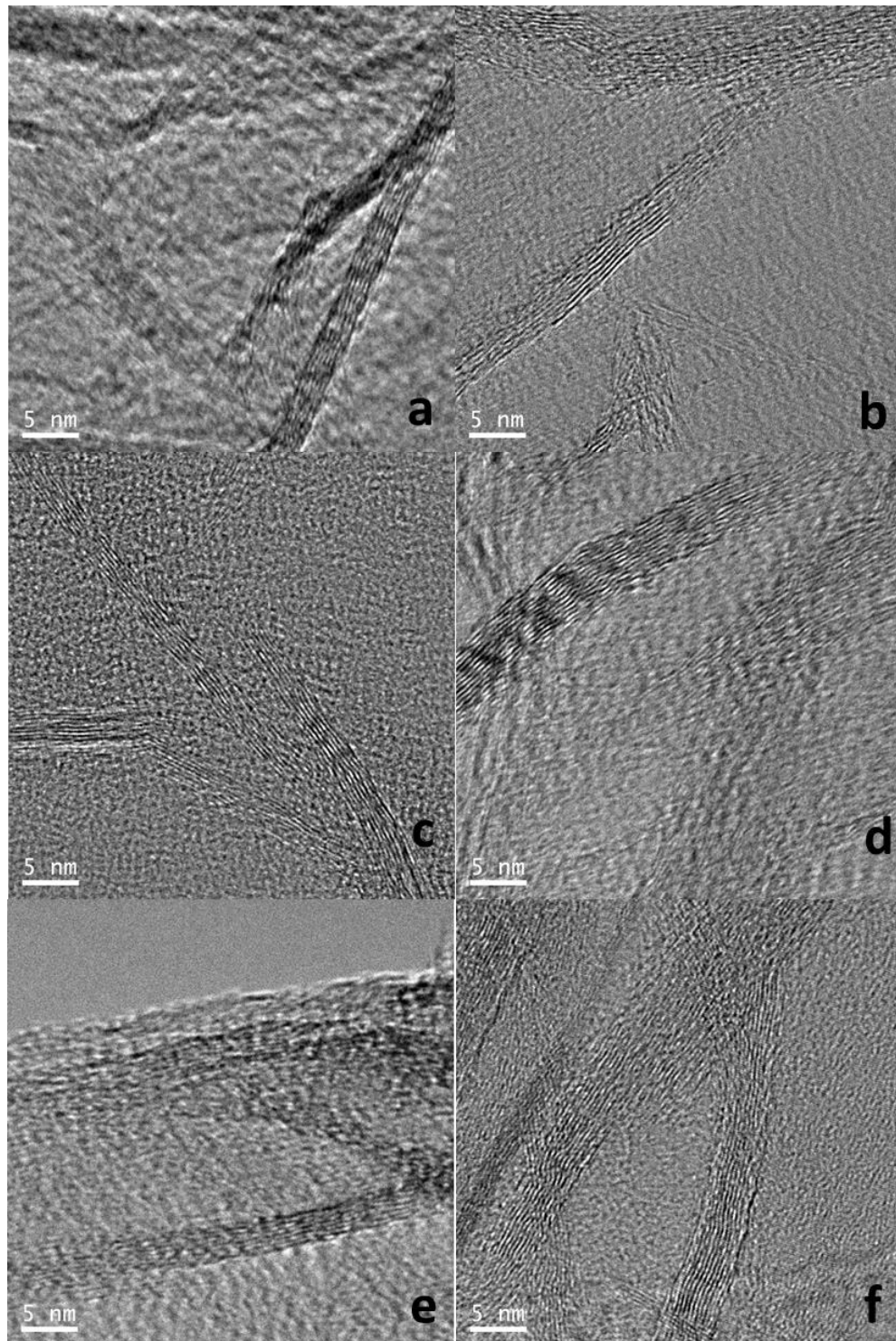
Figure 4.10 TEM micrograph for (a) rGO$_{325}$-3, (b) NrGO$_{325}$-4, (c) rGO$_{100}$-3, (d) NrGO$_{100}$-4, (e) rGO$_{10}$-3 and (f) NrGO$_{10}$-4.

The thermal reactivity under air of the prepared materials was investigated by TGA (Figure 4.11). Differential thermogravimetric profiles for rGO_m-3 samples show pronounced peaks near 598-642ºC that could be attributed to a weight loss due to the oxidation of a well-organized carbon structure. In comparison, for $NrGO_m$-4 samples this peak moved toward higher temperatures, showing oxidation temperatures between 663-671 ºC. These findings are in concordance with previously reported trends[145] showing that the thermal stability in air increases for nitrogen doped graphenic materials and it could be attributed to the extent of the oxidation is larger due to higher surface areas of rGO_m-3 exposing more edge-active positions to oxygen attack.
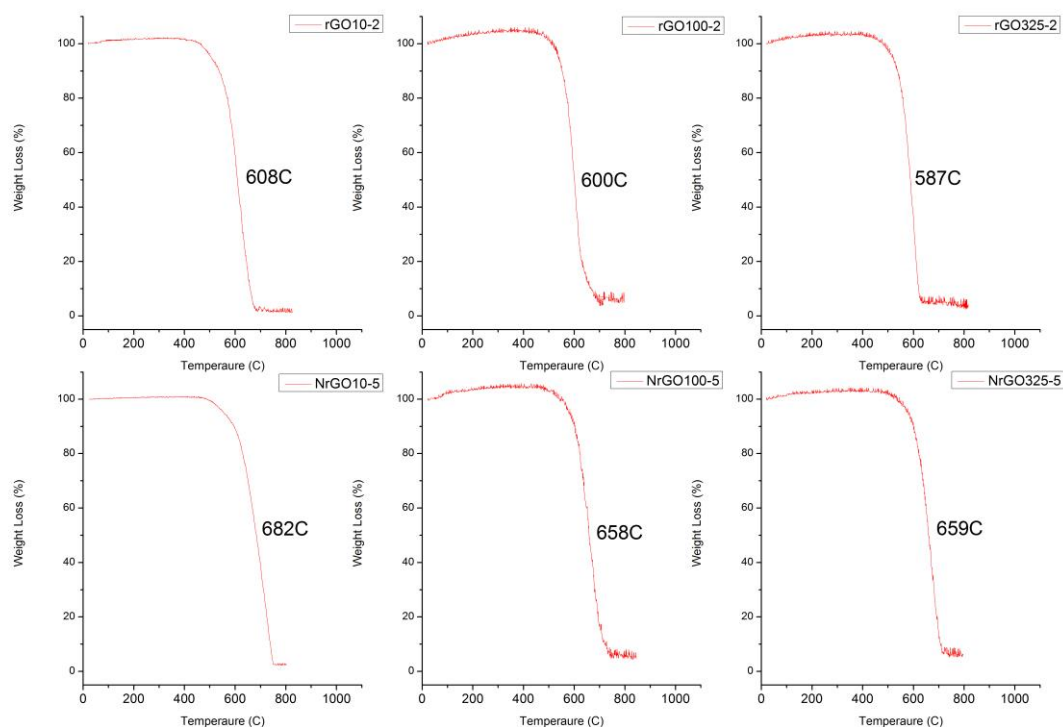
Figure 4.11 TG analysis under air for rGO_m-3 and $NrGO_m$-4 samples.

Figure 4.12 summarizes the results obtained in this section. It becomes clear that materials obtained from G_{325} mesh allow the synthesis of graphenic materials with enhanced properties.
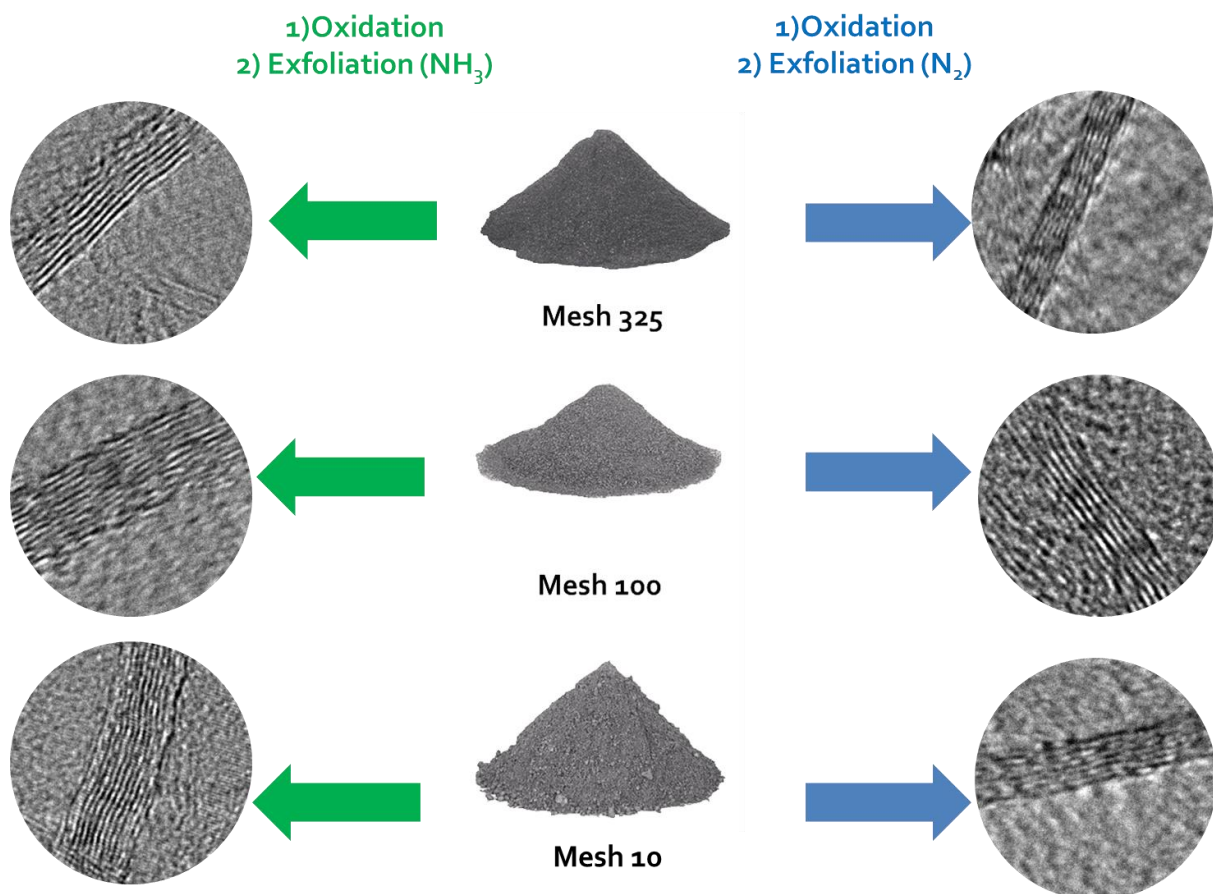
Figure 4.12 Scheme of the different graphenic material prepared using ramp 3 for rGO_m and ramp 4 for $NrGO_m$

4.1.2. Commercial materials

As earlier pointed out in the section 3.1.2, apart from the lab prepared graphenic materials five commercial supports were also employed. These are: SiO_2, TiO_2, Al_2O_3, activated carbon, and high surface area graphite.

The activated carbon (denoted as AC, S_{BET} = 1190 m^2g^{-1}, 313 m^2g^{-1} external surface area) was provided by Oleicola el Tejar, Córdoba Spain. The detailed purification and data of the characterization for this sample can be found in Gallegos-Suarez, E.'s Doctoral Thesis.[191]

The high surface area graphite material (HSAG$_{400}$, S_{BET} = 396 m^2g^{-1}) was supplied by TIMCAL. The detailed data of the characterization for this sample can be found in Esteban-Arranz, A.'s Doctoral Thesis.[192]

SiO_2 (S_{BET} = 465 m^2g^{-1}) was obtained from Fluka, P25 TiO_2 (S_{BET} = 50 m^2g^{-1}) and Al_2O_3 (S_{BET} = 187 m^2g^{-1}) from Degussa.

Figure 4.13 shows the XRD patterns of TiO_2, SiO_2 and Al_2O_3. The analysis of the commercial SiO_2 showed a wide peak at 22° associated to the typical diffraction of the amorphous SiO_2. The Al_2O_3 has a low degree of crystallinity, the wide peak at 67° is characteristic of γ-alumina.[193] Finally, the diffractogram of the P25 TiO_2 contains a mixture of anatase and rutile phases, showing a bicrystalline structure with two clear peaks at 25º and 27° corresponding to anatase (101) and rutile (110), respectively.[194]
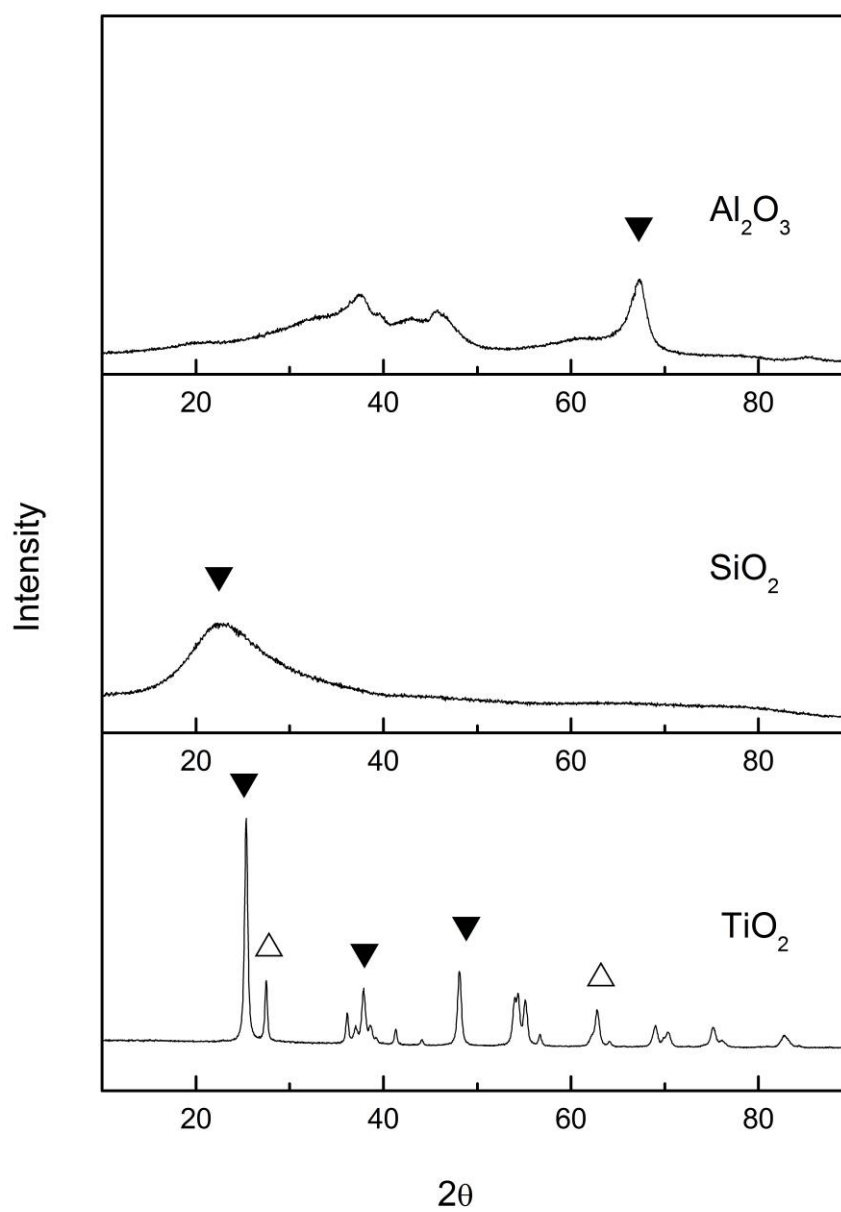
Figure 4.13 XRD patterns of Al$_2$O$_3$, SiO$_2$, and TiO$_2$ (▼ anatase and △ rutile phases).

4.2. Characteristics of the supported catalysts

The characterization results for the graphenic supports showed in the section 4.1.1, suggest that the starting graphite particle size and thermal conditions applied during the exfoliation treatment of GO remarkably affect the final surface properties of the prepared materials. From the results showed in the Table 4.1 it can be seen that the ramp 3 for non-doped graphene prepared from G_{325} (rGO_{325}-3) and the ramp 4 for N-doped graphene prepared from G_{325} ($NrGO_{325}$-4) lead to reduced materials having an enhanced S_{BET}. Surface areas of 867 m^2g^{-1} for rGO_{325}-3 and 492 m^2g^{-1} for $NrGO_{325}$-4 were achieved.

Due to their enhanced properties these optimized these samples, can be considered as promising catalytic materials to be used as metallic nanoparticles supports. It is well know that high surface area supports favor deposition of the precursor leading to well dispersed nanoparticles. Thus, rGO_{325}-3 and $NrGO_{325}$-4 were used as supports of Ru, Cu, Ag, and Au NPs.

For comparative purposes different commercial materials (SiO_2, TiO_2, Al_2O_3, activated carbon and high surface area graphite) were also evaluated as support of Ru NPs.

The effect of three different metal precursors used ($RuCl_3$, $RuNO(NO_3)_3$ and $Ru_3(CO)_{12}$) in the preparation of the Ru nanocrystallites has been assessed. Catalysts prepared by wetness impregnation of $Ru_3(CO)_{12}$ were denoted with "CO" as described elsewhere.[195] Ru catalyst prepared by incipient wetness method using $RuCl_3$ and $Ru(NO)(NO_3)_3$ were labelled as "Cl" and "NN" as precursor.

For the sake of better understanding, in the following sections supports rGO_{325}-3 and $NrGO_{325}$-4 will be denoted as rGO and NrGO, respectively

The loading of metal in carbon supported catalysts was estimated by TGA. Thermogravimetric method consisted in weighing the residues of RuO_2, CuO, Ag_2O and Au generated after burning away the graphenic support at 850ºC in air.[196,197]

Also it was checked that bare supports (rGO and NrGO) produce null amount of residue. The same can be said for the HSAG support material. Contrarily in the case of the commercial AC, in spite of its purification treatment, a small residue weight was determined (0.24 wt%), this amount being subtracted for determining the quantitative loading of incorporated Ru. Considering the similarities of the nominal amount of Ru incorporated and the experimental determinations, we can point out that Ru is not volatilized under these carbon support burning conditions. The chemical compositions of the catalyst are presented in Table 4.3.

Table 4.3 Characteristics of the metallic particles after reducing samples under hydrogen flow at 350ºC for 2 h.

Catalyst	$d_{TEM}{}^a$ (nm)	$d_{TEM}{}^b$ (nm)	metal (wt%)
Ru(Cl)/rGO	1.5	-	3.9
Ru(Cl)/NrGO	1.8		4.4
Ru(NN)/rGO	1.4	1.3	4.0
Ru(NN)/NrGO	1.7	-	4.0
Ru(CO)/rGO	1.4	1.3	4.3
Ru(CO)/NrGO	1.8	-	3.9
Ru(CO)/AC	2.4	-	4.1
Ru(CO)/HSAG	2.3	1.8	4.1
Ru(CO)/Al$_2$O$_3$	1.2	-	4.0^c
Ru(CO)/SiO$_2$	2.7	-	4.0^c
Ru(CO)/TiO$_2$	1.3	-	4.0^c
Au/rGO	5.5	-	1.2
Au/NrGO	8.1	-	1.4
Cu/rGO	4.8	-	2.6
Cu/NrGO	5.9	-	1.8
Ag/rGO	73	-	4.0
Ag/NrGO	40	-	4.3

^{a} Sample reduced at 350ºC ^{b}Sample reduced at 300ºC ^{c}Nominal content

The particle sizes of the Ru NPs in the reduced catalysts were determined by TEM. Figures 4.14 and 4.15 show representative TEM images of the catalysts and their histograms with particle size distribution.

The average diameters of the Ru nanoparticles for the supported catalysts are summarized in Table 4.3, which shows the particle sizes for these Ru crystallites are in the range from 1.2 to 2.7 nm. From Table 4.3, it can be seen that the particle size of Ru nanoparticles strongly depends on the support and precursor used, as well as on the temperature of reduction used.

For Ru(NN)/rGO, Ru(CO)/rGO, and Ru(CO)/HSAG samples, two temperatures of reduction were applied (300ºC and 350ºC), with the TEM measurements for these catalysts indicating that the size of Ru nanoparticles were affected depending on the applied temperature. Lower temperatures can lead to less sintering of the Ru atoms, leading to smaller metallic particle sizes than the catalysts reduced at 350ºC.

When a graphene support (rGO or NrGO) is considered the ruthenium particle size change with the metal precursor in the order: Ru(Cl) > Ru(NN)~Ru(CO).
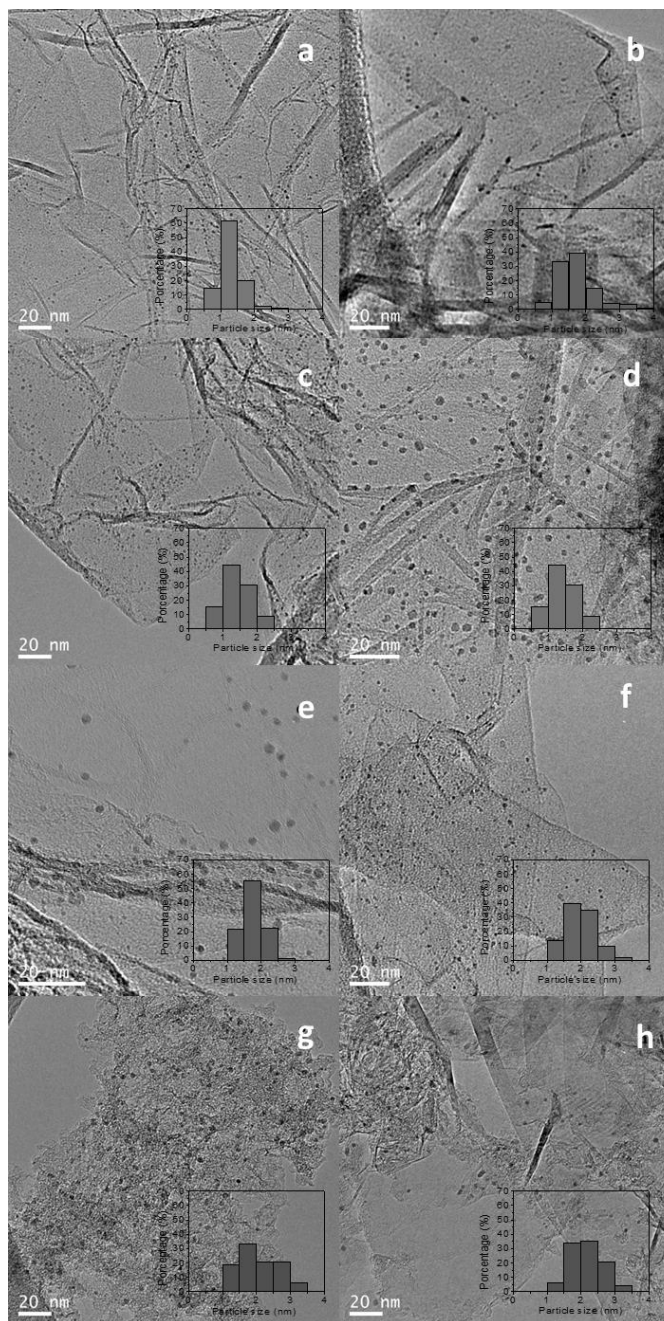
Figure 4.14 TEM images and particle size distribution of the catalysts: a) Ru(Cl)/rGO, b) Ru(Cl)/NrGO, c) Ru(NN)/rGO, d) Ru(NN)/NrGO, e) Ru(CO)/rGO, f) Ru(CO)/NrGO, g) Ru(CO)/AC and h) Ru(CO)/HSAG after H$_2$ reduction at 350ºC .
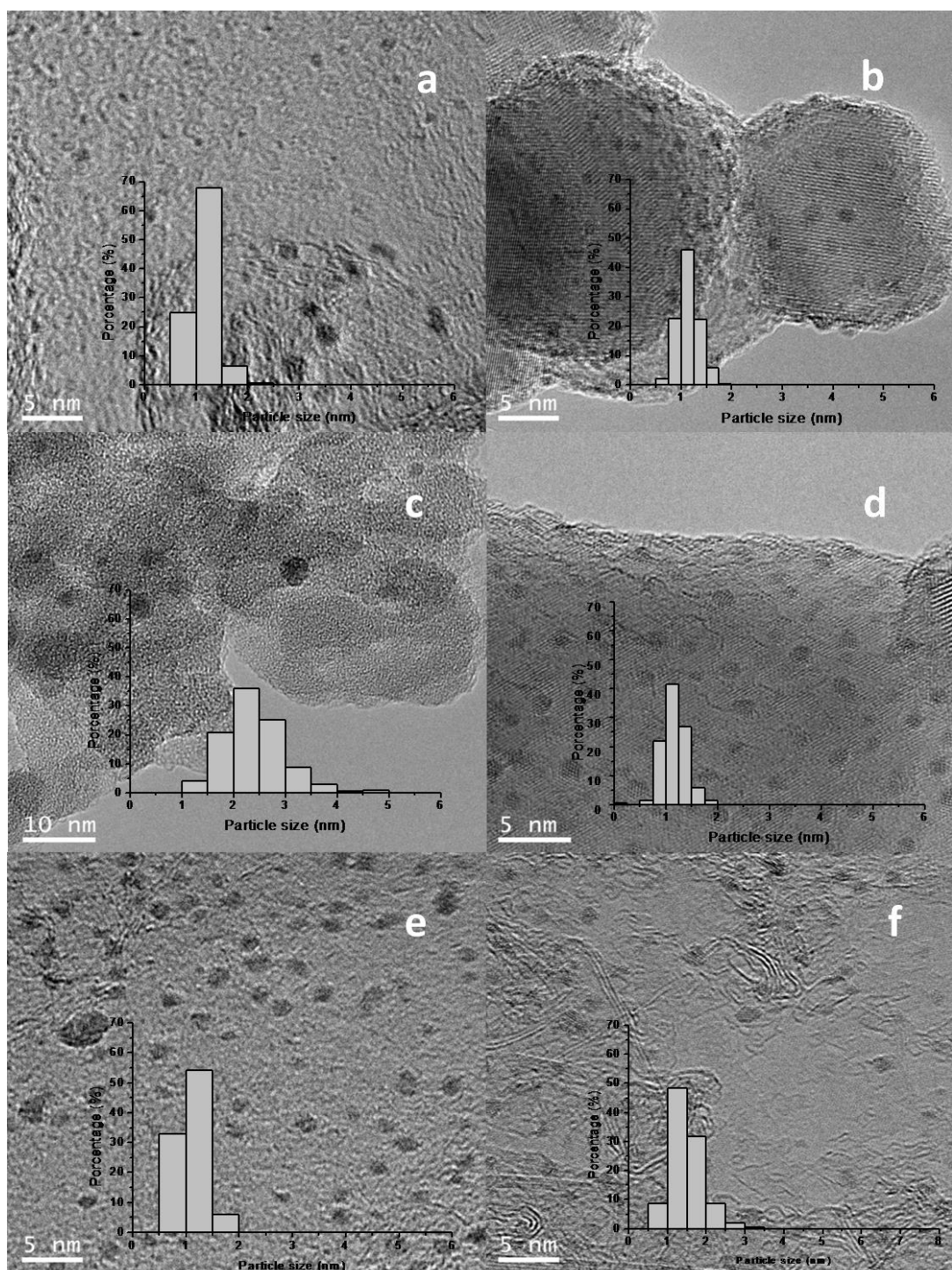
Figure 4.15 TEM images and particle size distribution of the catalyst: (a) Ru(CO)/rGO*, (b) Ru(CO)/ TiO$_2$, (c) Ru(CO)/SiO$_2$, (d) Ru(CO)/Al$_2$O$_3$, (e) Ru(NN)/rGO*, (f) Ru(CO)/ HSAG* after reduction at 300°C(*) or 350°C.

Comparison of Ru catalysts supported on the different materials, prepared from the $Ru_3(CO)_{12}$ precursor, reveals that smaller particle sizes were obtained on rGO support, which could be rationalized as a consequence of the lower specific surface area of HSAG (396 m^2g^{-1}), SiO_2 (465 m^2g^{-1}), NrGO (492 m^2g^{-1}), and AC (313 m^2g^{-1} external surface area) compared to rGO (867 m^2g^{-1}). Thus the higher surface area of rGO promotes the narrow and uniform distribution of the metallic precursor, leading to the particle size observed. In the case of TiO_2 and Al_2O_3 in spite of their relatively low surface areas, some chemical interactions between the Ru carbonyl precursor and the support surface can take place, directing the generation of smaller Ru nanoparticles after reduction. Furthermore, Ru(CO)/HSAG, Ru(CO)/SiO_2 and Ru(CO)/AC catalysts exhibit the highest average particle size and also the broadest range of crystal size distributions. As shown in Figure 4.12 Ru nanoparticles were dispersed uniformly on graphene surfaces without detecting aggregation formation, so the interactions of graphene surfaces with the Ru crystallites seem to be maximized.

The particle sizes of Cu, Au and Ag NPs were also determined by TEM. Figures 4.16 and 4.17 show representative images of the catalysts and their histograms with particle size distribution. The average diameters of the Cu, Au and Ag nanoparticles supported on rGO and NrGO are summarized in Table 4.3. The particle sizes for the Cu/rGO and Cu/NrGO crystallites are 4.8 and 5.9 nm, for the Au/rGO and Au/NrGO crystallites are 5.5 and 8.1 nm, and for the Ag/rGO and Ag/NrGO crystallites are 73 and 40 nm, respectively. As can be seen Cu and Au NPs supported on rGO present smaller particle sizes compared to their counterparts supported on NrGO. This can be explained, in the same way than Ru NPs supported over graphenic materials, as a consequence of the higher specific surface area of rGO ($867 \ m^2 g^{-1}$) compared to NrGO ($492 \ m^2 g^{-1}$).

For Ag/rGO sample, a wide range of NPs sizes was observed. Furthermore, even although the mean particle sizes was 73 nm, the sample contained a significant population of NPs between 0-50 nm and 120-250 nm, nearly a bimodal distribution, showing that incipient wetness impregnation is not an efficient method to disperse the Ag NPs on rGO using $AgNO_3$ as precursor. Ag/NrGO sample showed a broad range of NPs sizes, however the mean particle sizes was 40 nm.

According to the signal intensity of the XRD patterns (See Figure 4.20 below) for Ag catalysts, applying the Scherrer's equation, Ag/rGO showed smaller particle sizes than Ag/NrGO (36 and 43 nm respectively). Therefore, it could be suggested that bigger crystals in the TEM images of the sample Ag/rGO could be hiding a significant population of smaller NPs.
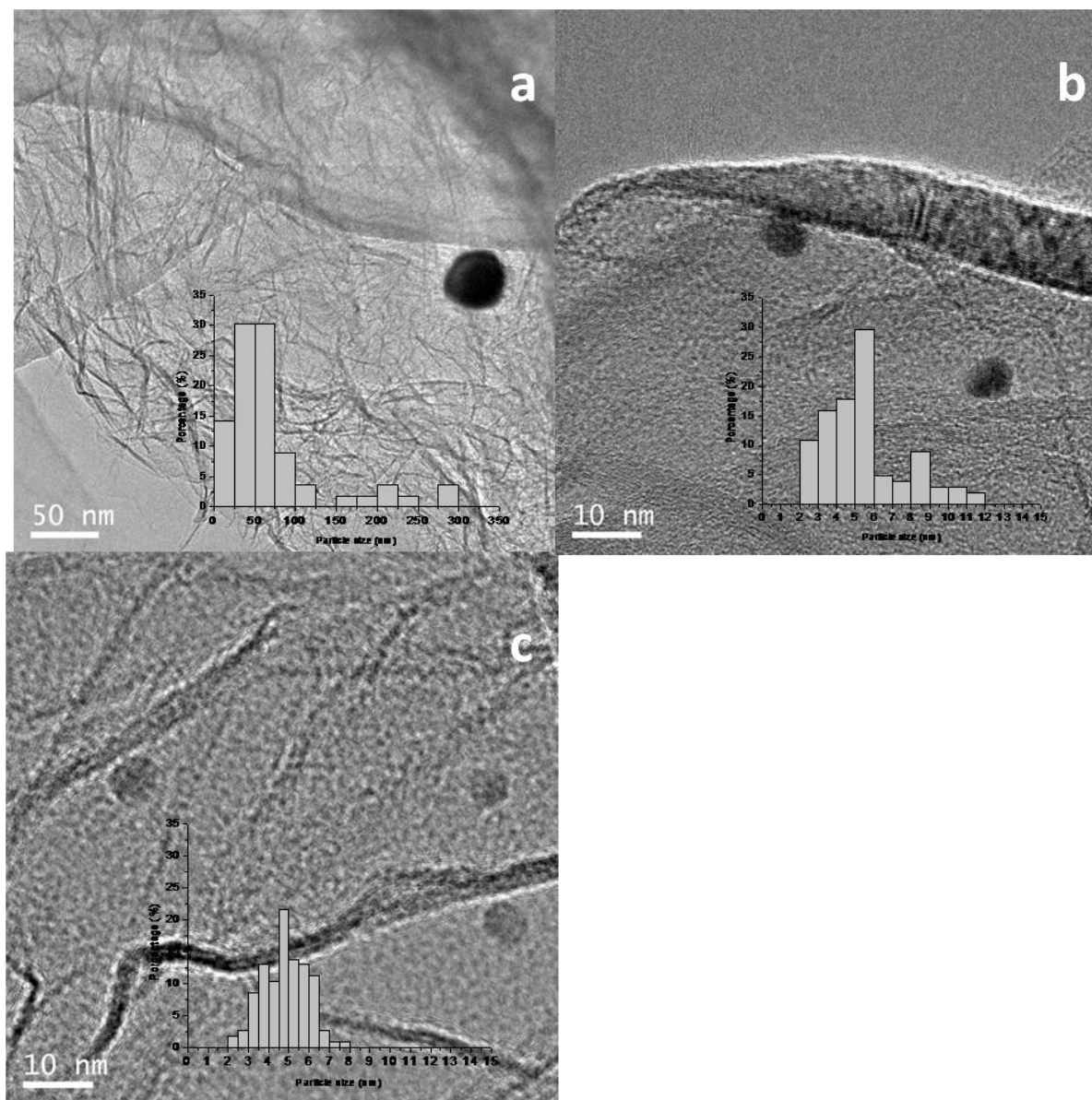
Figure 4.16 TEM images and particle size distribution of the catalysts: a) Ag/rGO, b) Au/rGO, c) Cu/rGO
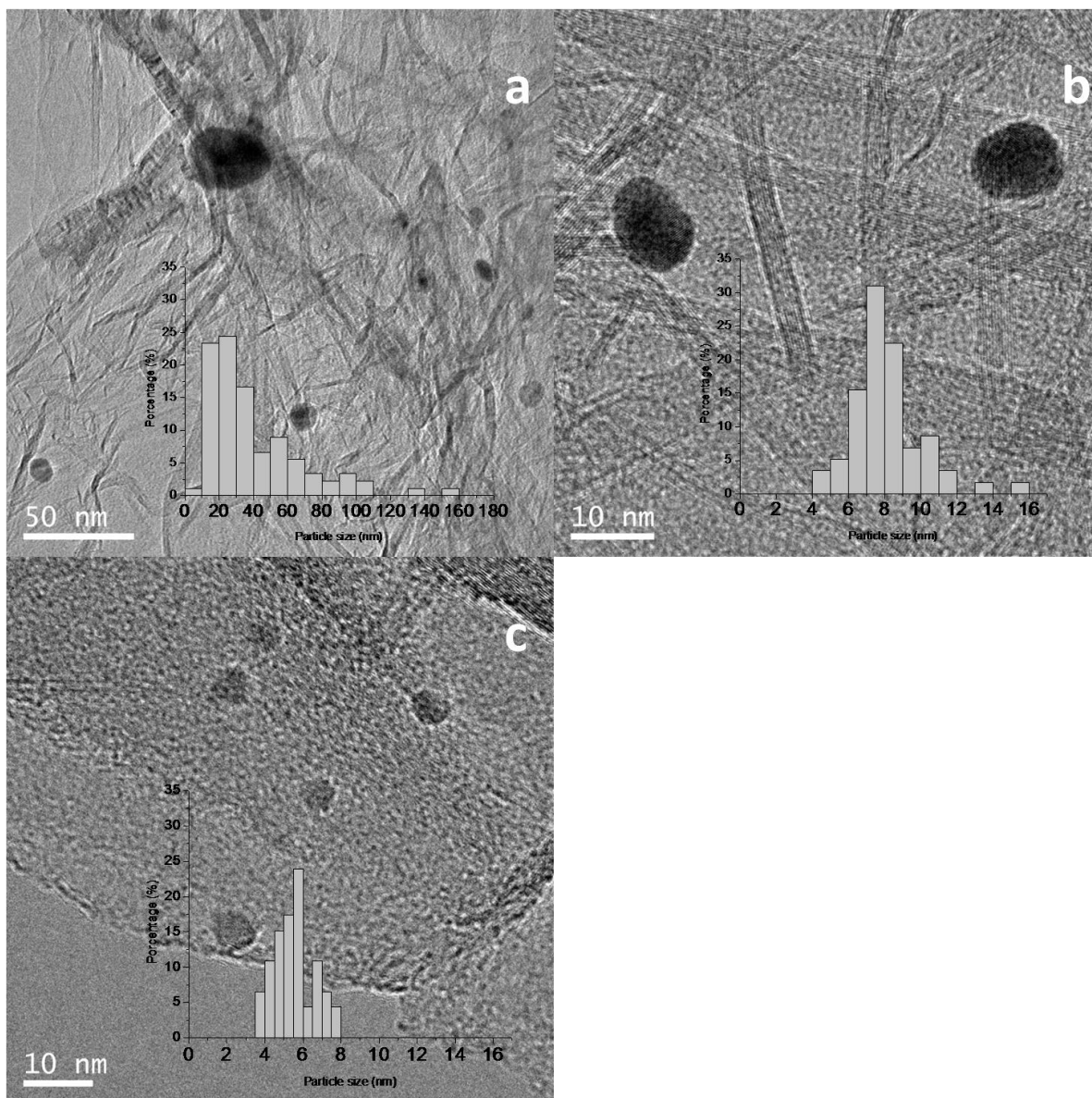
Figure 4.17 TEM images and particle size distribution of the catalysts: a) Ag/NrGO, b) Cu/NrGO, c) Au/NrGO

The XRD patterns of the catalysts prepared from different ruthenium precursors are shown in Figures 4.18 and 4.19. All the carbon supported samples showed the characteristic (002) reflection of graphitic carbon at 26º (discussed above). However, no peaks related with the formation of crystalline Ru were observed on the samples. This might be attributable to the small particle size of Ru nanoparticles in these samples, as was evidenced in the d_{TEM} values reported in Table 4.3. Regarding TiO_2, SiO_2 and Al_2O_3 supported Ru NPs, any peak related with the formation of crystalline Ru was observed on the samples neither. Small particles are below the XRD detection threshold because they do not have enough range ordering to constructively interfere with X-rays.[167] Finally the addition of metal seems not to change significantly the peak intensity at 26 degree, so the initial structures graphenic or graphitic seems not to be modified by the incorporation of the Ru nanoparticles.
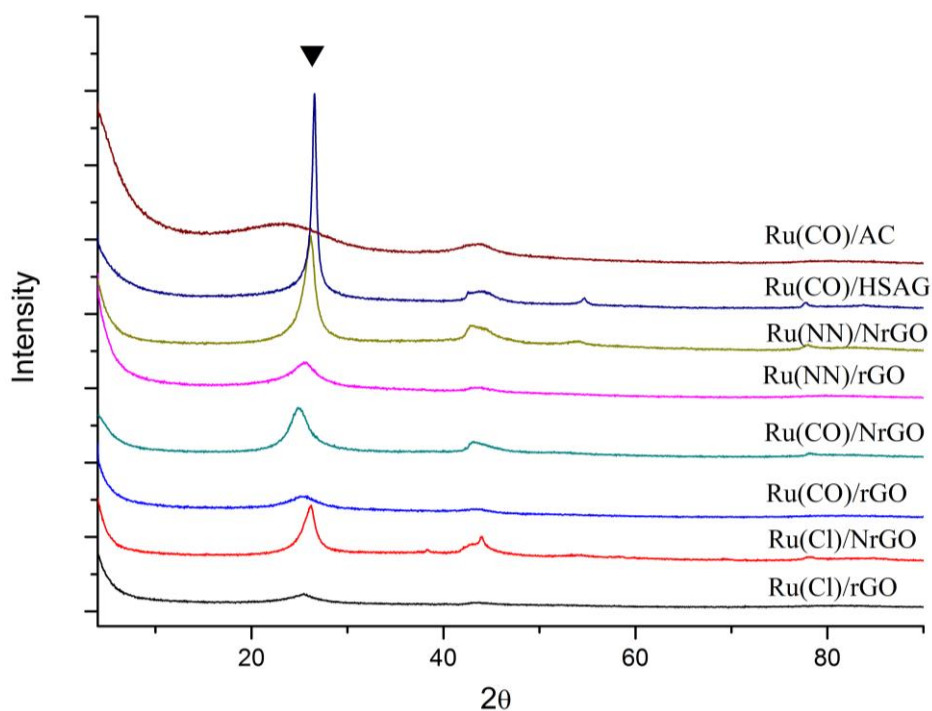
Figure 4.18 XRD patterns of Ru(Cl)/rGO, Ru(Cl)/NrGO, Ru(NN)/rGO, Ru(NN)/NrGO, Ru(CO)/rGO, Ru(CO)/NrGO, Ru(CO)/AC and Ru(CO)/HSAG after H₂ reduction at 350ºC.

The XRD patterns of the Cu, Au and Ag catalysts are shown in Figure 4.20. All the supported samples showed the characteristic (002) reflection of graphitic carbon at 26º (discussed above). X-ray diffraction patterns of Au, Ag, and Cu nanoparticles confirmed the crystalline structures of the metal catalysts.
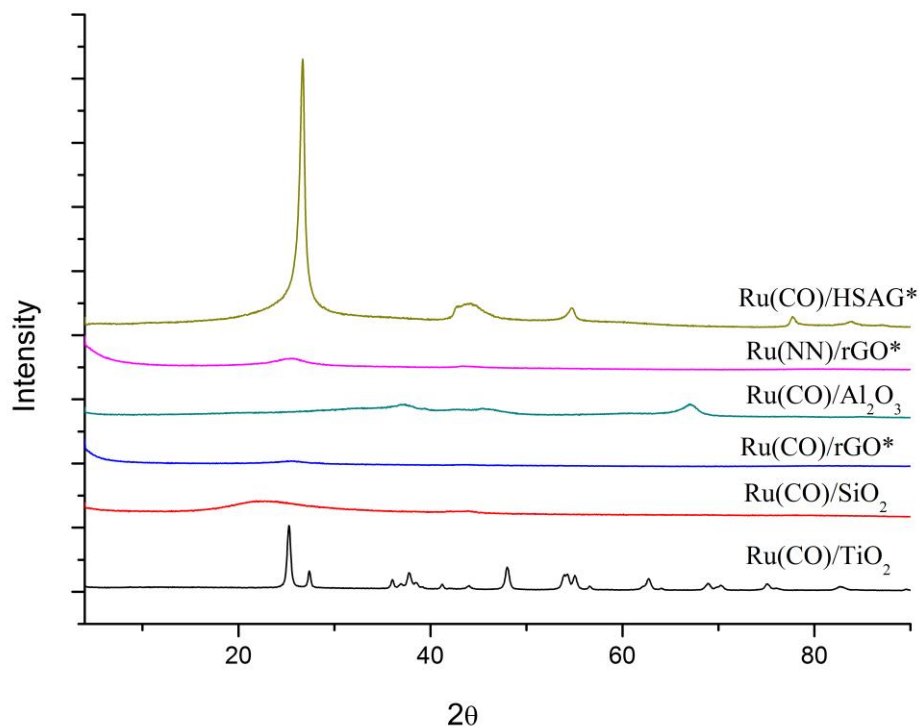
Figure 4.19 Ru(CO)/ TiO$_2$, Ru(CO)/SiO$_2$, Ru(CO)/rGO*, Ru(CO)/Al$_2$O$_3$, Ru(NN)/rGO*, and Ru(CO)/ HSAG* after reduction at 300°C(*) or 350°C.

XRD patterns of Ag/rGO and Ag/NrGO clearly reveal 5 peaks corresponding to the (111), (200), (220), (311), and (222) reflections of Ag nanocrystals. [198]

For Au/ NrGO 3 diffraction peaks can be observed at 2θ 38.2^o, 64° and 78° which correspond to the (111), (220) and (311) reflections of metallic gold, respectively.[198] Au/rGO pattern presents a small peak associated to the highest relative intensity (111) reflection. Similar observations have been made for Cu/NrGO where XRD patterns reveal 2 peaks related to (111), and (220) reflections.[198]
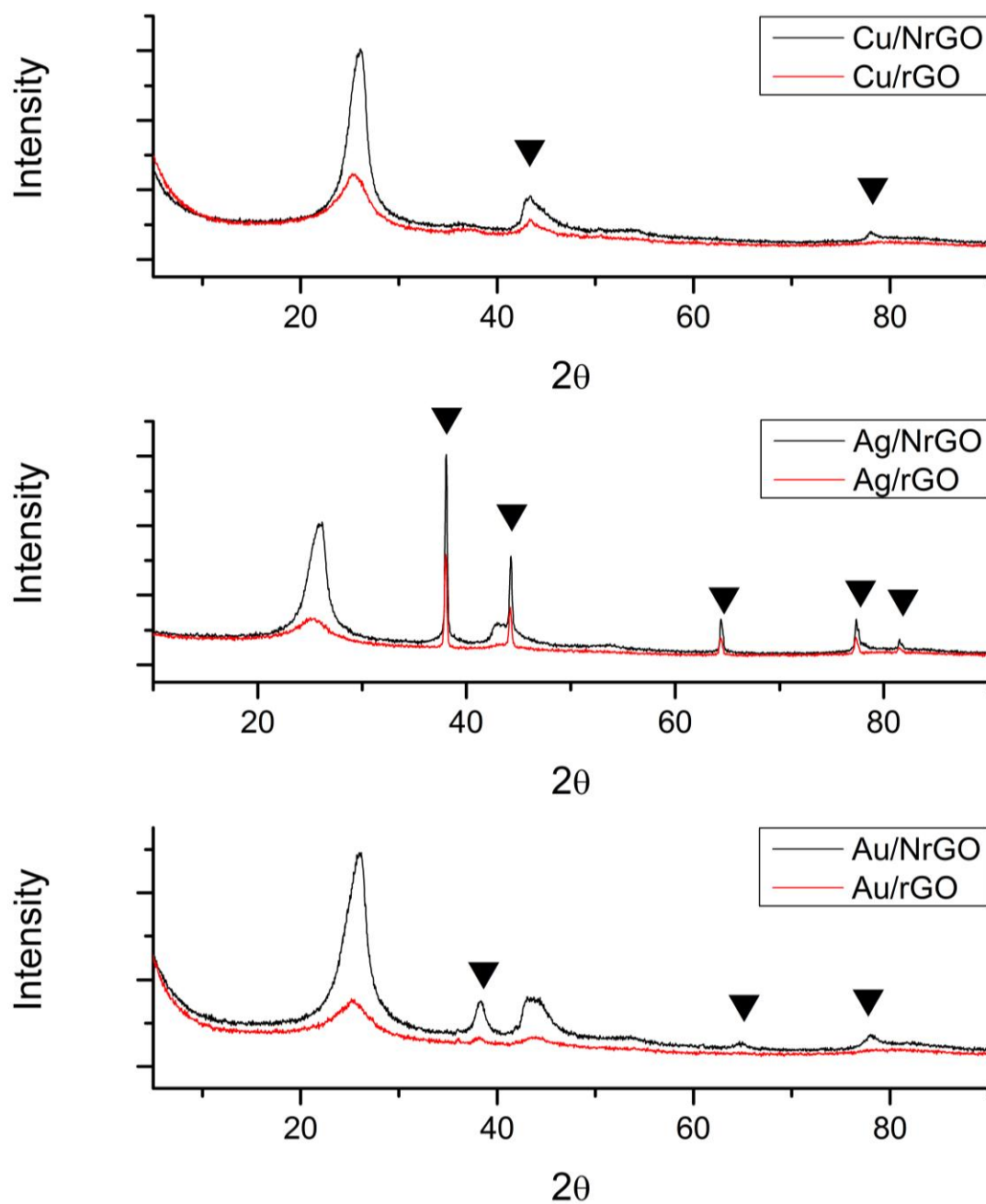
Figure 4.20 XRD patterns of Cu/rGO, Cu/rGO, Ag/rGO, Ag/rGO, Au/rGO and Au/NrGO.

XPS is a powerful technique to identify the chemical states of the surface elements, and was used to analyse the interaction of Ru nanoparticles on the different graphenic supports. Due to the partial overlapping of Ru $3d_{3/2}$ peaks with that of C 1s, the Ru 3p signal was used to study the chemical states of Ru in the samples.

The Ru 3p XPS spectrum for Ru(Cl)/rGO, Ru(NN)/rGO and Ru(CO)/rGO catalysts showed the doublet corresponding to Ru $3p_{3/2}$ and Ru $3p_{1/2}$ peaks. Notably, these peaks appeared at higher binding energies than the binding energies reported for Ru(Cl)/NrGO, Ru(NN)/NrGO and Ru(CO)/NrGO peaks respectively (Table 4.4 and Figures 4.21, 4.22 and 4.23). It can be concluded that when the Ru NPs are supported over the nitrogen-doped graphenic material, they suffer a shift in the Ru binding energies towards lower energy values when compared with rGO supported catalysts. These results suggest that the incorporation of nitrogen atoms in the graphitic structure of graphene can favor donation of electron density towards Ru active sites. This is due to a systematic electronic interaction between this support and the Ru NPs, with electron transfer from the support to the Ru when the NPs are supported on NrGO. In agreement with these results an earlier work of X. Chen et al. [199] reported that the N-doped graphene is an effective electron donor for iron nanoparticles, as revealed by Fe K-edge XANES study.

Table 4.4 XPS data of Ru catalysts.

Catalyst	BE Ru 3p$_{3/2}$ (eV)	FWHM	Ru/C
Ru(Cl)/rGO	463.0	2.4	0.001
Ru(Cl)/NrGO	462.6	3.1	0.002
Ru(NN)/rGO	463.4	3.7	0.002
Ru(NN)/NrGO	462.6	3.7	0.004
Ru(CO)/rGO	463.2	3.0	0.003
Ru(CO)/NrGO	463.1	3.3	0.003

It is noteworthy also that some residual chlorine impurities on the surface were observed in the survey scan XPS spectrum of Ru(Cl)/NrGO and Ru(Cl)/rGO catalysts.
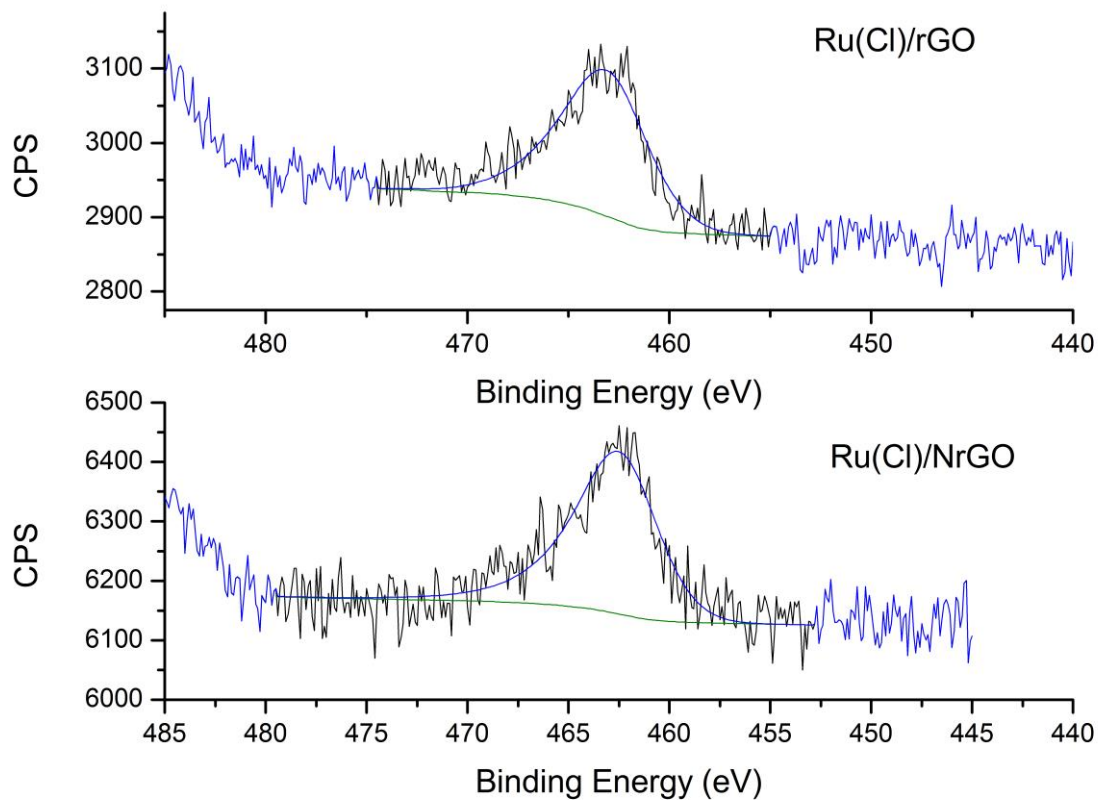
Figure 4.21 XPS spectra of 3p3/2 region for Ru(Cl)/rGO and Ru(Cl)/NrGO after H₂ reduction at 350ºC.
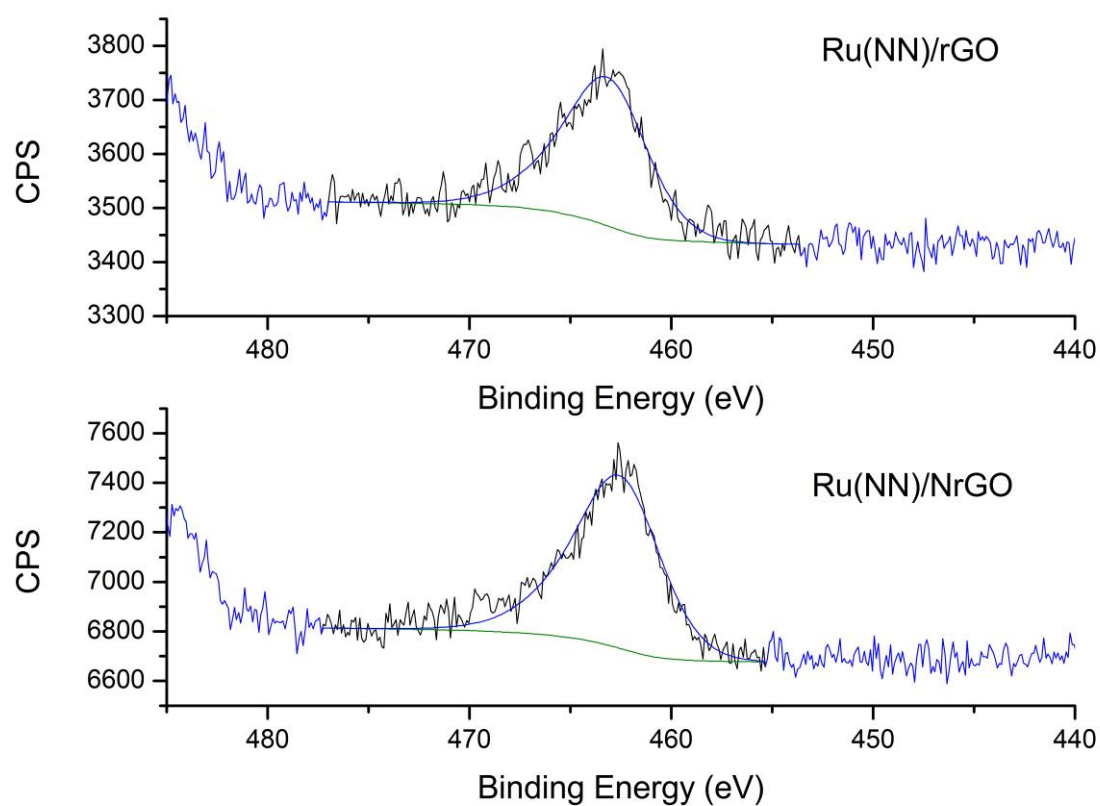
Figure 4.22 XPS spectra of 3p3/2 region for Ru(NN)/rGO and Ru(NN)/NrGO after H$_2$ reduction at 350ºC.
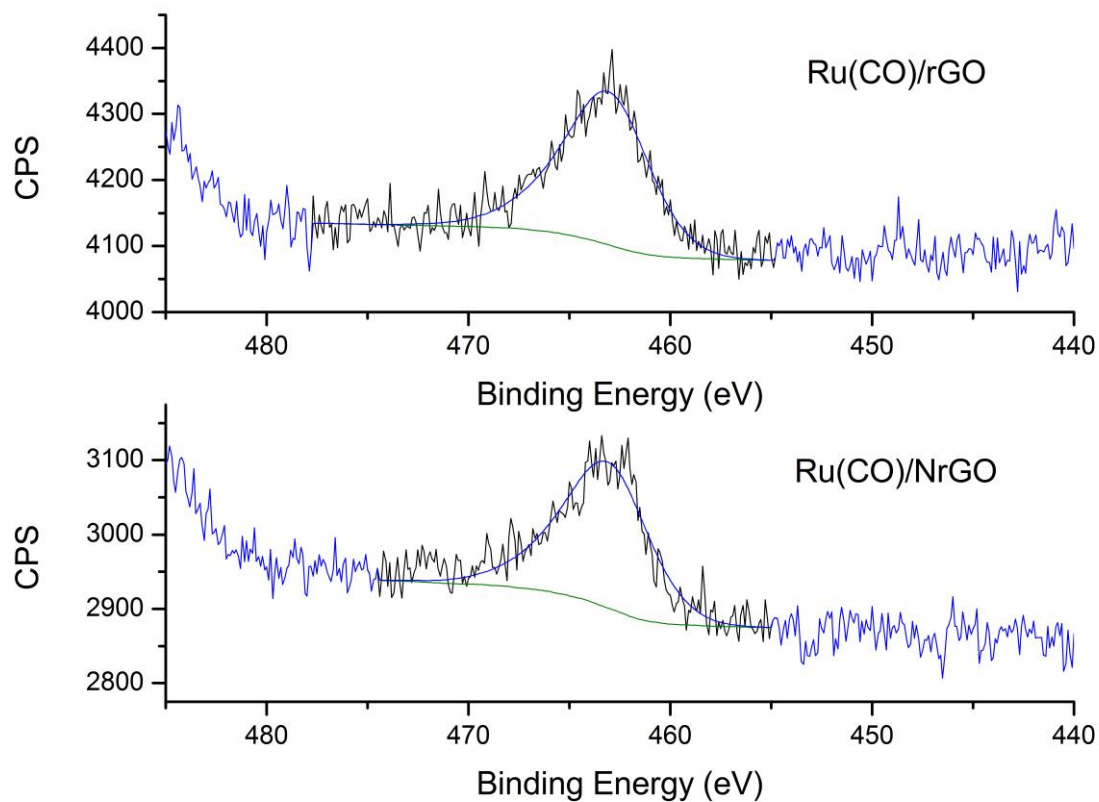
Figure 4.23 XPS spectra of 3p3/2 region for Ru(CO)/rGO and Ru(CO)/NrGO after H$_2$ reduction at 350ºC

4.3. Catalytic results

4.3.1. Oxidation of 5-HMF

4.3.1.1. Catalytic tests

Previous research with different metals (Ru, Pt) and supports (oxidic and carbonaceous materials) [42,44] demonstrates the relevance of the support in the achieved final FDCA yield (Figure 1.6 showed the reaction pathways), and that in general carbon supports are superior.

Table 4.5 lists the results of the base-free aqueous-phase oxidation of HMF to FDCA over the supported Ru catalysts prepared from different precursors. First, blank tests were carried out, without catalyst addition in the reactor, and barely formation of products was observed (entry 1 Table 4.5). Also the bare supports give very low HMF conversions (entries 2 and 3) under the proposed reaction conditions.

Table 4.5 Catalytic performance of ruthenium catalysts in the oxidation of HMF

Entry	Catalyst	Conversion (%)	Sel FDCA (%)	Sel FFCA (%)	Sel DFF (%)
1	Blank	1.6	0	0	100
2	NrGO	4.2	0	17	83
3	rGO	2.7	0	0.0	100
4	Ru(Cl)/rGO	99	49	48	3
5	Ru(Cl)/NrGO	98	43	48	9
6	Ru(NN)/rGO	100	76	24	0
7	Ru(NN)/NrGO	99	81	18	1
8	Ru(CO)/rGO	100	79	21	0
9	Ru(CO)/NrGO	100	79	21	0
10	Ru(CO)/HSAG	99	40	54	6
11	Ru(CO)/AC	99	39	59	2
12	Ru(CO)/SiO$_2$	35	10	15	25
13	Ru(CO)/TiO$_2$	50	43	8	19
14	Ru(CO)/Al$_2$O$_3$	37	46	0	32
15	Au/NrGO	14	0	47	32
16	Ag/NrGO	10	0	39	61
17	Cu/NrGO	2.5	0	0	100

Reaction conditions: HMF, 2 mmol, 50 mg of Ru catalyst (For Au, Ag and Cu catalysts see 3.4.1.1), molar ratio HMF/M=10, H$_2$O 100 ml, air 10 bars, 100ºC, 8 hours.

From Table 4.5 it can be observed that the achieved HMF conversions with nearly all the Ru studied catalysts were higher than 97.5% after 8 hr in reaction. Concerning the selectivity values significant differences can be observed depending on precursor and support. For instance, when Ru nanoparticles are supported on commercial carbons (Ru(CO)/HSAG and Ru(CO)/AC), FDCA selectivity values are significantly lower than when supported on graphenic materials. For Ru(CO)/AC, Ru(CO)/HSAG and Ru(CO)/SiO$_2$ catalysts the poor catalytic selectivities towards FDCA can be attributed to the Ru average particle sizes, 2.3 nm, 2.4 nm and 2.7 nm respectively (Table 4.3), which are significantly higher than the sizes in Ru catalysts supported on graphene supports (rGO and NrGO), in particular than those prepared with Ru carbonyl as metal precursor. Apparently an increased average metal particle size implies a reduction in the reaction rate since the progress of the consecutive oxidation reactions to reach the desired FDCA product is slower.

The catalytic behaviour of Ru based catalysts supported on rGO was compared to other metals such as Cu, Au and Ag (Table 4.5). The poor catalytic activities over Au, Cu and Ag based catalysts can be attributed to the differences in the average particle sizes (5.9, 8.1, and 40 nm for Cu, Au, and Ag respectively). Activity was remarkably low for Cu/NrGO catalyst, showing a similar conversion to a blank test.

The selectivities toward FDCA obtained with catalysts prepared from $RuCl_3$ precursor over graphenic materials were also lower than selectivity values obtained with $Ru_3(CO)_{12}$ and $Ru(NO)(NO_3)_3$ derived catalysts. The presence of chlorine impurities, that was confirmed by XPS as it was discussed above (section 4.2), can be the reason of this different behavior. This poisoning of the Ru nanoparticles[200] and a possible increase of acidity due to the presence of chlorine ions, seems to be responsible for the low selectivity towards FDCA of Ru(Cl)/rGO and Ru(Cl)/NrGO catalysts.

For catalysts prepared with both $Ru_3(CO)_{12}$ and $Ru(NO)(NO_3)_3$ precursors, higher selectivity towards FDCA was found when supported on NrGO in comparison with those supported on rGO. In Figure 4.24 the evolution of selectivity towards FDCA as the reaction is progressing is represented. Clearly a systematic support effect is evidenced. For these four catalysts, with Ru average particle sizes among 1.4 nm and 1.8 nm, as reported in Table 4.3, the possible effect of the nitrogen surface groups can be neatly evidenced. The single most noteworthy observation from these comparative data was that HMF could be completely converted, and with 79% selectivity towards FDCA, over Ru(CO)/NrGO after 8 h at 100ºC (entry 9).
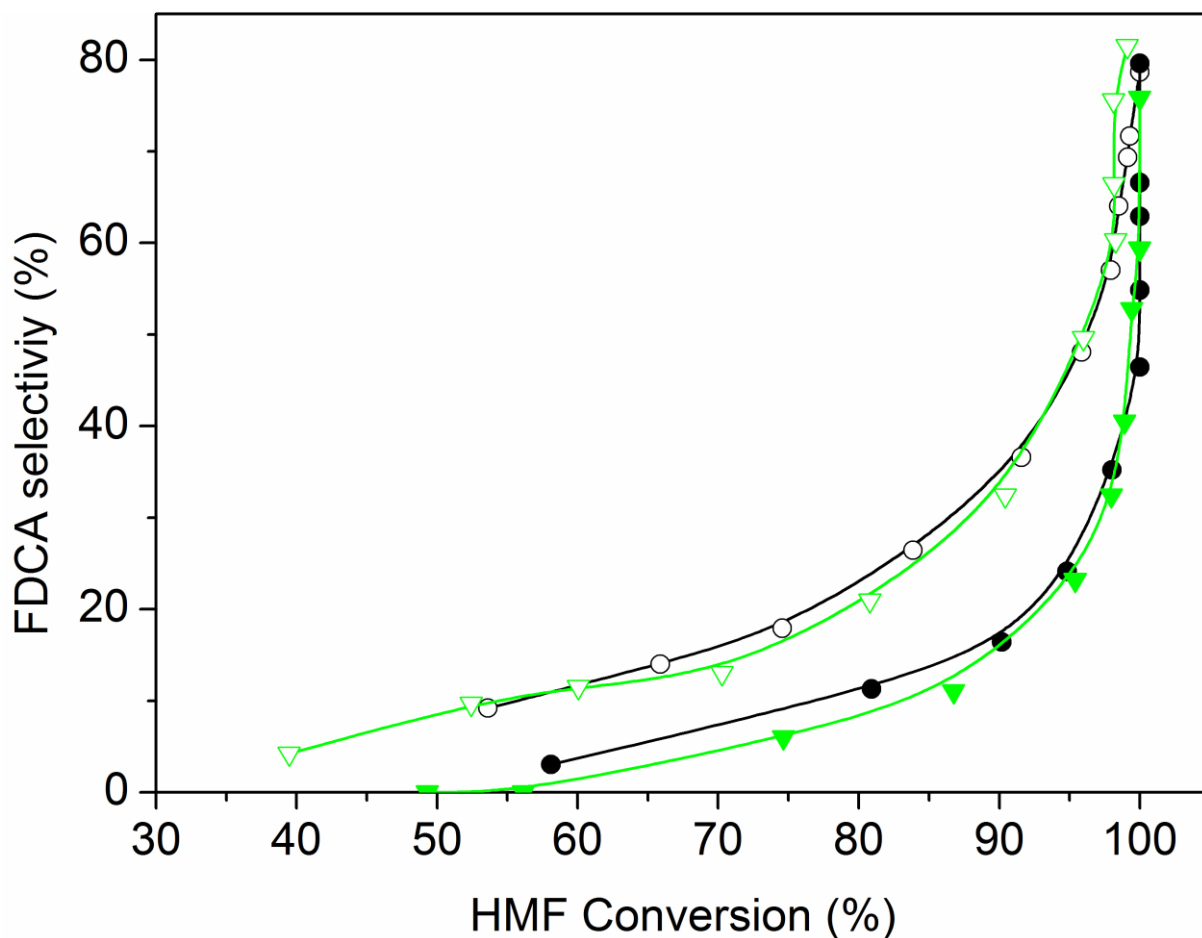
Figure 4.24 Evolution of selectivity towards FDCA during HMF oxidation reaction over Ru nanoparticles supported on nitrogen functionalized graphenic material: (○) Ru(CO)/NrGO, (▽) Ru(NN)/NrGO or on undoped graphene: (●) Ru(CO)/rGO, (▼) Ru(NN)/rGO. Reaction conditions: HMF, 2 mmol, 50 mg of catalyst, molar ratio HMF/M=10, H_2O 100 ml, air 10 bars, 100°C, 8 hours.

Results and discussion

In order to quantitatively compare the effects induced by the presence of nitrogen surface groups in the graphenic materials when used as supports, in Figure 4.25 catalyst activity is reported for each catalyst as site time yield (STY), mols of FDCA produced per mol of surface Ru per second. Clearly the two Ru catalysts supported on Nr-GO produce, in all the range of reaction time, higher selectivity values towards FDCA formation than those supported on rGO. This effect is observable for the two series of catalysts: ex-nitrosyl nitrate and ex-carbonyl. As reported in Table 4.5, entries 2 and 3, the bare support NrGO produce significant higher amount of FFCA in comparison with rGO, in spite of the low HMF conversion (Table 4.5). This FFCA is an intermediated in the formation of FDCA (Figure 1.6).

The different catalytic properties induced by Al_2O_3 and TiO_2 supports on the Ru nanoparticles, may be related with the intrinsic acid-base properties of these support materials, being Al_2O_3 an acidic support and TiO_2 an amphoteric reducible support. Besides, it is remarkable that the oxidation of 5-HMF over Ru NPs supported on oxidic materials, unlike the rest of catalysts, occurs through HFCA and DFF intermediates. Thus, under the reaction conditions used, carbon materials avoid the formation of HFCA, which could lead to ring opening and degradation products.[43]

The basic pyridinic surface groups of NGO support may also favour efficient oxidation of 5-HMF by Ru, when compared with oxidic supports. It well known that pyridinic- N groups can enhance the interactions between the NrGO surface and acid molecules, such as dipole–dipole, or hydrogen bonding[108] favouring the desorption of the products. This synergetic effect is commented below.
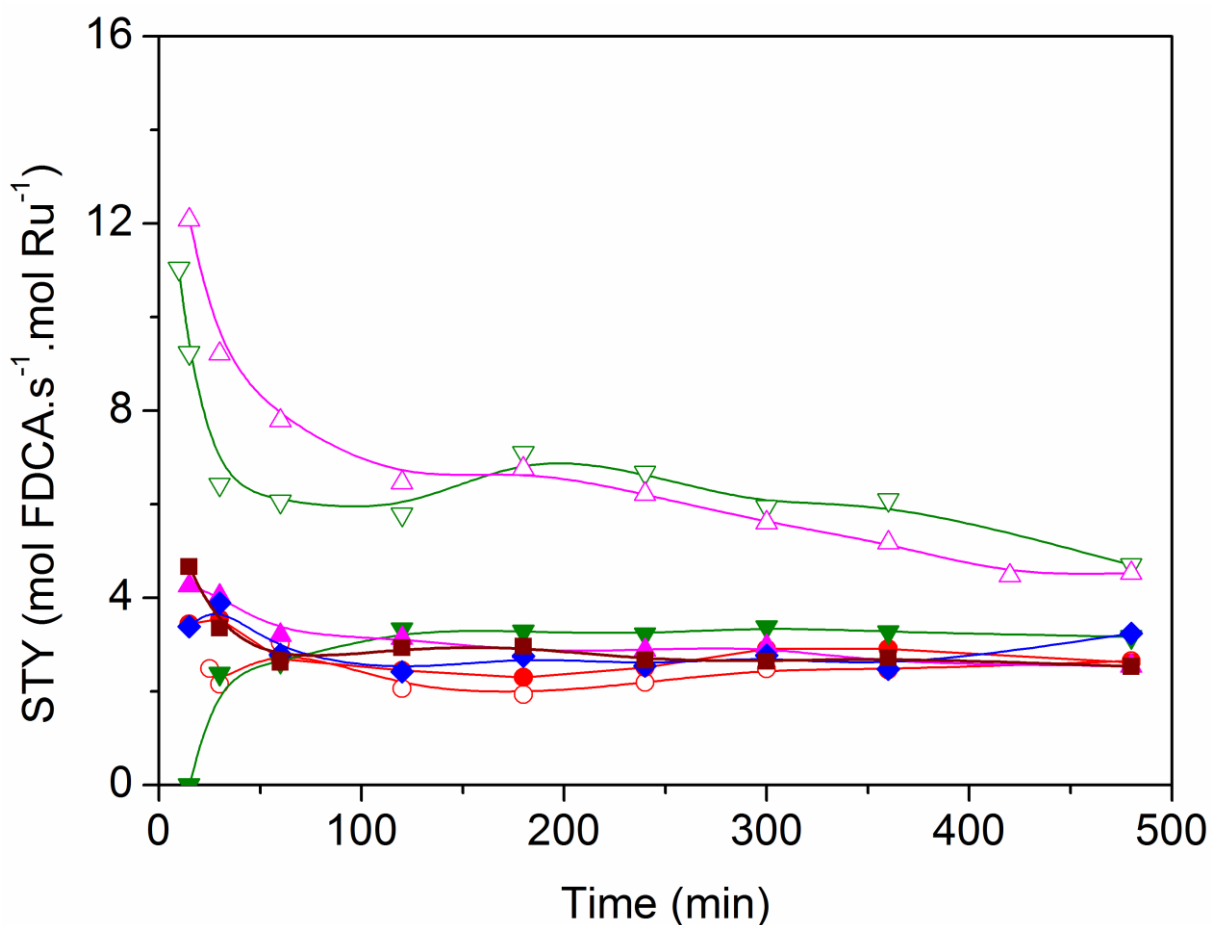
Figure 4.25 Site time yield for FDCA (STY, mol.s^{-1}.mol Ru^{-1}) with time of reaction (min) over (●) Ru(Cl)/rGO, (○) Ru(Cl)/NrGO, (▼) Ru(NN)/rGO, (▽) Ru(NN)/NrGO, (▲) Ru(CO)/rGO, (△) Ru(CO)/NrGO, (◆) Ru(CO)/AC and (■) Ru(CO)/HSAG. Reaction conditions: HMF, 2 mmol, 50 mg of catalyst, molar ratio HMF/M=10, H$_2$O 100 ml, air 10 bars, 100ºC, 8 hours.

Therefore, all these results would seem to indicate that the nitrogen functional groups significantly affect in the NrGO supported Ru catalysts, improving the selectivity to FDCA. The nature of the nitrogen effect could be thought to be twofold. On the one hand, the basic sites, as evidenced from IEP (Figure 4.8), in the case of Ru catalysts supported on NrGO, surely may contribute to the reaction in synergy with the Ru nanoparticles. However, the electron enrichment of the Ru nanoparticles, observed by XPS measurements, which could affect their activity for the HMF oxidation, can not improve the activity for the oxidation reaction, because a higher electron density of the surface Ru would disfavor both the dioxygen dissociation and the HMF chemisorption. Thus, the main hypothesis is that basic sites, in the case of Ru nanoparticles supported on NrGO, surely may contribute to the reaction in synergy with the Ru nanoparticles. In short the combination of very small Ru crystallites with some basic surface functions can act cooperatively. In a first stage oxygen and reactant are chemisorbed on the Ru surface and the production of acidic compounds (HFCA, FFCA and FDCA) starts. When FDCA is formed this is more efficiently removed from the metallic surface in the presence of basic sites exposed on the graphenic materials. These mechanistic aspects have been outlined in the Figure 4.26, and should be considered as an explanation of the results presented in Figures 4.24 and 4.25. So, this mechanism is close to that taking place when a basic compound is dissolved in the reaction media: reaction equilibrium displacement by elimination of the products from the proximity of the active surface sites. We can define this mechanism action as a cooperative effect between the surface sites exposed on the Ru nanoparticles and those basic functionalities exhibited on the nitrogen doped graphenic material (NrGO).
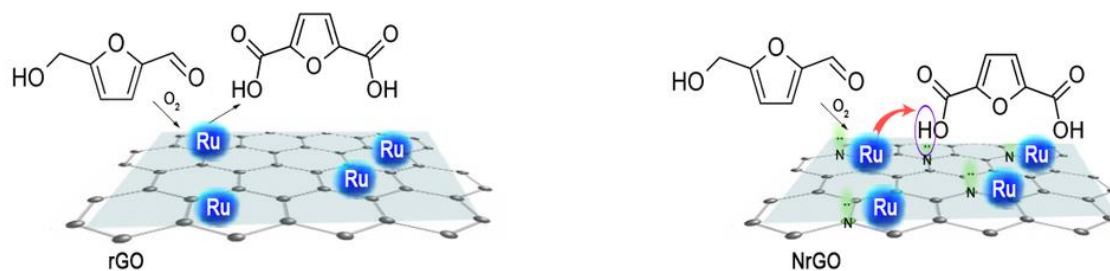
Figure 4.26 Proposal for the cooperative action of the nitrogen surface groups exposed on the doped graphenic materials and the Ru nanoparticles.

A representative example of the time course of the conversion (%) of HMF to the reaction products (%), determined using the Ru(CO)/NrGO catalyst, are presented in Figure 4.27. During the first 15 minutes, the main product was DFF. As HMF was consumed, the yield of DFF decreased and the yield of FFCA increased. The yield of the intermediates decreased and the yield of FDCA increased up to near 80% at 8 hours. Furthermore no HMFCA formation was detected. On the basis of these results, it is proposed that under the previously described experimental conditions, FDCA is produced by a stepwise reaction via DFF and FFCA as showed Figure 1.6. This tendency is in good agreement with previous studies [44] in the base-free oxidation of HMF. It is also worth noting that 85 % of HMF is converted in the first two hours indicating that the steps HMF to DFF and FFCA are faster than the reaction of transformation of FFCA into FDCA. Therefore, Ru catalysed the oxidation of –OH to –CHO, and further oxidized to –COOH, this later being the rate-limiting step.
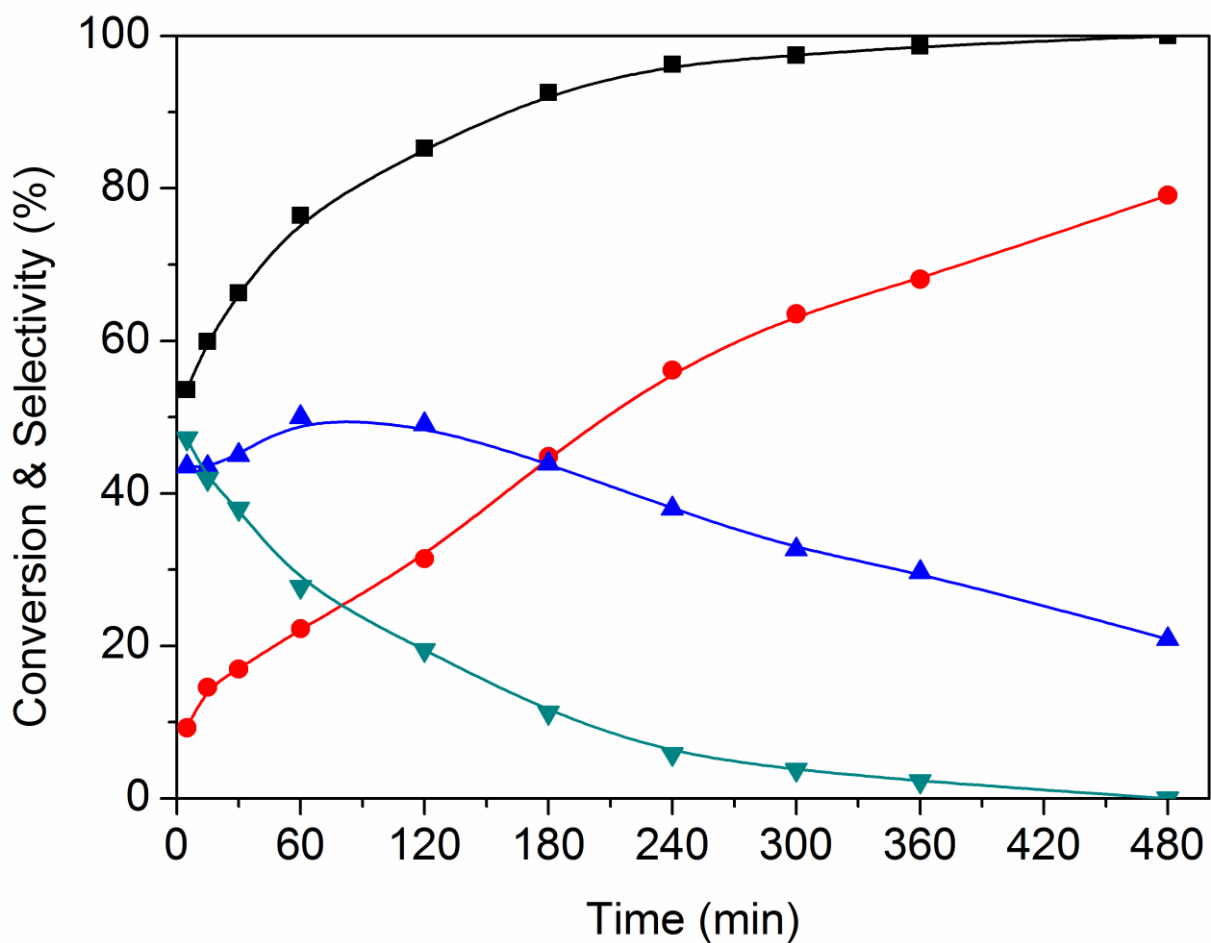
Figure 4.27 Time course of product formation for HMF oxidation over Ru(CO)/NrGO catalyst: (▼) DFF, (▲) FFCA, (●) FDCA and (■) HMF conversion. Reaction conditions: HMF, 2 mmol, 50 mg of catalyst, molar ratio HMF/M=10, H₂O 100 ml, air 10 bars, 100ºC, 8 hours.

In order to compare the catalyst that show the best performance with those previously published, in Table 4.6 are reported data obtained using different noble metal catalysts supported over diverse supports. It should be notice that in any case presented data are obtained using added base as co-catalyst and that in all the reaction studies presented in Table 4.6 water is solvent media. So these reported data are obtained under the greenest conditions. The comparison among catalysts in Table 4.6 is not easy since the reaction variables, such as temperature, pressure, reaction time or molar reactant-metal ratio, are not identical. However, Ru prepared catalysts are similar in terms of activity and selectivity with those reported with noble metals (Au, Pt) more expensive than Ru. When comparing with Ru catalysts supported on different materials, Ru(CO)/NrGO sample results slightly superior, just considering that we work at lower reaction temperature and pressure.

Table 4.6 Comparative data of HMF oxidation over different metal supported catalysts.

Catalyst	HMF:M ratio	T (°C)	O_2 pressure (bar)	Time (h)	Conversion (%)	FDCA selectivity (%)	Ref.
1,9Au/HT	40	95	1	7	100	99	[40]
2,4Ru/HT	20	140	2,5	6	100	95	[42]
2,4Ru/MgO	20	140	2,5	6	100	92	
2,4Ru/CeO$_2$	20	140	2.5	6	100	30	
1Au-1Pd/CNT	100	100	5	12	100	94	[43]
1Au-1Pd/CNT	100	100	10 (air)	12	100	96	
1Au-1Pd/CNT	100	100	5	12	100	95	
1Au-1Pd/HT	100	100	5	12	100	91	
5Pt/CNT	100	95	5	14	100	98	[44]
5Ru/CNT	100	95	5	14	47.0	2	
5Pt/HT	100	95	5	14	100	97	
5Pt/GO	100	95	5	14	100	95	
5Pt/CNT Ptto HNO$_3$	100	95	5	14	100	98	
4,32Ru/CTF-a	40	140	20 (air)	1	>99	38	[201]
5mol%Ru/C	10	120	5	10	100	88	[46]
Pt/C-O-Mg	50	110	10	12	>99	96	[202]
Pt/MgO-C	50	110	10	12	>99	96	
Ru(CO)/NrGO	10	100	10 (air)	8	100	79	present
Ru(NN)/NrGO	10	100	10 (air)	8	>99	82	work

4.3.1.2. Stability tests

In order to evaluate the stability of this Ru(CO)/NrGO catalytic material, three successive rounds were carried out with the solid recovered by filtration and washed with water. As shown in Figure 4.28, the initial conversion of HMF was maintained for at least three runs. However, the selectivity of FDCA slightly decreased during the recycle process.
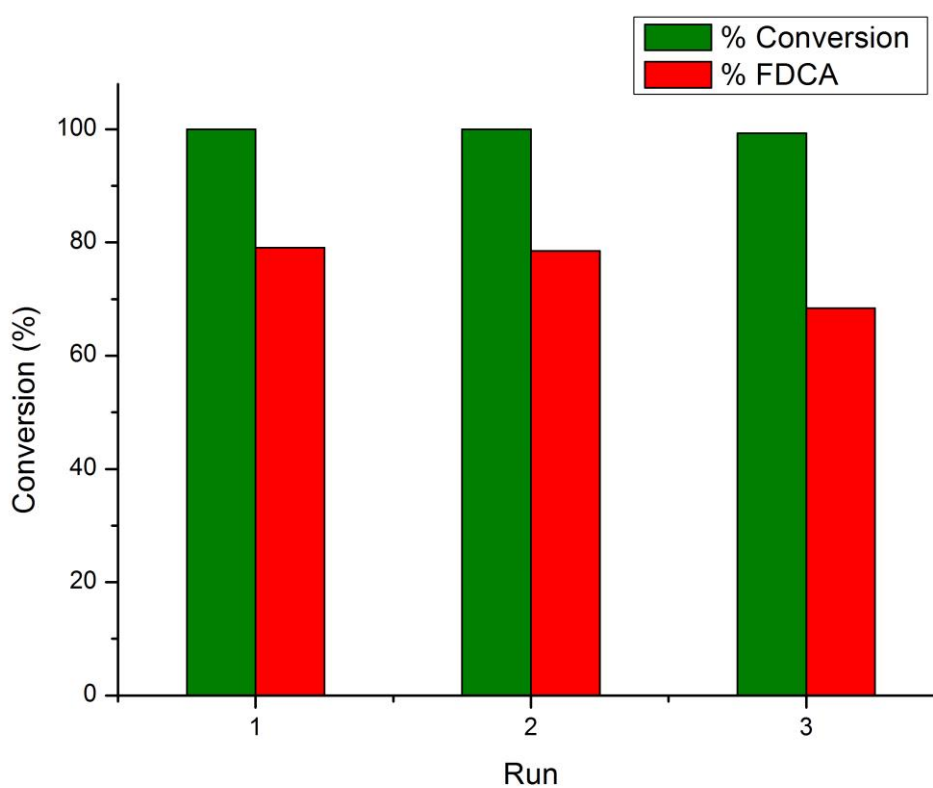
Figure 4.28 Stability of the Ru(CO)/NrGO catalyst during the recycling uses for the oxidation of HMF: (green bar) HMF conversion, (red bar) FDCA selectivity. Reaction conditions: HMF, 2 mmol, 50 mg of catalyst, molar ratio HMF/M=10, H_2O 100 ml, air 10 bars, 100ºC, 8 hours

In order to elucidate the causes of this slight catalyst deactivation a series of complementary experiments were carried out. To exclude a loss of activity produced by a Ru sintering mechanism, the spent catalysts were studied by TEM. (Figure 4.29)
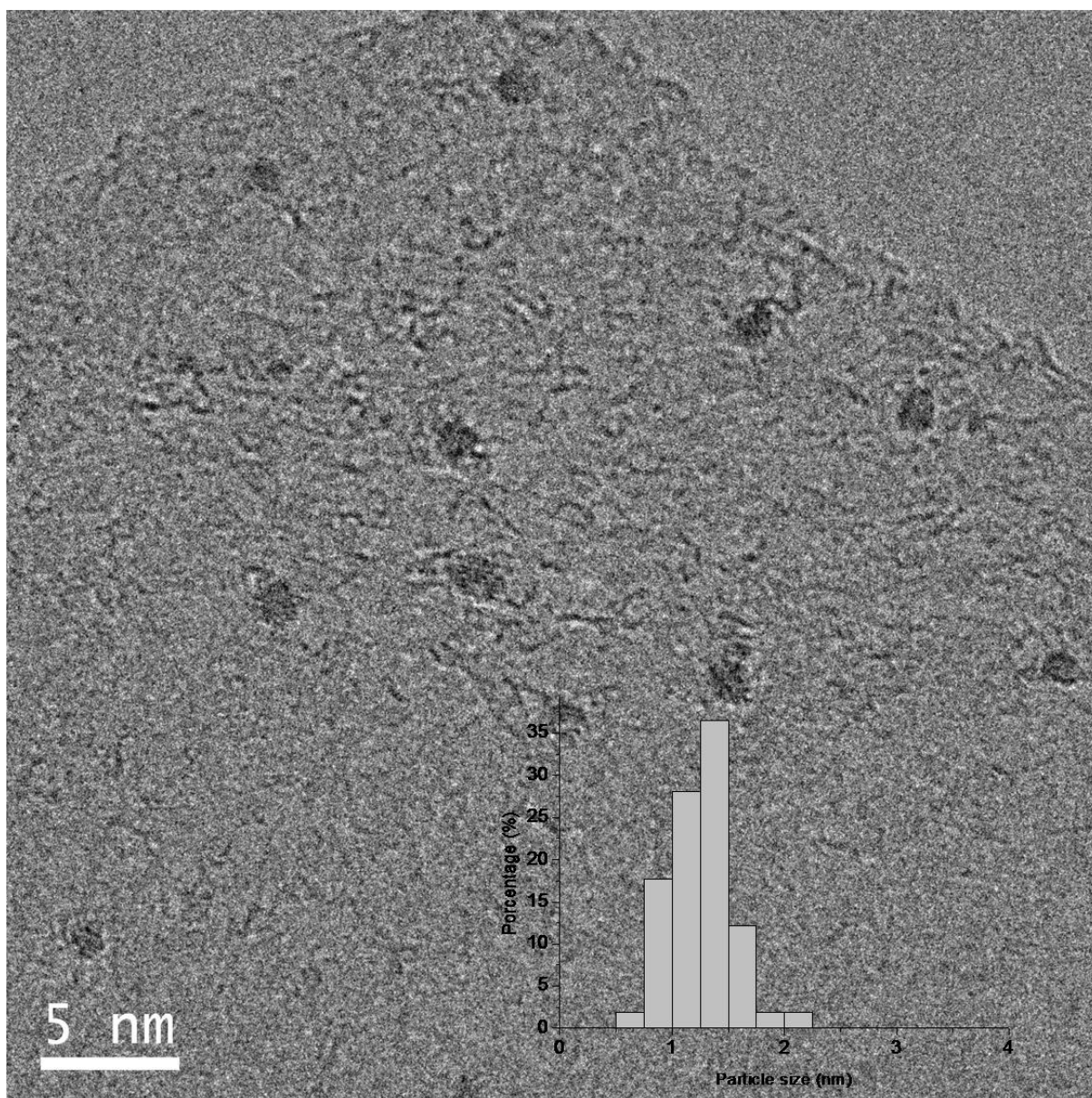
Figure 4.29 TEM image ad particle size distribution for spent Ru (CO)/NrGO

The average diameters for fresh (Table 4.3) and spent catalyst were 1.8nm and 1.4nm, respectively. Thus, no increase in the size of the particles after the recycling experiment was observed. Given the mild reaction conditions, no sintering was expected to be produced in the tested catalysts.

To study a possible change in the oxidation state of the Ru nanoparticles, XPS analyses were carried out over the spent catalysts. The Ru 3p XPS spectra of the fresh samples contain two peaks which can be assigned to Ru^0 species.[203] The XPS spectra for the spent samples upon recycling did not show any significant shift in the position of the peaks corresponding to Ru 3p (Figure 4.30). Hence, changes in the Ru oxidation states before and after reaction could not be assigned as a contribution to the deactivation of surface active sites.
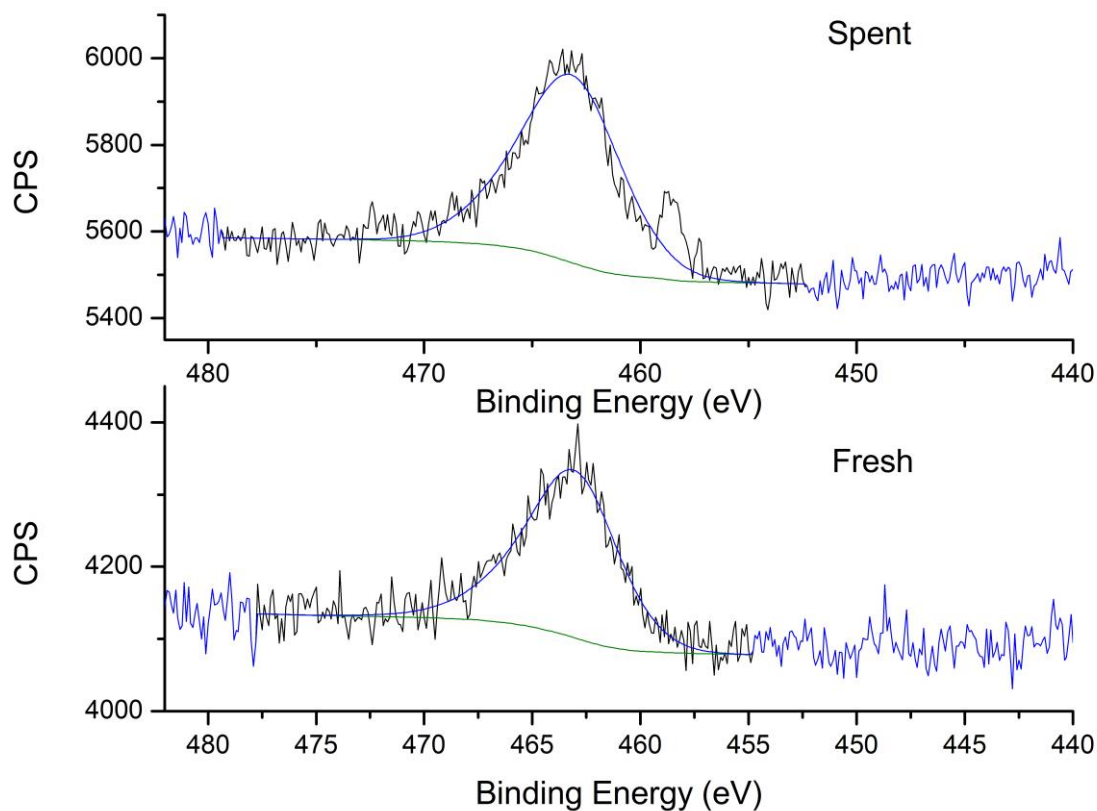
Figure   4.30 XPS spectra of 3p3/2 region for fresh Ru(CO/NrGO and spent Ru(CO)/NrGO catalysts

Finally, the concentration of potentially leached ruthenium in the aqueous solution was analysed by ICP-EOS. For post-reaction solutions obtained from the Ru(CO)/NrGO catalyst after the three stability runs, no ruthenium was detected.

Taken together, these results demonstrate that the sintering of Ru nanoparticles, the oxidation of Ru species, and the leaching of ruthenium could be discarded as possible explanations for the decrease in the activity of the Ru catalysts.

The slight deactivation could be related to a small loss of mass during recovery of the catalyst between cycles and/or with a blocking of the support basic surface sites by some adsorbed reaction products. Thus all these results demonstrated the outstanding stability and reusability of the improved Ru(CO)/NrGO catalyst.

4.3.2. Hydrogenation of furfural

4.3.2.1. Catalytic tests

Table 4.7 summarizes the results obtained for the hydrogenation of FAL to FOL in water at room temperature (20ºC) and 10 bars of H_2 over the Ru catalysts prepared from different precursors and with different support materials. Negligible conversion of products was observed in blank tests carried out without catalyst under the reaction conditions used (entry 1) and with the bare rGO itself (entry 2), showing that Ru metallic sites are indispensable for catalytic FAL conversion.

The activities obtained with catalysts prepared from $Ru(NO)(NO_3)_3$ and $Ru_3(CO)_{12}$ precursors over rGO (entries 4 and 5) were higher than the activity observed using a $RuCl_3$ derived catalyst (entry 3). The presence of residual chlorine on the surface of the Ru(Cl)/rGO catalyst has been reported in the section 4.2, possibly the poisoning of Ru nanoparticles by anchored chlorine atoms, blocking and reducing the number of active sites, seems to be the reason of this different behaviour. On the other hand, using $Ru(NO)(NO_3)_3$ and $Ru_3(CO)_{12}$ derived catalysts, FAL conversions of 73% and 83% respectively with 98% selectivity towards FOL were reached after 5 hours.

Table 4.7 Catalytic performance of ruthenium catalysts in the hydrogenation of FAL

Entry	Catalyst	Conversion (%)	Sel FOL (%)	Sel THFA (%)
1	Blank	3.2	100	0
2	rGO	3.0	100	0
3	Ru(Cl)/rGO	49	98	2
4	Ru(NN)/rGO	73	98	2
5	Ru(CO)/rGO	83	98	2
6	Ru(CO)/NrGO	63	97	3
7	Ru(CO)/HSAG	46	99	1
8	Ru(CO)/AC	55	99	1
9	Ru(CO)/Al_2O_3	28	100	0
10	Ru(CO)/SiO_2	30	100	0
11	Ru(CO)/TiO_2	25	100	0
12	Ru(NN)/rGO[a]	93	97	3
13	Ru(CO)/rGO[a]	93	98	2
14	Ru(CO)/HSAG[a]	50	98	2
15	Au/rGO	8.1	100	0
16	Cu/rGO	4.7	100	0
17	Ag/rGO	2.0	100	0

Reaction conditions: FAL, 1.56 mmol, 25 mg of of Ru catalyst (For Au, Ag and Cu catalysts see 3.4.2.1), molar ratio FAL/M=157, H_2O 50 ml, H_2 10 bars, 20ºC, 5 hours. Reduction temperature 350ºC. [a] Reduction temperature 300ºC

Several Ru catalysts prepared using $Ru(CO)_{12}$ as Ru precursor over different supports (entries 5-11) were tested under the same reaction conditions. The supports studied include rGO, NrGO, AC, HSAG, SiO_2, Al_2O_3 and TiO_2. From Table 3 it can be seen that the achieved FOL selectivities with all the Ru studied catalysts were higher than 97%. Interestingly, when rGO was replaced by other support materials lower conversions (25-63% versus 83%) were observed. For $Ru(CO)/AC$, $Ru(CO)/HSAG$, $Ru(CO)/SiO_2$ and $Ru(CO)/NrGO$ catalysts the poor catalytic activities can be attributed to the differences in Ru average particle sizes (1.8-2.7 nm Table 4.3) compared with the $Ru(CO)/rGO$ catalyst (1.4 nm). Furthermore the outstanding catalytic performances of $Ru(CO)/rGO$ and $Ru(NN)/rGO$ can be also associated with the narrow mean particle size of Ru (see histograms in Figures 4.14 and 4.15) and the high dispersion of Ru nanoparticles, aspects that we have related to the noteworthy high surface area of this support (867 $m^2 g^{-1}$).

Moreover, it was comparatively investigated the catalytic behaviour of Ru based catalysts supported on rGO with other metals such as Cu, Au and Ag. Table 4.7 show that over Au, Cu and Ag based catalysts, a maximum conversion of 8.1% is obtained. The poor catalytic activities can be attributed to the differences in the average particle sizes (4.8, 5.5, and 73 nm for Cu, Au, and Ag respectively). The absence of active surface sites was more remarkable for Ag/rGO catalyst, being inactive for the hydrogenation of furfural under the experimental conditions used.

Relevantly, the considerable difference in terms of catalytic activity observed over $Ru(CO)/Al_2O_3$ and $Ru(CO)/TiO_2$ catalysts (entries 9 and 11 respectively) compared to $Ru(CO)/rGO$, cannot be attributed to the Ru crystallite sizes, as all these catalysts have very small Ru particle size (Table 4.3). The different catalytic properties induced by Al_2O_3 and TiO_2 supports on the Ru nanoparticles, may be related with the intrinsic acid-base properties of these support materials, with Al_2O_3 an acidic support and TiO_2 an amphoteric reducible support. However, rGO is an inert support with outstanding surface properties originated from high surface area and weaker electronic interactions with the Ru nanoparticles. Thus, the inert surface of this rGO support may also favour efficient hydrogenation of FAL by Ru, when compared with oxidic supports, due to rGO offers large specific surface area, improved diffusion of reactant and product and absence of chemisorption on this carbon support, could act accelerating the catalytic process. Thus, once furfuryl alcohol is formed on the surface of catalyst, it would leave quickly and then be replaced by new reactant molecules.

In short, undoubtedly, the support plays a key role in the performance of the studied Ru catalysts and among the examined supports; rGO is the most preferable for the hydrogenation of FAL.

Comparison of three Ru catalysts Ru(NN)/rGO, Ru(CO)/rGO, and Ru(CO)/HSAG reduced under H_2 at 350 ºC (entries 4, 5 and 7) and at 300ºC (entries 12-14) reveals that catalytic activity, in the aqueous-phase hydrogenation of FAL, can be optimized. This reduction temperature dependence of the catalytic results is displayed in Figure 4.31. Systematically smaller Ru nanoparticles obtained pre-treating the catalysts at 300ºC (Table 4.3) are more active in the FAL hydrogenation than those reduced at 350ºC. For instance, Ru(CO)/HSAG gives a conversion of 46% when is reduced at 350ºC, increasing this value to 50% by the use of a lower pre-treatment temperature. The most noteworthy remark from these comparative data is that, with this catalyst Ru(CO)/rGO, FAL can be almost completely converted, and with 98% of selectivity towards FOL. The same behaviour is obtained using Ru(NN)/rGO, 97% of selectivity towards FOL, when reduced at 300ºC (entry 13). Thus we have been able to optimize a supported catalyst, combining the surface properties of rGO and very small Ru NPs, which permits to achieve near 100% yield FOL from FAL.
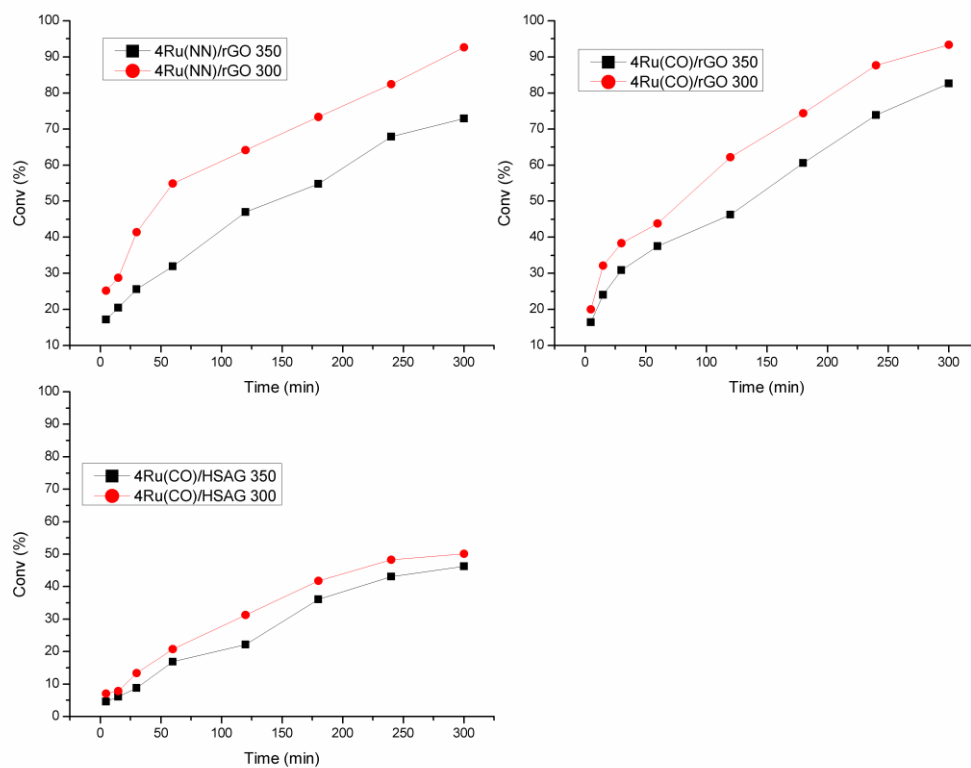
Figure 4.31 Conversion of FAL into FOL over Ru(CO)/rGO, Ru(NN)/rGO and Ru(CO)/HSAG reduced at 350ºC and 300ºC. Reaction conditions: FAL, 1.56 mmol, 25 mg of catalyst, molar ratio FAL/M=157, H_2O 50 ml, H_2 10 bars, 20ºC, 5 hours.

A comparative evaluation between Ru(CO)/rGO catalyst with those previously published is summarized in Table 4.8. It should be notice that in all reactions presented in Table 4.8, water was the solvent (or the reaction media). The comparison among catalysts in Table 4.8 is not straightforward since the reaction condition variables, such as temperature, pressure, reaction time or molar reactant-metal ratio, are not similar. However, considering that we work at lower reaction temperature and/or higher molar reactant-metal ratio, the performance of the graphene material supported Ru catalysts is clearly superior to those reported in the literature.

Table 4.8 Comparative data of the FAL hydrogenation over different metal supported catalyst using water as solvent media

Catalyst	FAL:M ratio	T (°C)	H_2 pressure (bar)	Time (h)	Conversion (%)	FOL selectivity (%)	Reference
2%Pd-1%Ir/SiO$_2$	480	20	80	6	100	<1%	[204]
5%Pd-1.5%Cu/Al$_2$O$_3$	6	90	20	2	100	41	[70]
5%Cu/Al$_2$O$_3$	6	90	20	2	81.0	100	
1.5%Pd/CNT	856	50	5	-	95.0	52	[72]
1.5%Ru/CNT	856	50	5	-	14.0	88	
5%Pd-5%Cu/MgO	133	130	8	0.9	100	99	[71]
3%Ru/Al-MIL-53s	40	20	5	2	100	>99.9	[73]
5%Pd/C$_3$N$_4$	376	100	10	5	>99	>99	[57]
3%Ru-2.5%Sn/AC	0.7	90	12.5	5.5	90.0	95	[74]
Ru(CO)/rGO	157	20	10	5	93.3	98	This work
Ru(NN)/rGO	157	20	10	5	92.7	98	This work

4.3.2.2. Stability tests

Based on the above catalytic results, we have examined the stability of Ru(CO)/rGO and Ru(NN)/rGO catalysts reduced at 300ºC, in particular, their reusability. Four successive rounds were conducted with the solid recovered by filtration and washed thoroughly with water. As shown in Figure 4.32, for Ru(NN)/rGO, the initial conversion of FAL was maintained for at least two runs, for the third and fourth runs the conversion of FAL strongly decreased during the recycling experiment. No loss in the selectivity towards FOL was

observed. Therefore, a clear reduction in the intrinsic activity was observed for the Ru (NN)/rGO catalyst. For Ru(CO)/rGO no catalyst deactivation was observed after 3 rounds. For the fourth round, conversion of FAL slightly decreased. Also the selectivity to FOL kept stable during the recycle process. This indicates that Ru(CO)/rGO catalyst was generally stable showing a minor deactivation during the recycling experiment. Consequently, in a first step Ru(CO)/rGO exhibit better stability upon reuse compared to Ru(NN)/rGO.
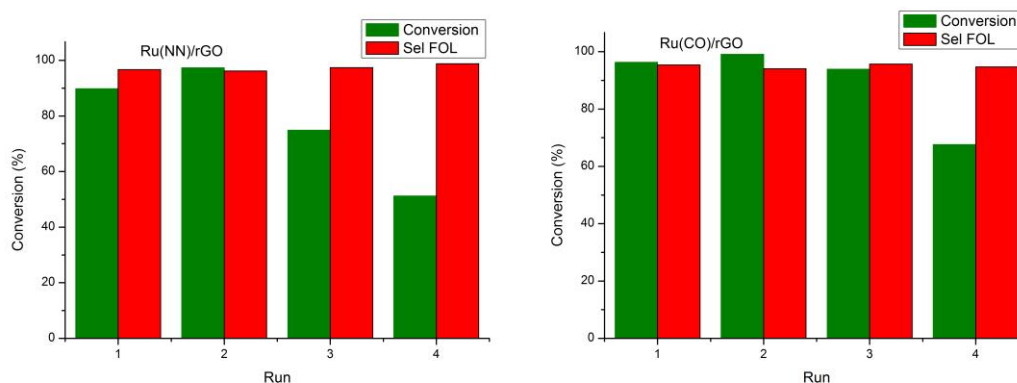
Figure 4.32 Stability of the Ru(NN)/rGO, and Ru(CO)/rGO catalysts during the recycling uses for the hydrogenation of Furfural. Reaction conditions: FUR 1.56 mmol, 25 mg of catalyst, molar ratio FAL/M=157, H$_2$O 50 ml, H$_2$ 10 bars, 20°C, 5 hours.

In order to elucidate the causes of the catalyst deactivation a series of complementary experiments were carried out. So the concentration of potential leached ruthenium in the filtered aqueous solution was studied by ICP-OES. For the hydrogenation solutions obtained from the Ru(NN)/rGO and Ru(CO)/rGO catalysts after the recycling experiments, no detectable leaching of ruthenium was identified. To preclude a loss of activity produced by a Ru sintering mechanism, the spent catalysts were studied by TEM (Figure 4.33).
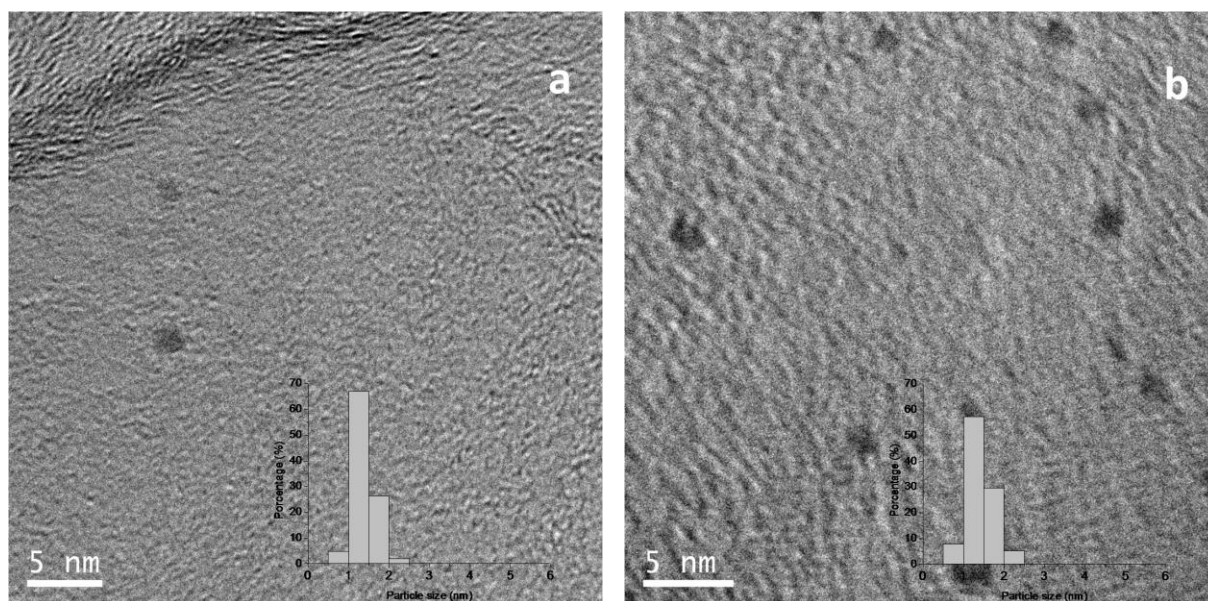
Figure 4.33 TEM images and particle size distributions for spent catalysts: a) Ru(CO)/rGO and b) Ru(NN)/rGO.

Based on the TEM measurements (Table 4.9 and Figure 4.33), a slightly increase in the mean diameters of the Ru nanoparticles and no essential changes in the particle size distribution after the fourth cycles were observed. Given the mild reaction conditions, no sintering was expected to be produced in the tested catalysts.

To study a possible change in the oxidation state of the Ru nanoparticles, XPS analyses were carried out over the spent catalysts. The XPS experiments of the fresh and spent samples were carried out at the European Bioenergy Research Institute (EBRI) of Aston University (Birmingham-UK). The catalyst were analysed by X-ray photoelectron spectroscopy (XPS) using a Kratos AXIS Supra spectrophotometer, which operated with a monochromatic Al K_α source (1486.7 eV). Spectra were analysed with CasaXPS software and RSF database by fitting after Shirley background correction.

The Ru 3p XPS spectra of the fresh samples contain two peaks which can be assigned to Ru^0 species.[203] The XPS spectra for the spent samples upon recycling show an increase of oxygen content in the samples that concomitantly can be due to adsorbed reactant or products in the spent catalysts (see below TPD experiments). Also a shift in the position of the peaks corresponding to Ru 3p to higher binding energy values (Table 4.9) that could be partly due to oxidation of the Ru^0 particles[205] to RuO_2, probably occurred during the transfer and manipulation of the sample during the characterization process, was observed for the two catalysts. Hence, changes in the Ru oxidation states before and after reaction could not be assigned as contribution to the deactivation of the active sites.

Table 4.9 XPS and TEM characterization of the fresh and spent Ru(NN)/rGO and Ru(CO)/rGO catalysts.

Catalyst	d_{TEM}(nm)	O (%)	BE Ru $3p_{3/2}$ (eV)
Ru(NN)/rGO fresh	1.3	6.2	462.3
Ru(NN)/rGO spent	1.4	11.8	463.1
Ru(CO)/rGO fresh	1.3	6.1	462.7
Ru(CO)/rGO spent	1.4	10.9	463.1

Temperature programmed desorption (TPD) experiments with MS analysis of the gases evolved were also carried out to exclude possible irreversible chemisorption of one of the reaction products on the surface of the Ru(CO)/rGO catalyst that can cause the deactivation phenomena. This thermal desorption study (TPD) allows to identify the desorbed products and to discern between chemisorbed and physisorbed products in base to the strength of the adsorption and its thermal stability. These experiments, carried out over aliquots of the catalyst that have been 20 hours in contact with aqueous solutions containing FAL, FOL or THFA, are shown in Figure 4.34.

The evolved FAL, FOL and THFA appears as desorption profiles, following in the MS univocal molecular ions (95, 98 and 71, respectively).

In the FAL desorption the most abundant specie of the obtained spectra appear at m/z=95. Considering that boiling points of FAL is 162ºC, and that desorption profiles of FAL appear in the range 120-155 ºC we have consider this peak as due to physisorbed FAL. Also it can be appreciated a small shoulder at about 230ºC, assignable to some species of chemisorbed FAL. In this experiment negligible peaks for m/z values 98 and 71 were detected, so in the absence of hydrogen FOL is not produced.

FOL desorption is followed by the m/z=98 ion. Considering that boiling point of FOL is 170 ºC, the peaks located at 170-225 ºC can be associated to physisorbed species. The small peak at 270ºC should correspond to traces amounts of chemisorbed FOL. The simultaneous evolution of FAL (m/z = 95) possibly indicates the dehydrogenation of FOL during the run of the TPD experiment, as no FAL was detected in the solution after the adsorption process (analysed by GC).

Finally THFA, who boiling point is 178 ºC, was followed by the signal m/z=71. The lack of m/z=71 during the TPD suggests that physical adsorption of THFA is not taking place. At this point we can assume that the observed physisorbed species might be located on the support surface, while the chemisorbed ones would be in interaction with the Ru nanoparticles. This spatial distribution in the catalyst could explain the reduced amount of chemisorbed species in comparison with physisorbed ones. Nevertheless, the presence of strong adsorption sites able to chemisorb FOL seems to indicate that the slight deactivation of Ru(CO)/rGO catalyst after 4 runs could be caused by obstruction of metallic sites by FOL.
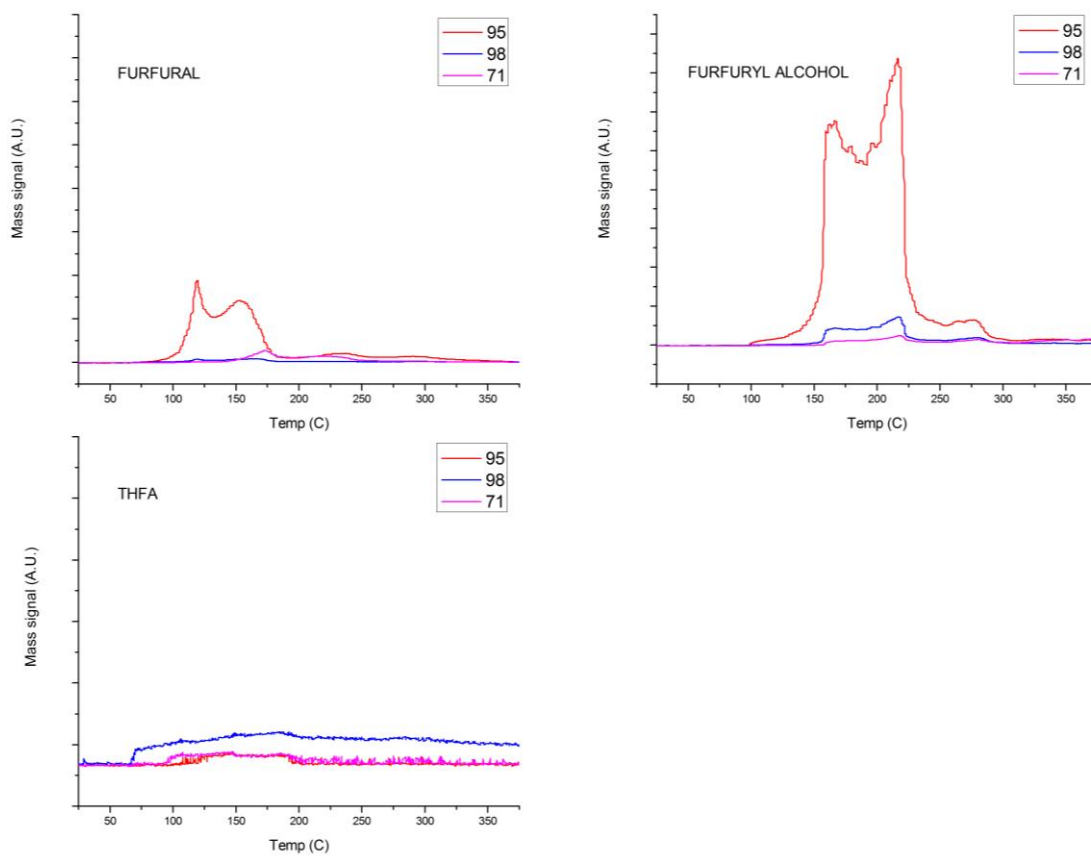
Figure 4.34 TPD-MS of FAL, FOL and THFA from thermally treated catalyst

Taken together, these results demonstrate that the sintering of Ru nanoparticles, the oxidation of Ru species, and the leaching of ruthenium could be discarded as possible explanations for the decrease in the activity of the Ru catalysts. Thus, the slight deactivation could be related to a small loss of mass during recovery of the Ru(CO)/rGO catalyst between successive runs and/or to the irreversible chemisorption of FOL over the Ru active sites. But the relevant finding is that these results prove that the highly active Ru(CO)/rGO catalyst shows excellent reusability under the employed reaction conditions, without significant loss of catalytic activity or selectivity.

4.3.3. Oxidation of benzyl alcohol

The following experiments were carried out during a 3 month stay at the European Bioenergy Research Institute (EBRI) of Aston University (Birmingham-UK). In Figure 1.12 was schematized the principal products of this partial oxidation reaction (benzaldehyde and benzoic acid).

4.3.3.1. Catalytic tests

Table 4.10 summarizes the results obtained for the oxidation of Benzyl alcohol to benzaldehyde in toluene at 90ºC and atmospheric pressure of pure oxygen O_2 over the Ru catalysts prepared from different precursors and over different support materials. Traces amounts of products were observed in blank tests carried out without catalyst (entry 1) and with the bare graphenic supports (entry 2 and 3).

Table 4.10 Characteristics and catalytic performance of the Ru catalysts in the oxidation of benzyl alcohol

Entry	Catalyst	Conversion (%)	Sel Benzaldehyde (%)
1	Blank	0.4	>99
2	rGO	0.3	>99
3	NrGO	0.3	>99
4	Ru(Cl)/rGO	14	>99
5	Ru(Cl)/NrGO	16	>99
6	Ru(NN)/rGO	31	>99
7	Ru(NN)/NrGO	32	>99
8	Ru(CO)/rGO	36	>99
9	Ru(CO)/NrGO	46	>99
10	Ru(CO)/AC	16	>99
11	Ru(CO)/HSAG	18	>99

Reaction conditions: Benzyl alcohol, 8.4 mmol, 25 mg of catalyst, molar ratio Substrate/M=849, toluene 10 ml, O_2 5ml min^{-1}, 90ºC, 24 hours. Reduction temperature 350ºC.

From Table 4.10 it can be seen that the achieved benzaldehyde selectivities, for all the studied Ru catalysts, were higher than 99%. Interestingly, all the Ru catalysts supported on NrGO systematically produce higher conversion in comparison with those supported on rGO (Table 4.10 and Figure 4.35). The most noteworthy remark from these comparative data is that, with the catalyst derived from $Ru_3(CO)_{12}$ supported on NrGO, conversions of 46% with >99% selectivity towards benzaldehyde were reached after 24 hours. The same tendency is observed using Ru(NN)/NrGO, (entry 7) compared to Ru(NN)/rGO (entry 6). The activities obtained with catalysts prepared from ex-chloride precursors (entries 4 and 5) were lower than the activity observed using a $Ru_3(CO)_{12}$ and $Ru(NO)(NO_3)_3$ derived catalysts. As discussed above, the presence of residual chlorine on the surface of the Ru(Cl)/rGO catalyst was detected by XPS. Chlorine atoms poison Ru nanoparticles, reducing the number of active sites. For Ru(CO)/AC and Ru(CO)/HSAG catalysts the poor catalytic activities can be attributed to the differences in Ru average particle sizes (2.3-2.4 nm Table 4.3) compared with the Ru(CO)/NrGO catalyst (1.8 nm Table 4.3). Undoubtedly, the support plays a key role in the performance of the studied Ru catalysts and among the examined supports NrGO is the most preferable for the oxidation of benzyl alcohol.

The outstanding catalytic performances of Ru(CO)/NrGO could be associated with an electron enrichment of the Ru nanoparticles, revealed by XPS measurements (section 4.2). On the other hand, the nature of the nitrogen groups in the surface of NrGO, in the case of Ru catalysts supported on NrGO, surely may contribute to the reaction in cooperative action with the Ru nanoparticles. It well known that organic compounds are able to originate specific interactions depending on their polarities, when they interact with the diverse types of groups exposed on the surface of graphenic materials. Since nitrogen adatoms have an additional electron in comparison with carbon atoms, p electron delocalization will occur easily in NrGO, in short, changing the electron density of the graphenic materials. This excess of electrons changes the π-π interactions between the graphenic surfaces and the substrate, and possibly modifies the adsorption of reactants over the support, near the catalytic sites. Furthermore N groups can enhance the interactions between the NrGO surface and acid molecules, such as dipole–dipole, or hydrogen bonding[108] favouring the desorption of the reaction products from catalytic active sites. Thus, acidity of benzyl alcohol (pka 15.4) and more notably, acidity of benzaldehyde (pka 14.9) could be important because of the possibility of formation of donor-acceptor complexes with the delocalized p electrons of NrGO. In a similar way to oxidation of 5-HMF (Section 4.3.1), the production of benzaldehyde starts after the chemisorptions of reactants and oxygen on the Ru surface. Then, benzaldehyde is efficiently removed from the metallic surface, with the help of the basic sites exposed on the graphenic materials, and consequently the catalytic activity is enhanced, as reported for Ru(CO)/NrGO catalyst compared to rGO supported Ru NPs in Figure 4.35.
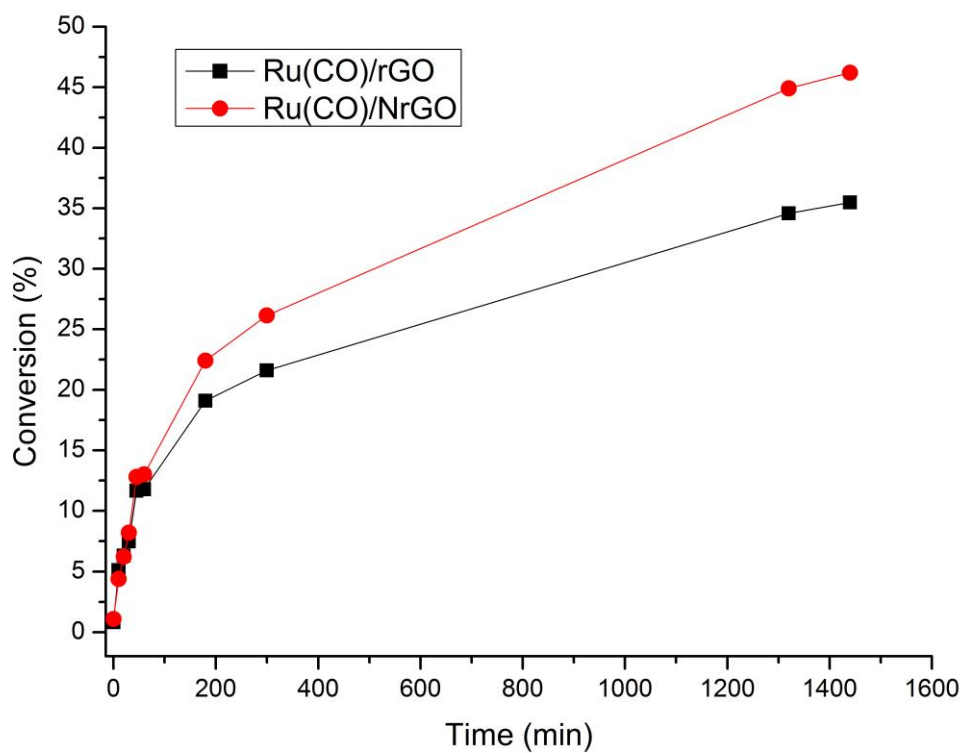
Figure 4.35 Conversion of benzyl alcohol into benzaldehyde over Ru(CO)/rGO and Ru(CO)/NrGO reduced at 350ºC. Reaction conditions: Benzyl alcohol, 8.4 mmol, 25 mg of catalyst, molar ratio Substrate/M=849, toluene 10 ml, O_2 5ml min^{-1}, 90ºC, 24 hours.

A comparative evaluation between the results obtained using Ru(CO)/NrGO as catalyst with those previously published is summarized in Table 4.11. It should be notice that in all reactions presented in Table 4.11, any additive was used in the reaction media. The comparison among catalysts in Table 4.11 is not easy since the reaction conditions are not similar. However, considering that this work was developed using Ru as metal and higher molar reactant-metal ratio, the performance of N doped graphene material supported Ru catalysts is clearly more effective compared to those reported in the literature.

Table 4.11 Comparative data of the Benzyl alcohol oxidation over different metal supported catalysts

Catalyst	Benzyl alcohol:Metal ratio	T (°C)	O_2 flow (ml min^{-1})	Time (h)	Conv (%)	Sel (%)	Ref
2%Au/U_3O_8[a]	713	130	1.5 bar	5	53	95	[99]
3%Pd/MagSBA[a]	3429	90	1 bar	9	81	83	[100]
8.7% Pd/N-CNT[a]	2975	120	20	3	91	>99	[102]
1%Pt /TiO_2[b]	39	26	Ambient air	10	77	>99	[104]
1.4%Ru/Al_2O_3[c]	70	83	1 bar	1	>99	>99	[49]
9.3% RuO_2 /CN[d]	14	80	6	1	75	>99	[105]
9.2% RuO_2 /NaY[d]	108	70	20	3	12	>99	[106]
4% Ru(CO)/NrGO[d]	849	90	5	24	46	>99	This work

[a]Solventless [b]Solvent water [c]Solvent trifluorotoluene [d]Solvent toluene

4.3.3.2. Stability tests

Based on the above catalytic results, we have subsequently examined the reusability of Ru(CO)/NrGO catalyst, after reduction treatment at 350ºC. Three successive rounds were conducted with the solid recovered by filtration and washed thoroughly with toluene. As shown in Figure 4.36 the achieved conversion of benzyl alcohol strongly decreased during the recycling experiments, but no loss in the selectivity towards benzaldehyde was observed. Therefore, a clear reduction in the intrinsic activity was observed for the Ru (CO)/NrGO catalyst.
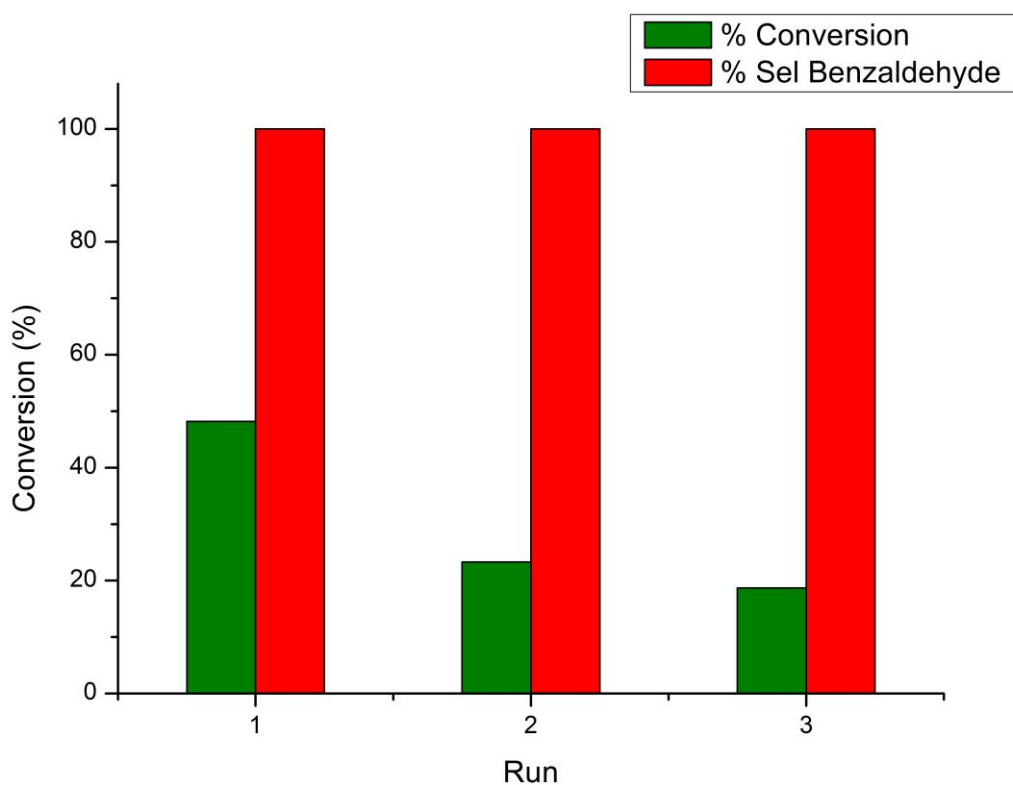
Figure 4.36 Stability of the Ru(CO)/NrGO catalysts during the recycling uses for the oxidation of benzyl alcohol. Reaction conditions: benzyl alcohol 8.4 mmol, 25 mg of catalyst, molar ratio Substrate/M=849, toluene 10 ml, O_2 5ml min^{-1}, 90ºC, 24 hours.

181

In order to elucidate the causes of this deactivation a series of complementary experiments were carried out. So, the potential leached ruthenium was extracted from the filtered toluene solution using 3 portions of 10 ml of water and its concentration was determined by ICP-EOS. For the solutions obtained from the Ru(CO)/NrGO catalysts after the recycling experiments, no detectable leaching of ruthenium was identified. To preclude a loss of activity produced by a Ru sintering mechanism, the spent catalyst was studied by TEM. The average diameters for fresh (Table 4.3) and spent catalyst (Table 4.12 and Figure 4.37) were 1.8nm and 1.4nm, respectively. Thus, no essential changes in the particle size distribution after the recycling experiment were detected.
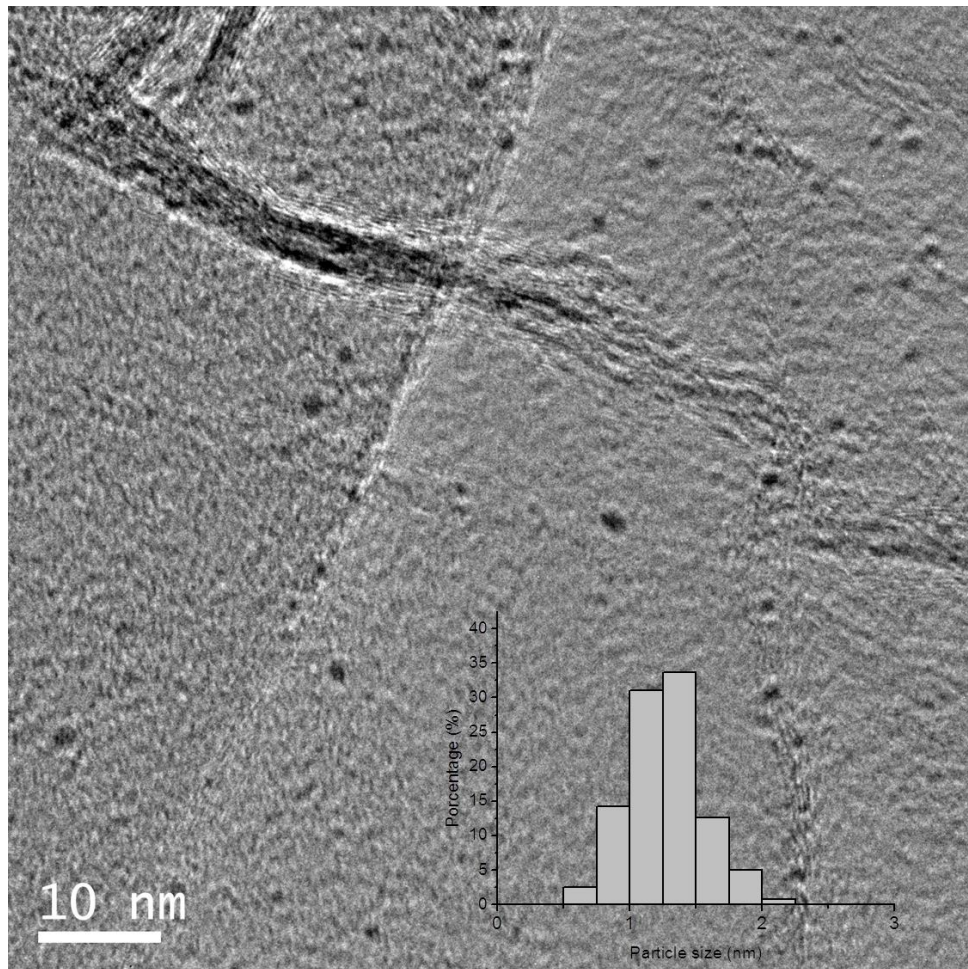
Figure 4.37 TEM image and particle size distribution for spent Ru (CO)/NrGO

Finally the fresh and the spend catalysts were analysed by X-ray photoelectron spectroscopy (XPS) using a Kratos AXIS Supra spectrophotometer, which operated with a monochromatic Al K_α source (1486.7 eV). This study was performed in order to evaluate a possible change in the oxidation state of the Ru nanoparticles. The Ru 3p XPS spectra of the fresh samples contain a doublet which can be assigned to Ru^0 species.[203] The XPS spectra for the spent samples upon recycling did not show any significant shift in the position of the peaks corresponding to Ru 3p (Table 4.12 and Figure 4.38). Hence, changes in the Ru oxidation states before and after reaction could not be assigned as main contributions to the deactivation of the active sites.

Table 4.12 XPS data of fresh Ru(CO)/NrGO and spent Ru(CO)/NrGO catalysts.

Catalyst	d_{TEM}(nm)	BE Ru $3p_{3/2}$ (eV)	FWHM	Ru/C
Ru(CO)/NrGO fresh	1.8	463.0	3.5	0.004
Ru(CO)/NrGO spent	1.4	463.0	3.7	0.004
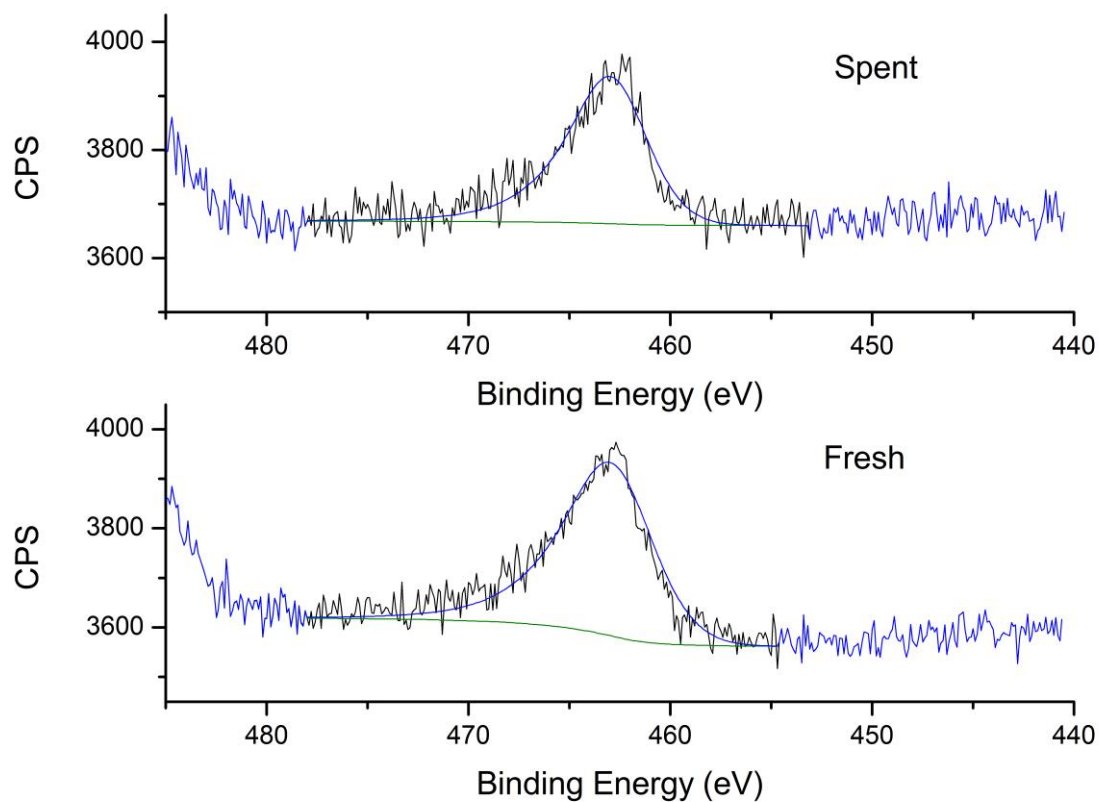
Figure 4.38 XPS spectra of 3p3/2 region for fresh Ru(CO)/NrGO and spent Ru(CO)/NrGO catalysts

Taken together, these results demonstrate that the sintering of Ru nanoparticles, the oxidation of Ru species, and the leaching of ruthenium could be discarded as possible explanations for the decrease in the activity of the Ru catalysts.

In order to attempt to figure out the causes of the catalyst deactivation a series of treatment experiments was carried out. In an earlier work Yu et al.[105] demonstrated that the water, formed as product of the reaction during the oxidation of benzyl alcohol may adsorb over the active sites of Ru catalysts restricting the adsorption of the reactants and blocking the accessibility to these metallic surface sites. Reasonably this effect of deactivation may occur due to the low solubility of water in weakly polar solvents, as toluene. Considering this later study, we have applied treatments to the used Ru(CO)/NrGO catalyst oriented to remove adsorbed water. Thus, the recyclability of the catalysts was investigated, under the same reaction conditions, after a drying treatment of the spent catalyst under helium flow at 300ºC. In fact after this regeneration treatment catalyst activity is re-established. So conversions of benzyl alcohol after 3 rounds slightly decreased, as shown in Figure 4.39. Also the selectivity to benzaldehyde kept stable during the recycling process. This indicates that Ru(CO)/NrGO catalyst was generally stable showing a minor deactivation during the recycling experiment. Consequently, drying treatment of Ru(CO)/NrGO, between successive reaction runs, allows the reuse of this catalyst. Finally, the slight deactivation, observed in Figure 4.39, could be related to a small loss of mass during recovery of the Ru(CO)/NrGO catalyst between successive runs. But the relevant finding is that, these results prove that the highly active Ru(CO)/NrGO catalyst shows excellent reusability under the employed reaction conditions, without significant loss of catalytic activity or selectivity after a simple post reaction treatment.
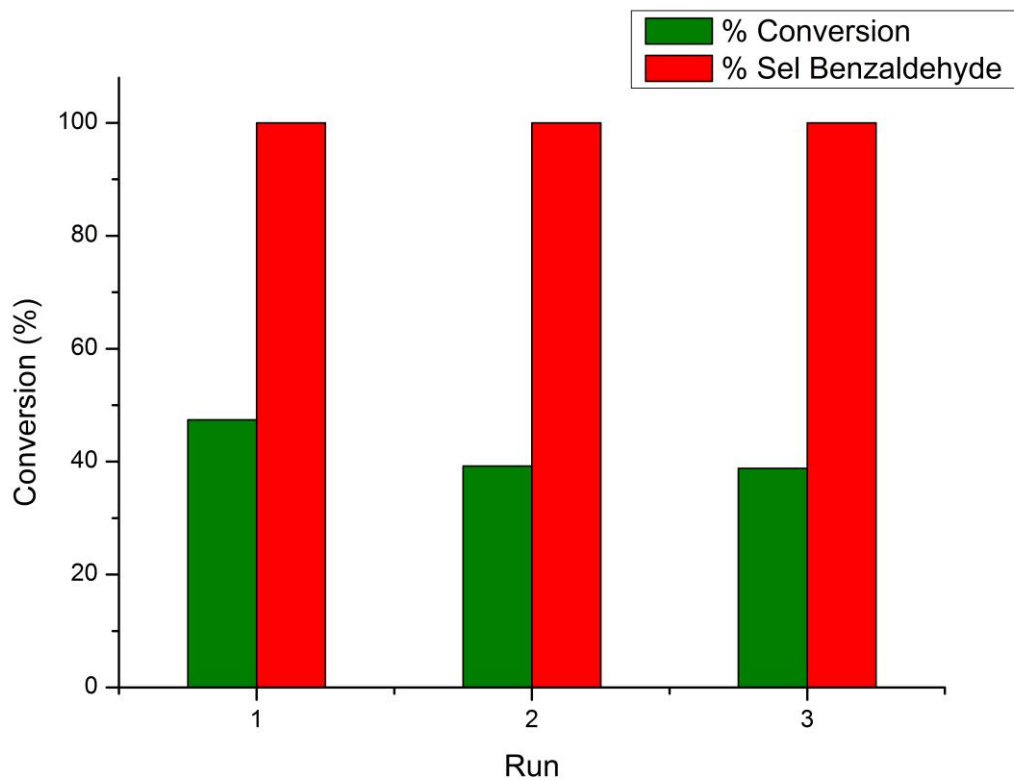
Figure 4.39 Stability of the Ru(CO)/NrGO catalysts during the recycling uses for the oxidation of benzyl alcohol after thermal reactivation treatments between runs. Reaction conditions: benzyl alcohol 8.4 mmol, 25 mg of catalyst, molar ratio Substrate/M=849, toluene 10 ml, O$_2$ 5ml min^{-1}, 90°C, 24 hours.

CONCLUSIONS-CONCLUSIONES

5. CONCLUSIONS - CONCLUSIONES

CONCLUSIONS

The objective of this Doctoral Thesis is to develop new nanomaterials based on N-doped and non-doped graphenic materials with tailored and optimized properties. In addition, these materials are utilized as support of Ru nanoparticles. The aim is to establish and comprehend the effects induced by the supports when metal particles are deposited on them. Likewise, the common axis of all this research is the application of the synthesized materials as heterogeneous catalysts in several reactions of valorisation of some platform molecules obtained from biomass. And more precisely, to establish the effects induced by the properties of the supports on the Ru particles when they act as catalysts (activity, selectivity, stability)

The purpose of this final chapter is to present the more relevant conclusions obtained. For this, it will proceed following the same scheme in which the results have been presented and discussed

Synthesis and characterization of graphenic materials and catalysts:

A successful and reproducible method for the synthesis of graphenic materials and nitrogen doped graphene derivatives with controlled properties has been reported. It was based on the oxidation of graphite flakes with different particle sizes and selecting the used experimental conditions during the later thermal exfoliation process. The conclusions of this section are in more detail:

1)   Analysis and characterization data pointed out that the physical properties of the graphenic materials, such as the nitrogen species introduced and the surface area obtained, were dependent on the particle size of the starting graphite and the experimental conditions during the thermal exfoliation. This study allowed to synthesize new graphenic materials with controlled properties: quantity and type of the nitrogen functionalities incorporated, number of graphitic layers in the resulting material, or surface area developed during the thermal exfoliation process. These results show that it is possible to control the final properties of graphenic materials and their doping with nitrogen atoms, replacing carbon atoms in the structure.

2)   The results point out that smaller particle sizes lead to higher surface areas. We achieved surface areas of 870 m^2g^{-1} for rGO. While for NrGO samples obtained we observed BET surface areas close to 500 m^2g^{-1}. For these last ones the amount of nitrogen introduced could be also tailored

3)   By introducing nitrogen within the graphenic structure, the electronic properties and basicity of the doped materials are modified. Due to these modifications in the properties of the optimized NrGO and rGO samples, they can be used as part of promising catalytic materials consisting of Ru metal nanoparticles supported on them, with better catalytic properties: more active, more selective and more stable.

4)   It is well know that high surface area supports favor deposition of the precursor leading to well dispersed nanoparticles. Thus, over the optimized developed materials were supported Ru NPs, generally of sizes smaller than 5 nm, and in many cases showing average diameters of the order of 1-2 nm. These size values of the Ru NPs refer to pre-reduced samples at temperatures of the order of 300-400°C, which in some way ensures their stability at the reaction temperatures in which they can be applied.

5)   Different Ru precursors have also been studied for the preparation of catalytic materials. It was found that rutheniun dodecacarbonyl precursor $Ru_3(CO)_{12}$ gives smaller particle sizes. As a general rule, when a graphenic support is considered, the ruthenium particle size change with the metal precursor in the order: $Ru(Cl) > Ru(NN) \sim Ru(CO)$.

6) The XPS spectra of the Ru 3p transition have been comparatively analyzed for all the catalysts prepared from the three Ru precursors, and supported in both nitrogen-doped and undoped graphene materials. Systematically, it was found that when the Ru NPs are supported over the nitrogen-doped graphenic material, they suffer a shift in the Ru binding energies towards lower energy values when compared with rGO supported catalysts. The results reveal that the incorporation of nitrogen atoms in the graphitic structure of graphene could favor donation of electron density towards Ru active sites. Therefore, a new type of electronic interaction has been identified between the supports, either functionalized or not, and Ru particles. This interaction is clearly an electron transfer interaction from the support to the metal containing the catalytically active sites; hence it is relevant to compare these materials from the point of view of their action in various reactions.

Application as heterogeneous catalysts:

The materials composed by Ru NPs supported on the optimized graphenic supports have been evaluated in three processes that use platform molecules as substrates; that is, compounds obtained from biomass and that serve as a starting point to obtain other chemical products of greater industrial interest.

When it has been considered appropriate, other series of catalysts have been prepared and characterized to compare them, in terms of their catalytic behaviour, with the Ru-graphenic materials. The obtained results have also been compared with those published in the bibliography.

The reactions that have been studied are:

✓ The base free aqueous-phase oxidation of 5-hydroxymethylfurfural (5-HMF) to 2,5-Furandicarboxylic acid. (FDCA)

✓ The aqueous-phase hydrogenation of furfural (FAL) to furfuryl alcohol (FOL).

✓ The selective oxidation of benzyl alcohol to benzaldehyde.

The conclusions derived from each of the three reactions are listed bellow

1) The obtained results in the aqueous-phase aerobic oxidation of 5-HMF showed that the support along with the Ru precursor remarkably affect the conversion and product distributions for this reaction. In addition, the catalysts supported on graphenic materials are more active and selective, compared to those supported in other commercial carbonaceous materials.

2) For graphenic supported catalysts the highest conversion in the oxidation of 5-HMF was achieved by using $Ru_3(CO)_{12}$ as ruthenium precursor. For the improved catalyst, Ru supported on NrGO, yield towards FDCA close to 80% was achieved. Characterization data pointed out those catalytic results can be correlated to basic properties of NrGO support as well as to the surface properties of Ru nanoparticles. Thus, it was proposed that basic surface nitrogen heteroatoms exposed on the NrGO support can play an important role, particularly in the desired product selectivity. Due to their basic character, the surface nitrogen sites exposed on the doped graphene surface can remove the acidic products of this reaction cooperating with the maintenance of free surface Ru sites to perform the oxidation reaction more rapidly.

3)   Finally, for the oxidation of 5-HMF, it has been proven that the best catalyst in terms of yield was the one prepared using Ru dodecacarbonyl as precursor and NrGO. Ru(CO)/NrGO catalyst can be reused several times without any significant loss of activity nor modifications in selectivity values.

4)   Regarding the catalytic hydrogenation of FAL into FOL, the results obtained confirm that the performance of the Ru based catalysts is strongly influenced by the reduction temperature and the used ruthenium precursor; and to a lesser degree by the support. . In relation to N doped graphenic materials used as support, the functions related to nitrogen groups do not seem to be positively involved in the improvement of the catalytic behavior. The characterization results pointed out that not only smaller Ru particle sizes lead to higher catalytic activities and selectivities, but also the special surface properties of graphenic materials have a major contribution in the improvement of the catalytic features. Thus, the inert surface of this rGO support favours an efficient hydrogenation of FAL by Ru, because rGO offers a large specific surface area, allowing that an accelerated diffusion of reactant and product in its surface. Thus, once furfuryl alcohols is formed on the surface of catalyst, they would leave quickly and then be replaced by new reactant molecules.

5)   Thus, the best results in the hydrogenation of FAL were obtained over the sample Ru(CO)/rGO (93% conversion and 98% of selectivity toward FOL). It was demonstrated that Ru(CO)/rGO can be reused several time in the reaction process without further reactivation or regeneration treatments. Thus, a remarkable stable catalyst for the hydrogenation of FAL has been reported, being superior to the ones reported in the bibliography.

6)   It must be remembered that, unlike the previous reactions, the selective oxidation of benzyl alcohol to benzaldehyde is not carried out in aqueous medium, but in toluene as solvent. The different supports also strongly modify the catalytic behaviour of Ru nanoparticles, the NrGO materials being those that under the experimental reaction conditions used produce the highest conversion of benzyl alcohol to the desired product. Thus, the catalytic performance is significantly enhanced by presence of N in the graphenic structure. These catalytic differences could be attributed to the interaction of the substrate and products of the reaction with the surface of N doped graphenic materials due to their weak acidity.

7)   Moreover, metal precursor also plays an important role on the activity of the catalysts in oxidation of benzyl alcohol. The best results were obtained over the sample Ru(CO)/NrGO showing conversions close to 50% and >99% of selectivity toward benzaldehyde. It was found that the catalyst strongly deactivated during the reaction probably due to water accumulation on the active sites. It was proved that the surface of the spent catalyst can be easily regenerated with a simple drying treatment.

CONCLUSIONES

El objetivo principal de esta Tesis Doctoral es desarrollar nuevos nanomateriales basados en materiales grafénicos dopados con nitrógeno y sin dopar, con propiedades superficiales optimizadas convenientemente. Además dichos materiales son aplicados como soporte de nanopartículas de Ru. La idea es poder establecer y comprender los efectos inducidos por dichos soportes cuando se depositan sobre ellos partículas metálicas. Igualmente, como eje común de toda esta investigación, está utilizar los materiales sintetizados como catalizadores heterogéneos en varias reacciones de valorización de algunas moléculas plataforma obtenidas a partir de la biomasa. Y más concretamente establecer los efectos generados por las propiedades de los soportes sobre las partículas de Ru cuando actúan como catalizadores (actividad, selectividad, estabilidad).

El objetivo de este último capítulo final es presentar las conclusiones más relevantes que se han obtenido. Para ello, se procederá siguiendo el mismo esquema con el que se han presentado y discutido los resultados.

Síntesis y caracterización de materiales grafénicos y de catalizadores:

Se ha demostrado que es posible conseguir un método reproducible para la síntesis de materiales grafénicos y de sus derivados dopados con grupos de nitrógeno. En ambos casos se han podido controlar las propiedades superficiales que los caracterizan. Dicho método se basa en la oxidación de granos de grafito, con diferentes tamaños de partículas, y en la selección de las condiciones experimentales adecuadas para realizar los subsiguientes tratamientos de exfoliación térmica. Con más detalle las conclusiones de este apartado son:

1) Los datos de análisis y caracterización de las propiedades físicas de los materiales soporte, como son las especies de nitrógeno introducidas o los valores de áreas superficiales conseguidos, resultan depender del tamaño de grano del grafito de partida; así como de las condiciones experimentales usadas en la exfoliación térmica. Este estudio nos ha permitido sintetizar nuevos materiales grafénicos con propiedades controladas: cantidad y tipo de las funcionalidades de nitrógeno incorporadas en los materiales grafénicos, número de capas grafíticas en el material resultante o el área superficial que desarrollan durante el proceso de exfoliación térmica. Estos resultados demuestran que es posible controlar las propiedades finales de los materiales grafénicos y de su dopado con átomos de nitrógeno, sustituyendo a otros átomos de carbono de la estructura.

2) Los tamaños de grano más pequeños en el grafito de partida dan lugar a materiales grafénicos con áreas superficiales mayores. Así hemos logrado materiales con áreas superficiales del orden de 870 m^2g^{-1}, para las muestras que no tienen nitrógeno incorporado, mientras que hemos llegado a acercarnos a los 500 m^2g^{-1} en las muestras dopadas. También el contenido de nitrógeno puede ser modulado mediante los procesos de síntesis.

3)   Al incorporar el nitrógeno dentro de la estructura grafénica, se modifican las propiedades electrónicas y la basicidad de los materiales resultantes. Debido a estas modificaciones en las propiedades del soporte se pueden conseguir materiales catalíticos, consistentes en nanopartículas metálicas de Ru soportadas en ellos, con mejores propiedades catalíticas: más activos, más selectivos o más estables.

4)   Es bien sabido que las altas áreas superficiales en los soportes favorecen el anclaje de los precursores metálicos, con lo que se generan nanopartículas catalíticas bien dispersas. Por lo tanto, sobre los materiales que hemos desarrollado, ha sido posible soportar nanopartículas de Ru generalmente de tamaños menores de 5 nm, y en muchos casos diámetros promedio del orden de 1-2 nm. Estos valores de tamaño de las nanopartículas de Ru se refieren a muestras pre-reducidas a temperaturas del orden de los 300-400 ºC, lo que en cierta forma asegura su estabilidad a las temperaturas de reacción en las que pueden aplicarse.

5)   También se han estudiado diferentes precursores de Ru para la preparación de los materiales catalíticos, encontrándose que el trirutenio dodecacarbonilo [$Ru_3(CO)_{12}$] es el que da lugar a los tamaños de partícula más pequeños. Como regla general para los catalizadores de Ru soportados en los materiales grafénicos, el tamaño de las partículas de Ru que se obtienen, según el precursor, sigue el orden: cloruro > nitrato de nitrosilo ~ carbonilo.

6)   Los espectros XPS de la transición Ru 3p se han analizado comparativamente, en todos los catalizadores preparados a partir de los tres precursores de Ru, y tanto soportados en los materiales grafénicos dopados con nitrógeno como en los sin dopar. Sistemáticamente se ha observado que cuando las nanopartículas de Ru están soportadas sobre el material grafénico dopado con nitrógeno, las energías de ligadura son menores que cuando se soportan en material grafénico exento de nitrógeno. Estos resultados apuntan a que la incorporación de átomos de nitrógeno en las estructuras grafíticas del soporte puede favorecer la donación de densidad de electrones, hacia los sitios activos de Ru. Por tanto, se ha identificado un nuevo tipo de interacción electrónica entre este tipo de soportes, funcionalizados o no, y las partículas de Ru. Dicha interacción es claramente de transferencia de electrones entre el soporte y el metal que contiene los sitios catalíticamente activos, por consiguiente resulta relevante comparar estos materiales desde el punto de vista de su acción en diversas reacciones.

Aplicación como catalizadores heterogéneos:

Los materiales consistentes en nanopartículas de Ru soportadas en los materiales grafénicos optimizados, se han evaluado en tres procesos que usan como reactivos moléculas plataforma; es decir, compuestos obtenidos a partir de biomasa y que sirven como punto de partida para obtener otros productos químicos de mayor interés industrial. Cuando se ha considerado oportuno se han preparado y caracterizado otras series de catalizadores para compararlos, en cuanto a sus comportamientos como catalizadores, con los materiales Ru-material grafénico. Igualmente se han comparado los resultados obtenidos con los publicados en la bibliografía.

Las tres reacciones que se han estudiado son:

- ✓ La oxidación en fase acuosa y sin adición de bases del 5-hidroximetilfurfural (5-HMF) a ácido 2,5-furandicarboxílico (FDCA).

- ✓ La hidrogenación en fase acuosa del furfural (FAL) al alcohol furfurílico (FOL).

- ✓ La oxidación selectiva de alcohol bencílico a benzaldehído.

Las conclusiones derivadas del estudio de la acción catalítica en cada una de las tres reacciones se enumeran a continuación.

1) Los resultados obtenidos en la oxidación aeróbica en fase acuosa de 5-HMF demuestran que, tanto el soporte como el precursor de Ru, afectan significativamente las conversiones y selectividades obtenidas en esta reacción. Además, los catalizadores soportados en materiales grafénicos son más activos y selectivos, en comparación a cuando el Ru esta soportado en otros materiales carbonosos comerciales.

2) También en la oxidación del 5-HMF, en particular utilizando aquellos catalizadores soportados en los materiales grafénicos, y sobre todo en el preparado a partir de $Ru_3(CO)_{12}$, se ha conseguido maximizar el rendimiento hacia FDCA, llegando a valores cercanos al 80%. Los resultados de la caracterización llevan a pensar que los resultados catalíticos se pueden correlacionar con las propiedades básicas del soporte de NrGO, así como con las propiedades de superficie de las nanopartículas de Ru. Por ello, se ha propuesto que los heteroátomos de nitrógeno de carácter básico, expuestos en la superficie del soporte, intervienen en la reacción y modifican la selectividad. Debido su carácter básico, los grupos superficiales de nitrógeno actúan retirando los productos de la reacción de carácter ácido, permitiendo que los sitios catalíticamente activos de Ru permanezcan libres de productos de re-adsorción y la reacción ocurra más rápidamente.

3) Por último, en la reacción de oxidación del 5-HMF, se ha comprobado que el mejor catalizador en términos de rendimiento es el preparado a partir de dodecacarbonilo de Ru y NrGO. El catalizador Ru(CO)/NrGO puede ser reutilizado varias veces sin pérdida significativa de su actividad catalítica, y sin modificaciones en los valores de selectividad conseguidos.

4)   En relación con la hidrogenación en fase acuosa del furfural al alcohol furfurílico (FOL) los resultados obtenidos confirman que el rendimiento de los catalizadores basados en Ru está fuertemente influenciado por la temperatura de reducción y el precursor de rutenio usado en la preparación; y en menor extensión por el material soporte. En cuanto a los materiales grafénicos dopados con N utilizados como soporte, las funciones relacionadas con los grupos de nitrógeno no parecen estar implicadas positivamente en la mejora del comportamiento catalítico. Los resultados de caracterización señalaron que no solo los tamaños de partícula de Ru más pequeñas conducen a actividades y selectividades catalíticas más elevadas, sino que las propiedades superficiales especiales de los materiales grafénicos podrían tener una importante contribución en la mejora de las propiedades catalíticas. Así, la superficie inerte del rGO favorece una hidrogenación eficiente de FAL por Ru, porque ofrece una gran superficie específica, lo que permite una difusión acelerada de reactivo y producto en su superficie. Por lo tanto, una vez que el FOL se forma en la superficie del catalizador, es removido rápidamente y es reemplazado por nuevas moléculas de reactivo.

5)   Igualmente en la reacción de la hidrogenación en fase acuosa del furfural los mejores resultados catalíticos se obtuvieron usando el material preparado con carbonilo de Ru, soportado sobre el material grafénico no dopado, muestra designada como Ru(CO)/rGO, llegando a valores de conversión del 93% y a selectividad hacia FOL del 98%. Sobre este mismo catalizador se verificó que se puede reutilizar varias veces en reacción, sin requerir tratamientos de reactivación o regeneración adicionales. Estos aspectos hacen que este catalizador aplicado para esta reacción sea remarcable, en el sentido de ser superior a los datos reportados en la bibliografía.

6)   Conviene recordar que, a diferencia de las anteriores, la oxidación selectiva de alcohol bencílico a benzaldehído no se realiza en medio acuoso, sino en tolueno como disolvente. También aquí los diferentes soportes modifican fuertemente el comportamiento catalítico de las nanopartículas de Ru, siendo los materiales de NrGO los que bajo las condiciones de reacción experimentales utilizadas producen la conversión más alta de alcohol bencílico al producto deseado. Por lo tanto, el rendimiento catalítico se mejora significativamente por la presencia de N en la estructura grafénica del soporte. Tentativamente estas diferencias catalíticas se pueden atribuir a la interacción del sustrato y el producto de la reacción con la superficie de materiales grafénicos dopados con N, debido a su carácter de acidez débil.

7)   Asimismo se ha demostrado, en la oxidación selectiva de alcohol bencílico a benzaldehído, que el precursor de Ru metal también es importante desde el punto de vista de la actividad catalítica. De nuevo los mejores resultados se obtuvieron usando la muestra Ru(CO)/NrGO, llegándose a conversiones cercanas al 50% y selectividades hacia benzaldehído mayores del 99%. Por otra parte se comprobó que este catalizador se desactivaba fuertemente durante esta reacción, impidiendo su reúso. Las causas de esta desactivación posiblemente estén ligadas a la acumulación de agua cerca de los sitios activos. Por ello, se probó que la actividad del catalizador agotado puede regenerarse, mediante un simple tratamiento de secado.

BIBLIOGRAFIA

6. BIBLIOGRAFIA

(1)   Yan, K.; Jarvis, C.; Gu, J.; Yan, Y. *Renew. Sustain. Energy Rev.* **2015**, *51*, 986–997.

(2)   Chheda, J. N.; Huber, G. W.; Dumesic, J. A. *Angew. Chemie - Int. Ed.* **2007**, *46* (38), 7164–7183.

(3)   Shafiee, S.; Topal, E. *Energy Policy* **2009**, *37* (1), 181–189.

(4)   Van Putten, R. J.; Van Der Waal, J. C.; De Jong, E.; Rasrendra, C. B.; Heeres, H. J.; De Vries, J. G. *Chem. Rev.* **2013**, *113* (3), 1499–1597.

(5)   Wu, L.; Moteki, T.; Gokhale, A. A.; Flaherty, D. W.; Toste, F. D. *Chem* **2016**, *1* (1), 32–58.

(6)   Huber, G. W.; Iborra, S.; Corma, A. *Chem. Rev.* **2006**, *106* (9), 4044–4098.

(7)   Azar, C.; Lindgren, K.; Larson, E.; Möllersten, K. *Clim. Change* **2006**, *74* (1–3), 47–79.

(8)   Reed, T.; Das, A. *Handbook of Biomass Downdraft Gasifier Engine Systems*; Biomass Energy Foundation Press, 1988.

(9)   Alonso, D. M.; Bond, J. Q.; Dumesic, J. A. *Green Chem.* **2010**, *12* (9), 1493.

(10)   Besson, M.; Gallezot, P.; Pinel, C. *Chem. Rev.* **2014**, *114* (3), 1827–1870.

(11)   Lin, Y.; Huber, G. W. *Energy Environ. Sci.* **2009**, *2* (1), 68.

(12)   Li, X.; Jia, P.; Wang, T. *ACS Catal.* **2016**, acscatal.6b01838.

(13)   *Selective Catalysis for Renewable Feedstocks and Chemicals*; Nicholas, K. M., Ed.; Springer, 2014.

(14)   Climent, M. J.; Corma, A.; Iborra, S. *Green Chem.* **2014**, *16* (2), 516–547.

(15)   Sebayang, A. H.; Masjuki, H. H.; Ong, H. C.; Dharma, S.; Silitonga, A. S.; Mahlia, T. M. I.; Aditiya, H. B. *RSC Adv.* **2016**, *6* (18), 14964–14992.

(16)   Vennestrøm, P. N. R.; Osmundsen, C. M.; Christensen, C. H.; Taarning, E. *Angew. Chemie Int. Ed.* **2011**, *50* (45), 10502–10509.

(17)   Yan, K.; Yang, Y.; Chai, J.; Lu, Y. *Appl. Catal. B Environ.* **2015**, *179*, 292–304.

(18)   Bozell, J. J.; Petersen, G. R. *Green Chem.* **2010**, *12* (4), 539.

(19) Werpy, T.; Petersen, G. *Top Value Added Chemicals from Biomass*; 2004; Vol. 1.

(20) Resasco, D. E.; Sitthisa, S.; Faria, J.; Prasomsri, T.; Ruiz, M. P. In *Heterogeneous Catalysis in Biomass to Chemicals and Fuels*; 2011; pp 1–33.

(21) Mukherjee, A.; Dumont, M.-J.; Raghavan, V. *Biomass and Bioenergy* **2015**, *72*, 143–183.

(22) Rosatella, A. A.; Simeonov, S. P.; Frade, R. F. M.; Afonso, C. A. M. *Green Chem.* **2011**, *13* (4), 754.

(23) Gebre, H.; Fisha, K.; Kindeya, T.; Gebremichal, T. *Int. Lett. Chem. Phys. Astron.* **2015**, *57*, 72–84.

(24) Zeitsch, K. J. In *The chemistry and technology of furfural and its many by-products*; Elsevier, 2000; Vol. 13, pp 36–74.

(25) Bull, S. R. *Renewabe Energy* **1994**, *5*, 799–806.

(26) Pugh, S.; McKenna, R.; Halloum, I.; Nielsen, D. R. *Metab. Eng. Commun.* **2015**, *2*, 39–45.

(27) Mabena, L. F. Synthesis , characterisation and activity of Ruthenium/N-doped multi-walled Carbon nanotubes catalysts, University of the Witwatersrand, 2013.

(28) Sheldon, R. A. *Green Chem.* **2014**, *16* (3), 950–963.

(29) Miura, T.; Kakinuma, H.; Kawano, T.; Matsuhisa, H. Method for producing furan-2,5-dicarboxylic acid. US7411078B2, 2008.

(30) Partenheimer, W.; Grushin, V. V. *Adv- Synth. Catal.* **2001**, *343* (1), 102–111.

(31) Zhang, Z.; Deng, K. *ACS Catal.* **2015**, *5* (11), 6529–6544.

(32) Vinke, P.; Van Dam, H. E.; Van Bekkum, H. *Stud. Surf. Sci. Catal.* **1990**, *55* (8), 147–158.

(33) Lilga, M. a; Hallen, R. T.; Gray, M. *Top. Catal.* **2010**, *53* (15–18), 1264–1269.

(34) Casanova, O.; Iborra, S.; Corma, A. *ChemSusChem* **2009**, *2* (12), 1138–1144.

(35) Donoeva, B.; Masoud, N.; de Jongh, P. E. *ACS Catal.* **2017**, No. Figure 1, acscatal.7b00829.

(36) Xie, J.; Nie, J.; Liu, H. *Chinese J. Catal.* **2014**, *35* (6), 937–944.

(37) Albonetti, S.; Lolli, A.; Morandi, V.; Migliori, A.; Lucarelli, C.; Cavani, F. *Appl. Catal. B Environ.* **2015**, *163*, 520–530.

(38) Neațu, F.; Marin, R. S.; Florea, M.; Petrea, N.; Pavel, O. D.; Pârvulescu, V. I. *Appl. Catal. B Environ.* **2016**, *180*, 751–757.

(39) Casanova, O.; Iborra, S.; Corma, A. *J. Catal.* **2009**, *265* (1), 109–116.

(40) Gupta, N. K.; Nishimura, S.; Takagaki, A.; Ebitani, K. *Green Chem.* **2011**, *13* (4), 824.

(41) Ardemani, L.; Cibin, G.; Dent, A. J.; Isaacs, M. A.; Kyriakou, G.; Lee, A. F.; Parlett, C. M. A.; Parry, S. A.; Wilson, K. *Chem. Sci.* **2015**, *6* (8), 4940–4945.

(42) Gorbanev, Y. Y.; Kegnæs, S.; Riisager, A. *Top. Catal.* **2011**, *54* (16–18), 1318–1324.

(43) Wan, X.; Zhou, C.; Chen, J.; Deng, W.; Zhang, Q.; Yang, Y.; Wang, Y. *ACS Catal.* **2014**, *4* (7), 2175–2185.

(44) Zhou, C.; Deng, W.; Wan, X.; Zhang, Q.; Yang, Y.; Wang, Y. *ChemCatChem* **2015**, *7* (18), 2853–2863.

(45) Lei, D.; Yu, K.; Li, M.-R.; Wang, Y.; Wang, Q.; Liu, T.; Liu, P.; Lou, L.-L.; Wang, G.; Liu, S. *ACS Catal.* **2016**, *7* (1), acscatal.6b02839.

(46) Yi, G.; Teong, S. P.; Zhang, Y. *Green Chem.* **2016**, *18* (4), 979–983.

(47) Davis, S. E.; Ide, M. S.; Davis, R. J. *Green Chem.* **2013**, *15* (1), 17–45.

(48) Kohsuke Mori; Takayoshi Hara; Tomoo Mizugaki; Kohki Ebitani, A.; Kaneda*, K. *JACS* **2004**, No. 126, 10657–10666.

(49) Yamaguchi, K.; Mizuno, N.; Zudin, V. N.; Zamaraev, K. I.; Nmr, S. S.; Laplaca, S. J.; Ibers, J. A.; Chem, I.; Yamaguchi, K.; Mizuno, N. *Angew. Chemie* **2002**, *41* (23), 4538–4542.

(50) Yang, X.; Xiuna, W.; Qiu, J. *Catal. Commun.* **2010**, *382*, 131–137.

(51) Zhu, J. U. Synthesis of Precious Metal Nanoparticles Supported on Bacterial Biomass for Catalytic Applications in Chemical Transformations, University of Birmingham, 2014.

(52) Sheldon, R. A.; Kochi, J. K. *Metal-Catalyzed Oxidations of Organic Compounds*; Academia Press: New York, 1981.

(53) Keresszegi, C.; Ferri, D.; Mallat, T.; Baiker, A. *J. Phys. Chem. B* **2005**, *109* (2), 958–967.

(54) Mallat, T.; Mallat, T.; Baiker, A.; Baiker, A. *Chem. Rev.* **2004**, *104* (6), 3037–3058.

(55) Mariscal, R.; Maireles-Torres, P.; Ojeda, M.; Sádaba, I.; López Granados, M. *Energy Environ. Sci.* **2016**, *9* (4), 1144–1189.

(56) Corma, A.; Iborra, S.; Velty, A. *Chem. Rev.* **2007**, *107*, 2411–2502.

(57) Chen, X.; Zhang, L.; Zhang, B.; Guo, X.; Mu, X. *Sci. Rep.* **2016**, *6* (1), 28558.

(58) Bremner, J.; Keeys, R. *J. Chem. Soc* **1947**, 1068–1080.

(59) Seo, G.; Chon, H. *J. Catal.* **1981**, *67* (2), 424–429.

(60) Rao, R.; Dandekar, A.; Baker, R. T. K.; Vannice, M. A. *J. Catal.* **1997**, *171* (2), 406–419.

(61) Kijeński, J.; Winiarek, P.; Paryjczak, T.; Lewicki, A.; Mikołajska, A. *Appl. Catal. A Gen.* **2002**, *233* (1), 171–182.

(62) Nagaraja, B. M.; Padmasri, A. H.; David Raju, B.; Rama Rao, K. S. *J. Mol. Catal. A Chem.* **2007**, *265* (1), 90–97.

(63) Baijun, L.; Lianhai, L.; Bingchun, W.; Tianxi, C.; Iwatani, K. *Appl. Catal. A Gen.* **1998**, *171* (1), 117–122.

(64) Chen, X.; Li, H.; Luo, H.; Qiao, M. *Appl. Catal. A Gen.* **2002**, *233* (1–2), 13–20.

(65) Taylor, M. J.; Durndell, L. J.; Isaacs, M. A.; Parlett, C. M. A.; Wilson, K.; Lee, A. F.; Kyriakou, G. *Appl. Catal. B Environ.* **2016**, *180*, 580–585.

(66) Panagiotopoulou, P.; Vlachos, D. G. *Appl. Catal. A Gen.* **2014**, *480*, 17–24.

(67) Zhang, Z.; Song, J.; Jiang, Z.; Meng, Q.; Zhang, P.; Han, B. *ChemCatChem* **2017**, *9* (13), 2448–2452.

(68) Zhao, Y. *Environ. Chem. Lett.* **2014**, *12* (1), 185–190.

(69) Nakagawa, Y.; Takada, K.; Tamura, M.; Tomishige, K. *ACS Catal.* **2014**, *4* (8), 2718–2726.

(70) Lesiak, M.; Binczarski, M.; Karski, S.; Maniukiewicz, W.; Rogowski, J.; Szubiakiewicz, E.; Berlowska, J.; Dziugan, P.; Witońska, I. *J. Mol. Catal. A Chem.* **2014**, *395*, 337–348.

(71) Fulajtárova, K.; Soták, T.; Hronec, M.; Vávra, I.; Dobročka, E.; Omastová, M. *Appl. Catal. A Gen.* **2015**, *502*, 78–85.

(72)   Mironenko, R. M.; Belskaya, O. B.; Gulyaeva, T. I.; Nizovskii, A. I.; Kalinkin, A. V.; Bukhtiyarov, V. I.; Lavrenov, A. V.; Likholobov, V. A. *Catal. Today* **2015**, *249*, 145–152.

(73)   Yang, J.; Ma, J.; Yuan, Q.; Zhang, P.; Guan, Y. *RSC Adv.* **2016**, *6* (95), 92299–92304.

(74)   Musci, J. J.; Merlo, A. B.; Casella, M. L. *Catal. Today* **2016**, *296* (December 2016), 43–50.

(75)   Infomine http://www.infomine.com/investment/metal-prices/ (accessed Jan 29, 2018).

(76)   Wu, W.-P.; Xu, Y.-J.; Chang, S.-W.; Deng, J.; Fu, Y. *ChemCatChem* **2016**, *8* (21), 3375–3380.

(77)   Sharma, R. V.; Das, U.; Sammynaiken, R.; Dalai, A. K. *Appl. Catal. A Gen.* **2013**, *454*, 127–136.

(78)   Kirk-Othmer. *Encyclopedia of Chemical Technology*; New York, 1992; Vol. 4.

(79)   Colmenares, J. C.; Luque, R. *Chem. Soc. Rev.* **2014**, *43* (3), 765–778.

(80)   Corma, A.; Lambies, V.; Melo, F.; Palou, J. *An. Quim. Ser. A-QUIMICA Fis. Y Quim. Tec.* **1980**, *76* (3), 304–307.

(81)   Lee, D.; Spitzer, U. *Can. J. Chem.* **1975**, *53*, 3709–3713.

(82)   Joshi, S. R.; Kataria, K. L.; Sawant, S. B.; Joshi, J. B. *Ind. Eng. Chem. Res.* **2005**, *44*, 325–333.

(83)   Ouyang, W.; Kuna, E.; Yepez, A.; Balu, A.; Romero, A.; Colmenares, J.; Luque, R. *Nanomaterials* **2016**, *6* (5), 93.

(84)   Higashimoto, S.; Kitao, N.; Yoshida, N.; Sakura, T.; Azuma, M.; Ohue, H.; Sakata, Y. *J. Catal.* **2009**, *266* (2), 279–285.

(85)   Kimi, M.; Jaidie, M. M. H.; Pang, S. C. *J. Phys. Chem. Solids* **2018**, *112*, 50–53.

(86)   Yu, Y.; Lu, B.; Wang, X.; Zhao, J.; Wang, X.; Cai, Q. *Chem. Eng. J.* **2010**, *162* (2), 738–742.

(87)   García-Suárez, E. J.; Balu, A. M.; Tristany, M.; García, A. B.; Philippot, K.; Luque, R. *Green Chem.* **2012**, *14* (5), 1434.

(88)   Makwana, V. D.; Son, Y.-C.; Howell, A. R.; Suib, S. L. *J. Catal.* **2002**, *210* (1), 46–52.

(89)   Marx, S.; Baiker, A. *J. Phys. Chem. C* **2009**, *113* (15), 6191–6201.

(90) Arné Dijksman; Arturo Marino-González; Antoni Mairata i Payeras; Isabel W. C. E. Arends, and; Roger A. Sheldon*, †. **2001**.

(91) Feng, X.; Lv, P.; Sun, W.; Han, X.; Gao, L.; Zheng, G. *Catal. Commun.* **2017**, *99*, 105–109.

(92) Yu, X.; Huo, Y.; Yang, J.; Chang, S.; Ma, Y.; Huang, W. *Appl. Surf. Sci.* **2013**, *280*, 450–455.

(93) Ma, C. Y.; Cheng, J.; Wang, H. L.; Hu, Q.; Tian, H.; He, C.; Hao, Z. P. *Catal. Today* **2010**, *158* (3–4), 246–251.

(94) Harada, T.; Ikeda, S.; Hashimoto, F.; Sakata, T.; Ikeue, K.; Torimoto, T.; Matsumura, M. *Langmuir* **2010**, *26* (22), 17720–17725.

(95) Jamwal, N.; Sodhi, R. K.; Gupta, P.; Paul, S. *Int. J. Biol. Macromol.* **2011**, *49* (5), 930–935.

(96) Della Pina, C.; Falletta, E.; Rossi, M. *J. Catal.* **2008**, *260* (2), 384–386.

(97) Deng, M.; Zhao, G.; Xue, Q.; Chen, L.; Lu, Y. *Appl. Catal. B Environ.* **2010**, *99* (1–2), 222–228.

(98) Choudhary, V. R.; Chaudhari, P. A.; Narkhede, V. S. *Catal. Commun.* **2003**, *4* (4), 171–175.

(99) Choudhary, V. R.; Dhar, A.; Jana, P.; Jha, R.; Uphade, B. S. *Green Chem.* **2005**, *7* (11), 768.

(100) Li, Y.; Huang, J.; Hu, X.; Lam, F. L.-Y.; Wang, W.; Luque, R. *J. Mol. Catal. A Chem.* **2016**, *425*, 61–67.

(101) Villa, A.; Wang, D.; Spontoni, P.; Arrigo, R.; Su, D.; Prati, L. *Catal. Today* **2010**, *157* (1–4), 89–93.

(102) Wang, L.; Zhu, L.; Bing, N.; Wang, L. *J. Phys. Chem. Solids* **2017**, *107*, 125–130.

(103) Miedziak, P.; Sankar, M.; Dimitratos, N.; Lopez-Sanchez, J. A.; Carley, A. F.; Knight, D. W.; Taylor, S. H.; Kiely, C. J.; Hutchings, G. J. *Catal. Today* **2011**, *164* (1), 315–319.

(104) Liu, J.; Zou, S.; Lu, L.; Zhao, H.; Xiao, L.; Fan, J. *Catal. Commun.* **2017**, *99*, 6–9.

(105) Yu, H.; Zhang, Y.; Fu, X.; Peng, F.; Wang, H.; Yang, J. *Catal. Commun.* **2009**, *10* (13), 1752–1756.

(106) Jung, D.; Lee, S.; Na, K. *Solid State Sci.* **2017**, *72*, 150–155.

(107) Serp, P.; Machado, B. F. *Nanostructured Carbon Materials for Catalysis*; Royal Society of Chemistry: Cambridge, 2015.

(108) Serp, P.; Figueiredo, J. L. *Carbon Materials for Catalysis*; Serp, P., Figueiredo, J. L., Eds.; John Wiley & Sons, Inc: New Jersey, 2008.

(109) Ren, Z.; Lan, Y.; Wang, Y. *Aligned carbon nanotubes physics, concepts, fabrication and devices*; Springer, 2013.

(110) Rodríguez-Reinoso, F. *Carbon* **1998**, *36* (3), 159–175.

(111) Busca, G. *Heterogeneous Catalytic Materials Solid State Chemistry , Surface Chemistry and Catalytic Behaviour*; 2014.

(112) Hembacher, S.; Giessibl, F. J.; Mannhart, J.; Quate, C. F. *Proc. Natl. Acad. Sci.* **2003**, *100* (22), 12539–12542.

(113) Rodriguez-Reinoso, F.; Silvestre-Albero, J. *Ref. Modul. Mater. Sci. Mater. Eng.* **2016**, No. April 2015, 1–14.

(114) Geim, A. K.; Novoselov, K. S. *Nat. Mater.* **2007**, *6* (3), 183–191.

(115) Stoller, M. D.; Park, S.; Zhu, Y.; An, J.; Ruoff, R. S. *Nano Lett.* **2008**, *8* (10), 3498–3502.

(116) Weiss, N. O.; Zhou, H.; Liao, L.; Liu, Y.; Jiang, S.; Huang, Y.; Duan, X. *Adv. Mater.* **2012**, *24* (43), 5782–5825.

(117) Soldano, C.; Mahmood, A.; Dujardin, E. *Carbon* **2010**, *48* (8), 2127–2150.

(118) Machado, B. F.; Serp, P. *Catal. Sci. Technol.* **2012**, *2* (1), 54.

(119) Novoselov, K. S.; Geim, A. K.; Morozov, S. V.; Jiang, D.; Zhang, Y.; Dubonos, S. V.; Grigorieva, I. V.; Firsov, A. A. *Science (80-.).* **2004**, *306* (5696), 666–669.

(120) Kim, K. S.; Zhao, Y.; Jang, H.; Lee, S. Y.; Kim, J. M.; Kim, K. S.; Ahn, J.-H.; Kim, P.; Choi, J.-Y.; Hong, B. H. *Nature* **2009**, *457* (7230), 706–710.

(121) Berger, C.; Song, Z.; Li, X.; Wu, X.; Brown, N.; Naud, C.; Mayou, D.; Li, T.; Hass, J.; Marchenkov, A. N.; Conrad, E. H.; First, P. N.; de Heer, W. A. *Science (80-.).* **2006**, *312* (5777), 1191–1196.

(122) Hummers, W. S.; Offeman, R. E. *J. Am. Chem. Soc.* **1958**, *80* (6), 1339–1339.

(123) Brodie, B. C. *Philos. Trans. R. Soc. London* **1859**, *149* (9), 249–259.

(124) Stankovich, S.; Dikin, D. A.; Piner, R. D.; Kohlhaas, K. A.; Kleinhammes, A.; Jia, Y.; Wu, Y.; Nguyen, S. T.; Ruoff, R. S. *Carbon N. Y.* **2007**, *45* (7), 1558–1565.

(125) Shin, H.-J.; Kim, K. K.; Benayad, A.; Yoon, S.-M.; Park, H. K.; Jung, I.-S.; Jin, M. H.; Jeong, H.-K.; Kim, J. M.; Choi, J.-Y.; Lee, Y. H. *Adv. Funct. Mater.* **2009**, *19* (12), 1987–1992.

(126) Zhou, M.; Wang, Y.; Zhai, Y.; Zhai, J.; Ren, W.; Wang, F.; Dong, S. *Chem. - A Eur. J.* **2009**, *15* (25), 6116–6120.

(127) Sundaram, R. S.; Gómez-Navarro, C.; Balasubramanian, K.; Burghard, M.; Kern, K. *Adv. Mater.* **2008**, *20* (16), 3050–3053.

(128) Choucair, M.; Thordarson, P.; Stride, J. A. *Nat. Nanotechnol.* **2009**, *4* (1), 30–33.

(129) Wang, H.; Robinson, J. T.; Li, X.; Dai, H. *J. Am. Chem. Soc.* **2009**, *131* (29), 9910–9911.

(130) McAllister, M. J.; Li, J.-L.; Adamson, D. H.; Schniepp, H. C.; Abdala, A. A.; Liu, J.; Herrera-Alonso, M.; Milius, D. L.; Car, R.; Prud'homme, R. K.; Ilhan A. Aksay. *Chem. Mater.* **2007**, *19*, 4396–4404.

(131) Botas, C.; Álvarez, P.; Blanco, C.; Santamaría, R.; Granda, M.; Gutiérrez, M. D.; Rodriguez-Reinoso, F.; Menéndez, R. **2013**, *52*, 476–485.

(132) Gadipelli, S.; Guo, Z. X. *Prog. Mater. Sci.* **2015**, *69*, 1–60.

(133) Asedegbega-Nieto, E.; Perez-Cadenas, M.; Morales, M. V.; Bachiller-Baeza, B.; Gallegos-Suarez, E.; Rodriguez-Ramos, I.; Guerrero-Ruiz, A. *Diam. Relat. Mater.* **2014**, *44*, 26–32.

(134) Castillejos-Lopez, E.; Bachiller-Baeza, B.; Asedegbega-Nieto, E.; Guerrero-Ruiz, A.; Rodriguez-Ramos, I. *RSC Adv.* **2015**, *5* (99), 81583–81598.

(135) Geng, D.; Yang, S.; Zhang, Y.; Yang, J.; Liu, J.; Li, R.; Sham, T.-K.; Sun, X.; Ye, S.; Knights, S. *Appl. Surf. Sci.* **2011**, *257* (21), 9193–9198.

(136) Purceno, A. D.; Machado, B. F.; Teixeira, A. P.; Medeiros, T. V; Benyounes, A.; Beausoleil, J.; Menezes, H. C.; Cardeal, Z. L.; Lago, R. M.; Serp, P. *Nanoscale* **2015**, *7* (1), 294–300.

(137) Li, B.; Sun, X.; Su, D. *Phys. Chem. Chem. Phys.* **2015**, *17*, 6691–6694.

(138) Luo, Z.; Lim, S.; Tian, Z.; Shang, J.; Lai, L.; MacDonald, B.; Fu, C.; Shen, Z.; Yu, T.; Lin, J. *J. Mater. Chem.* **2011**, *21* (22), 8038.

(139) Reddy, A. L. M.; Srivastava, A.; Gowda, S. R.; Gullapalli, H.; Dubey, M.; Ajayan, P. M. *ACS Nano* **2010**, *4* (11), 6337–6342.

(140) Jin, Z.; Yao, J.; Kittrell, C.; Tour, J. M. *ACS Nano* **2011**, *5* (5), 4112–4117.

(141) Panchakarla, L. S.; Subrahmanyam, K. S.; Saha, S. K.; Govindaraj, A.; Krishnamurthy, H. R.; Waghmare, U. V.; Rao, C. N. R. *R. Adv. Mater.* **2009**, *21*, 4726–4738.

(142) Wang, Y.; Shao, Y.; Matson, D. W.; Li, J.; Lin, Y. *ACS Nano* **2010**, *4* (4), 1790–1798.

(143) Lin, Z.; Song, M.; Ding, Y.; Liu, Y.; Wong, C. *PCCP* **2012**, *14*, 3381–3387.

(144) Sheng, Z. H.; Shao, L.; Chen, J. J.; Bao, W. J.; Wang, F. Bin; Xia, X. H. *ACS Nano* **2011**, *5* (6), 4350–4358.

(145) Canty, R.; Gonzalez, E.; MacDonald, C.; Osswald, S.; Zea, H.; Luhrs, C. C. *Materials (Basel).* **2015**, *8* (10), 7048–7058.

(146) Li, X.; Wang, H.; Robinson, J. T.; Sanchez, H.; Diankov, G.; Dai, H. *J. Am. Chem. Soc.* **2009**, *131* (43), 15939–15944.

(147) Wu, Z. S.; Ren, W.; Gao, L.; Liu, B.; Jiang, C.; Cheng, H. M. *Carbon* **2009**, *47* (2), 493–499.

(148) Sheng, Z.-H.; Shao, L.; Chen, J.-J.; Bao, W.-J.; Wang, F.-B.; Xia, X.-H. *ACS Nano* **2011**, *5* (6), 4350–4358.

(149) Paez, A.; Jesús, G.; Alvarez, P.; Granda, M.; Blanco, C.; Santamaria, Ricardo Blanco, P.; Fernandez, L.; Menendez, R. M.; Calle, F. Methods for producing graphene with tunable properties by a multi-step thermal reduction process. WO 2016042099 A1, 2014.

(150) Zhang, C.; Lv, W.; Xie, X.; Tang, D.; Liu, C.; Yang, Q.-H. *Carbon* **2013**, *62*, 11–24.

(151) Dao, T. D.; Jeong, H. M. *Mater. Res. Bull.* **2015**, *70*, 651–657.

(152) Guerrero-Ruiz, A.; Rodriguez-Ramos, I.; Rodriguez-Reinoso, F.; Moreno-Castilla, C.; Lopez-Gonzalez, J. D. *Carbon* **1988**, *26* (4), 417–423.

(153) Fujita, S.-I.; Yoshida, H.; Arai, M. *J. carbon Res.* **2017**, *3* (4), 31.

(154) Yadav, R.; Dixit, C. K. *J. Sci. Adv. Mater. Devices* **2017**, *2* (2), 141–149.

(155) Wang, H.; Maiyalagan, T.; Wang, X. *ACS Catal.* **2012**, *2* (5), 781–794.

(156) Wei, Q.; Tong, X.; Zhang, G.; Qiao, J.; Gong, Q.; Sun, S. *Catalysts* **2015**, *5* (3), 1574–1602.

(157) Ayala, P.; Arenal, R.; Rümmeli, M.; Rubio, A.; Pichler, T. *Carbon* **2010**, *48* (3), 575–586.

(158) Li, M.; Xu, F.; Li, H.; Wang, Y. *Catal. Sci. Technol.* **2016**, *6* (11), 3670–3693.

(159) Ferrari, A. C.; Bonaccorso, F.; Fal'ko, V.; Novoselov, K. S.; Roche, S.; Bøggild, P.; Borini, S.; Koppens, F. H. L.; Palermo, V.; Pugno, N.; Garrido, J. A.; Sordan, R.; Bianco, A.; Ballerini, L.; Prato, M.; Lidorikis, E.; Kivioja, J.; Marinelli, C.; Ryhänen, T.; Morpurgo, A.; Coleman, J. N.; Nicolosi, V.; Colombo, L.; Fert, A.; Garcia-Hernandez, M.; Bachtold, A.; Schneider, G. F.; Guinea, F.; Dekker, C.; Barbone, M.; Sun, Z.; Galiotis, C.; Grigorenko, A. N.; Konstantatos, G.; Kis, A.; Katsnelson, M.; Vandersypen, L.; Loiseau, A.; Morandi, V.; Neumaier, D.; Treossi, E.; Pellegrini, V.; Polini, M.; Tredicucci, A.; Williams, G. M.; Hee Hong, B.; Ahn, J.-H.; Min Kim, J.; Zirath, H.; van Wees, B. J.; van der Zant, H.; Occhipinti, L.; Di Matteo, A.; Kinloch, I. A.; Seyller, T.; Quesnel, E.; Feng, X.; Teo, K.; Rupesinghe, N.; Hakonen, P.; Neil, S. R. T.; Tannock, Q.; Löfwander, T.; Kinaret, J. *Nanoscale* **2015**, *7* (11), 4587–5062.

(160) Tao, F. F. *Metal Nanoparticles for Catalysis: Advances and Applications*; Tao, F., Ed.; The Royal Society of Chemistry: Cambridge, 2014.

(161) Dobrzanski, L. A.; Pawlyta, M.; Krzton, A.; Liszka, B.; Tai, C. W. *Acta Phys. Pol. A* **2010**, *118* (3), 483–486.

(162) Brunauer, S.; Emmett, P. H.; Teller, E. *J. Am. Chem. Soc.* **1938**, *60* (1), 309–319.

(163) Che, M.; Vedrine, J. C. *Characterization of Solid Materials and Heterogeneous Catalysts*; Wiley-VCH Verlag & Co. KGaA: Weinheim, 2012.

(164) Liu, H. *Ammonia Synthesis Catalysts*; World Scientific Publishing Co, 2013; Vol. 53.

(165) Rouquerolt, J.; Avnir, D.; Fairbridge, C. W.; Everett, D. H.; Haynes, J. H.; Pernicone, N.; Ramsay, J. D. F.; Sing, K. S. W.; Unger, K. K. *Pure Appl. Chem.* **1994**, *66* (8), 1739–1758.

(166) Marangoni, A. G.; Peyronel, M. F. *X-Ray Powder Diffractometry*; 2013.

(167) Chorkendorff, I.; Niemantsverdriet, J. W. *Concepts of Modern Catalysis and Kinetics*; Wiley-VCH Verlag & Co. KGaA: Weinheim, 2003.

(168) Skoog, D. A.; Holler, F. J.; Nieman, T. A. *Principios de Análisis Instrumental*; McGraw-Hill: Madrid, 2001.

(169) Watts, J. F.; Wolstenholme, J. *An Introduction to Surface Analysis by XPS and AES 1st Edition*; John Wiley & Sons, Inc: West Sussex, 2003.

(170) Bumiller, M. *Chromatogr. Today* **2012**, No. April, 36–37.

(171) Zhu, B.; Xia, P.; Ho, W.; Yu, J. *Appl. Surf. Sci.* **2015**, *344*, 188–195.

(172) Serp, P.; Philippot, K. Wiley-VCH Verlag & Co. KGaA: Weinheim, 2013; pp 443–471.

(173) Gallegos-Suarez, E.; Perez-Cadenas, M.; Guerrero-Ruiz, A.; Rodriguez-Ramos, I.; Arcoya, A. *Appl. Surf. Sci.* **2013**, *287*, 108–116.

(174) Cazes, J. *Analitycal Instrumentation Handbook*; 2005.

(175) Dieing, T.; Hollricher, O.; Toporski, J. *Confocal Raman Microscopy*; Springer, 2010.

(176) Deutschmann, O.; Knözinger, H.; Kochloefl, K.; Turek, T. *Ullmann's Encycl. Ind. Chem.* **2009**, *1*, 2–110.

(177) Wepasnick, K. A.; Smith, B. A.; Bitter, J. L.; Howard Fairbrother, D. *Anal. Bioanal. Chem.* **2010**, *396* (3), 1003–1014.

(178) Desimoni, E.; Casella, G. I.; Morone, A.; Salvi, A. M. *Surf. Interface Anal.* **1990**, *15* (10), 627–634.

(179) Matter, P. H.; Zhang, L.; Ozkan, U. S. *J. Catal.* **2006**, *239* (1), 83–96.

(180) Pels, J. R.; Kapteijn, F.; Moulijn, J. a.; Zhu, Q.; Thomas, K. M. *Carbon* **1995**, *33* (11), 1641–1653.

(181) Biniak, S.; Szymański, G.; Siedlewski, J.; Świątkoski, A. *Carbon* **1997**, *35* (12), 1799–1810.

(182) Faba, L.; Criado, Y. A.; Gallegos-Suarez, E.; Pérez-Cadenas, M.; Díaz, E.; Rodriguez-Ramos, I.; Guerrero-Ruiz, A.; Ordóñez, S. *Appl. Catal. A Gen.* **2013**, *458*, 155–161.

(183) García-García, F. R.; Álvarez-Rodríguez, J.; Rodriguez-Ramos, I.; Guerrero-Ruiz, A. *Carbon* **2010**, *48* (1), 267–276.

(184) van Dommele, S.; de Jong, K. P.; Bitter, J. H. *Chem. Commun. (Camb).* **2006**, *76* (46), 4859–4861.

(185) Dongil, A. B.; Bachiller-Baeza, B.; Guerrero-Ruiz, A.; Rodríguez-Ramos, I.; Martínez-Alonso, A.; Tascón, J. M. D. *J. Colloid Interface Sci.* **2011**, *355* (1), 179–189.

(186) Figueiredo, J. .; Pereira, M. F. .; Freitas, M. M. .; Órfão, J. J. . *Carbon* **1999**, *37*, 1379–1389.

(187) Zielke, U.; Hüttinger, K. J.; Hoffman, W. P. *Carbon* **1996**, *34* (8), 983–998.

(188) Chen, C.-M.; Zhang, Q.; Zhao, X.-C.; Zhang, B.; Kong, Q.-Q.; Yang, M.-G.; Yang, Q.-H.; Wang, M.-Z.; Yang, Y.-G.; Schlögl, R.; Su, D. S. *J. Mater. Chem.* **2012**, *22* (28), 14076.

(189) Tuinstra, F.; Koenig, J. L. *J. Chem. Phys.* **1970**, *53* (3), 1126–1130.

(190) Pimenta, M. A.; Dresselhaus, G.; Dresselhaus, M. S.; Cançado, L. G.; Jorio, A.; Saito, R. *Phys. Chem. Chem. Phys.* **2007**, *9* (11), 1276–1290.

(191) Gallegos-Suárez, E. Valorización Del Glicerol Mediante Procesos Catalizados Por Nanopartículas Metálicas Soportadas, UNED, 2015.

(192) Esteban-Arranz, A. Sintesis, caracterizacion y aplicacion de nanomateriales de carbono para el tratamiento de aguas residuales, UNED, 2017.

(193) Orellana, F.; Lisperguer, J.; Nuñez, C. *J. Chil. Chem. Soc.* **2014**, *59* (1), 2389–2393.

(194) White, L.; Koo, Y.; Yun, Y.; Sankar, J. *J. Nanomater.* **2013**, *2013*.

(195) Ramirez-Barria, C.; López-Olmos, C.; Guerrero-Ruiz, A.; Rodríguez-Ramos, I. *RSC Adv.* **2017**, *7* (70), 44568–44577.

(196) Guerrero-Ruiz, A.; Badenes, P.; Rodríguez-Ramos, I. *Appl. Catal. A Gen.* **1998**, *173* (2), 313–321.

(197) Montero, M. A.; Gennero de Chialvo, M. R.; Chialvo, A. C. *J. Mater. Chem.* **2009**, *19* (20), 3276.

(198) Yanson, A. I.; Yanson, Y. I. *Low Temp. Phys.* **2013**, *39* (3), 312–317.

(199) Chen, X.; Deng, D.; Pan, X.; Hu, Y.; Bao, X. *Chem. Commun.* **2015**, *51* (1), 217–220.

(200) Guerrero-Ruiz, a.; Gallegos-Suarez, E.; Gonzalo-Chacon, L.; Rodriguez-Ramos, I. *Thermochim. Acta* **2013**, *567* (February), 112–117.

(201) Artz, J.; Palkovits, R. *ChemSusChem* **2015**, *8* (22), 3832–3838.

(202) Han, X.; Geng, L.; Guo, Y.; Jia, R.; Liu, X.; Zhang, Y.; Wang, Y. *Green Chem.* **2016**, *18*, 1597–1604.

(203) Folkesson, B. *Acta Chemica Scandinavica*. 1973, pp 287–302.

(204) Nakagawa, Y.; Takada, K.; Tamura, M.; Tomishige, K. *ACS Catal.* **2014**, *4* (8), 2718–2726.

(205) Shen, J. Y.; Adnot, a.; Kaliaguine, S. *Appl. Surf. Sci.* **1991**, *51* (1–2), 47–60.

APPENDIX

Publications derived from this Doctoral Thesis

Publications:

Carolina Ramirez-Barria, Cristina López-Olmos, Antonio Guerrero-Ruiz and Inmaculada Rodríguez-Ramos (2017) Direct catalytic effect of nitrogen functional groups exposed on graphenic materials when acting cooperatively with Ru nanoparticles. RSC Advances, 7, 44568-44577

Check for updates

Cite this: RSC Adv., 2017, 7, 44568

Direct catalytic effect of nitrogen functional groups exposed on graphenic materials when acting cooperatively with Ru nanoparticles†

Carolina Ramirez-Barria,[ab] Cristina López-Olmos,[b] Antonio Guerrero-Ruiz [*ac] and Inmaculada Rodríguez-Ramos [bc]

A number of inorganic carbonaceous materials (activated carbon, high surface area graphite and graphenic materials) have been used as supports of Ru nanoparticles in order to determine their catalytic properties in the base-free aqueous-phase oxidation of 5-hydroxymethylfurfural (HMF) to 2,5-furandicarboxylic acid (FDCA). In particular, we have studied in detail reduced graphene oxide (rGO) and nitrogen doped reduced graphene oxide (NrGO), which are the support materials that produce more selective ruthenium catalysts. Also the effects of different metal precursors used in the preparation of the Ru nanocrystallites have been evaluated. Both support materials and Ru catalysts were characterized by elemental analysis, nitrogen physisorption (BET), thermogravimetric analysis (TGA), transmission electron microscopy (TEM), and X-ray photoelectron spectroscopy (XPS). The point of zero charge (PZC) for the graphenic materials was also determined. Interestingly the different supports significantly modify the catalytic performances, the graphenic materials being those that under our experimental reaction conditions produce the highest selectivity to FDCA. On these supports (rGO and NrGO) the highest HMF conversion was achieved by using triruthenium dodecacarbonyl as the ruthenium precursor. For the improved catalyst, Ru supported on NrGO, the yield of FDCA becomes close to 80%. This catalyst has been reused several times with neither loss of activity nor modification in selectivity values. Characterization data indicate these catalytic results can be correlated to the basic properties of the NrGO support as well as to the surface properties of Ru nanoparticles. These findings indicated that the metal precursor and the surface functional groups exposed on the support can modulate the catalytic properties, in particular amending the selectivity towards FDCA production.
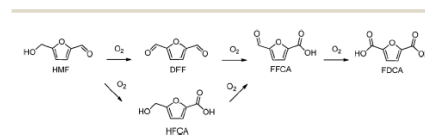
Introduction

In the last few years there has been a growing interest in the conversion of renewable biomass resources into chemicals and fuels.[1] In this context, HMF is a promising biomass-derived platform molecule generally produced through chemical dehydration of hexoses, such as glucose and fructose.[2] The oxidation of HMF can generate several kinds of products such as 2,5-diformylfuran (DFF), 5-hydroxymethyl-2-furancarboxylic acid (HFCA), 5-formyl-2-furancarboxylic acid (FFCA) and 2,5-

furandicarboxylic acid (FDCA) (Scheme 1). FDCA has been identified by the U.S. Department of Energy as one of the 12 top value added chemicals from biomass.[3] FDCA can be used as an alternative monomer to potentially replace terephthalic acid which is involved in the production of polyethylene terephthalate (PET).[4]

Several stoichiometric oxidants, such as HNO_3, N_2O_4 and $KMnO_4$,[5] as well as homogenous catalytic systems[6] have been used for the HMF oxidation into FDCA. However, harsh reaction conditions, corrosive properties of the media and production of large amounts of waste have a negative economic and environmental impact.

[a] Dpto. Química Inorgánica y Técnica, Facultad de Ciencias UNED, Senda del Rey 9, 28040 Madrid, Spain. E-mail: aguerrero@ccia.uned.es
[b] Instituto de Catálisis y Petroleoquímica, CSIC, Cantoblanco, Marie Curie 2, 28049 Madrid, Spain
[c] Unidad Asociada UNED-ICP/CSIC Grupo de Diseño y Aplicación de Catalizadores Heterogéneos, Spain
† Electronic supplementary information (ESI) available: Fig. S1 contains TEM micrographs of the different graphenic supports, Fig. S2 contains XPS spectra of the N 1s region for NrGO, Fig. S3 contains TGA for graphenic supports and Fig. S4 XPS spectra of the Ru 3p region of Ru(Cl)/rGO and Ru(Cl)/NrGO catalysts. See DOI: 10.1039/c7ra08774h

Scheme 1 Reaction pathway from HMF to FDCA.

Under revision:

Carolina Ramirez-Barria, Mark Isaacs, Karen Wilson, Antonio Guerrero-Ruiz, Inmaculada Rodríguez-Ramos (2018). Optimization of Ruthenium based catalysts for the aqueous phase hydrogenation of furfural to furfuryl alcohol. Under revision Applied Catalysis A: General

Ramirez-Barria, C., Villaro-Abalos, E., Guerrero-Ruiz, A., Rodriguez-Ramos, I. (2018). Upgrading the properties of reduced graphene oxide and nitrogen doped reduced graphene oxide produced by thermal reduction. Under revisión MR Bulletin

Carolina S. Ramirez-Barria, Mark Isaacs, Christopher Parlett, Karen Wilson, Antonio Guerrero-Ruiz, Inmaculada Rodríguez-Ramos (2018). Ru nanoparticles supported on N-doped reduced graphene oxide as valuable catalyst for the selective aerobic oxidation of benzyl alcohol. In preparation

Other publications:

C. Ramirez-Barria, A. Guerrero-Ruiz, E. Castillejos-López, I. Rodríguez-Ramos, J. Durand, J. Volkman and P. Serp(2016). Surface properties of amphiphilic carbon nanotubes and study of their applicability as basic catalysts. RSC Advances, 6, 54293–54298.

Alan J. McCue, Antonio Guerrero-Ruiz, **Carolina Ramirez-Barria**, Inmaculada Rodríguez-Ramos, James A. Anderson (2017) Selective hydrogenation of mixed alkyne/alkene streams at elevated pressure over a palladium sulfide catalyst. Journal of Catalysis, 355, 40-52

Wenjing Song, M.Carmen Lozano-Martín, Esteban Gallegos-Suarez, **Carolina Ramirez-Barria,** Weizheng Weng, Xiaodong Yi, Belén Bachiller-Baeza, Antonio Guerrero-Ruiz and Inmaculada Rodríguez-Ramos (2018) New insights in the development of carbon supported ruthenium catalysts for hydrogenation of levulinic acid. Current Catalysis, 7.

Curriculum Vitae

Education:

<u>**UNED**</u>
PhD Student, FPU Fellow (Highest merit fellowship of the Spanish Government)

2015-current
Supervisor: Prof. Antonio Guerrero-Ruiz and Inmaculada Rodriguez-Ramos
Thesis title: New nanomaterials applied as catalyst for some processes of valorisation of products derived from biomass

<u>**UNED**</u>

Master of Science (M.Sc.) Master´s degree in Inorganic Chemistry and Chemical Engineering

(2014– 2015) Supervisor: Prof. Antonio Guerrero-Ruiz

Research Project: Synthesis of carbon nanotubes with amphiphilic properties and study of some applications as catalysts. Defence on June 2015 obtaining the maximum grade with Honours

<u>**UNED**</u>

Bachelor's degree, Chemistry (First Class Honours)

(2010 – 2014) Undergraduate Research Supervisor: Prof. Antonio Guerrero-Ruiz

Research Project: Metallic nanoparticles: Some examples of relationships between size and superficial structures of supported monometallic nanoparticles and their catalytic properties. Defence on June 2014 obtaining the maximum grade with Honours

Conferences and Presentations:

- **EUROPACAT 2017**

13th European Congress on Catalysis. Florence, August 2017

Poster: Selective oxidation of 5-hydroxymethylfurfural into 2,5-furandicarboxylic using ruthenium supported catalyst

- **SECAT 2017**

Congress of the Spanish Society of Catalysis. Oviedo, June 2017

Poster: Significant effects of the support materials for the catalytic oxidation of 5-Hydroxymethylfurfural over ruthenium metallic nanoparticles

- **Trapcat I**

First Trans Pyrenean Meeting in Catalysis. Toulouse, October 2016

Poster: Base-free oxidation of 5-hydroxymethylfurfural to 2,5-furandicarboxylic acid over graphenic materials supported Ru catalysts

- **SECAT 2015**

Congress of the Spanish Society of Catalysis.Barcelona, July 2015

Poster: Synthesis of carbon nanotubes with amphiphilic properties and study of some applications as catalysts

Awards, fellowships and Grants:

- **FPU Short Stay**

(2017) Stay at "European Bioenergy Research Institute" (University of Aston) Birmingham. Research project under direction of Professor Karen Wilson

- **FPU Ph.D Fellowship (Highest merit fellowship of the Spanish Government)**

(2016- current) Prospective Professors in training

- **SECAT Grant (Spanish Society of Catalysis)**

(2015) Master Project Grant

- **Erasmus Grant**

(2015) 4 months stay at "Ecole nationale superieure des ingenieurs en arts chimiques et technologiques" (ENSIACET) Toulouse. Research project under direction of Professor Philippe Serp

- **Extraordinary Chemistry Degree Promotion Award (UNED)**

(2015) Academic Excellence Award